

Advanced Magnetic System for UXO Detection and Discrimination

Final Report

SERDP Project No. 1327

Contract Number: DACA72-02-C-0042

Issuing Agency

SERDP Program Support Office
1155 Herndon Parkway, Suite 900
Herndon, VA 20170

Prepared by:

Dr. Yacine Dalichaouch and Dr. Peter V. Czipott, GE Security
Professor Lawrence Carin, Duke University

GE Security

Quantum Magnetics, Inc.
15175 Innovation Drive · San Diego, CA · 92128 · Tel: (858) 605-5500 · FAX: (858) 605-5501
QM Project No. CW10515

June 4, 2007

Rev. 2

Report Documentation Page			Form Approved OMB No. 0704-0188		
Public reporting burden for the collection of information is estimated to average 1 hour per response, including the time for reviewing instructions, searching existing data sources, gathering and maintaining the data needed, and completing and reviewing the collection of information. Send comments regarding this burden estimate or any other aspect of this collection of information, including suggestions for reducing this burden, to Washington Headquarters Services, Directorate for Information Operations and Reports, 1215 Jefferson Davis Highway, Suite 1204, Arlington VA 22202-4302. Respondents should be aware that notwithstanding any other provision of law, no person shall be subject to a penalty for failing to comply with a collection of information if it does not display a currently valid OMB control number.					
1. REPORT DATE 04 JUN 2007		2. REPORT TYPE Final		3. DATES COVERED -	
4. TITLE AND SUBTITLE Advanced Magnetic System for UXO Detection and Discrimination				5a. CONTRACT NUMBER DACA72-02-C-0042	
				5b. GRANT NUMBER	
				5c. PROGRAM ELEMENT NUMBER	
6. AUTHOR(S) Dalichaouch, Yacine Czipott, Peter *Carin, Lawrence				5d. PROJECT NUMBER MM-1327	
				5e. TASK NUMBER	
				5f. WORK UNIT NUMBER	
7. PERFORMING ORGANIZATION NAME(S) AND ADDRESS(ES) GE Quantum Magnetics, Inc. 15175 Innovation Drive San Diego, CA 92128 * Duke University				8. PERFORMING ORGANIZATION REPORT NUMBER CW10515	
9. SPONSORING/MONITORING AGENCY NAME(S) AND ADDRESS(ES) Strategic Environmental Research and Development Program 901 North Stuart Street, Suite 303 Arlington, VA 22203				10. SPONSOR/MONITOR'S ACRONYM(S) SERDP	
				11. SPONSOR/MONITOR'S REPORT NUMBER(S)	
12. DISTRIBUTION/AVAILABILITY STATEMENT Approved for public release, distribution unlimited					
13. SUPPLEMENTARY NOTES The original document contains color images.					
14. ABSTRACT					
15. SUBJECT TERMS					
16. SECURITY CLASSIFICATION OF:			17. LIMITATION OF ABSTRACT UU	18. NUMBER OF PAGES 93	19a. NAME OF RESPONSIBLE PERSON
a. REPORT unclassified	b. ABSTRACT unclassified	c. THIS PAGE unclassified			

This report was prepared under contract to the Department of Defense Strategic Environmental Research and Development Program (SERDP). The publication of this report does not indicate endorsement by the Department of Defense, nor should the contents be construed as reflecting the official policy or position of the Department of Defense. Reference herein to any specific commercial product, process, or service by trade name, trademark, manufacturer, or otherwise, does not necessarily constitute or imply its endorsement, recommendation, or favoring by the Department of Defense.

TABLE OF CONTENTS

TABLE OF CONTENTS	ii
LIST OF ACRONYMS.....	iv
1 Implement the improved transmitter amplifier and the ferrite calibration method on the SERDP system for subsequent measurements.....	1
1.1 Improved Transmitter Amplifier	1
1.2 Ferrite Calibration and Correction.....	1
2 Measure MR-sensor system noise across the system bandwidth and cancellation of the primary field using improved transmitter amplifier.....	4
2.1 MR Sensor Noise Characterization.....	4
2.2 Frequency-domain (FD) system	6
2.2.1 System Description and Operation	6
2.2.2 Hardware modifications.....	10
2.2.3 Software development	10
2.3 Time-domain (TD) system	13
2.3.1 System Description and Operation	13
2.3.2 Hardware modifications.....	16
2.3.3 Software development (V. 3).....	17
3 Evaluate and tabulate the maximum range allowing UXO/clutter characterization for discrimination for both Time-Domain and Frequency-Domain systems. Generate response curves for different UXO and clutter items at a constant SNR. This includes modifying the acquisition software to calculate the response SNR in real time.....	19
3.1 Measurement setup	19
3.2 Laboratory prototype FD and TD sensors	24
3.2.1 FD System.....	24
3.2.2 TD System	25
4 Evaluate and tabulate maximum detection range of UXO targets using passive MR system.....	26
5 Process and analyze measurements from Task 2 to address technical issues.....	27
5.1 EMI Model.....	27
5.2 Feature Extraction.....	28
5.3 Classifier Model Design	28

5.4	Evaluation of testing data	30
5.5	Presentation of results.....	31
5.6	Results.....	31
5.6.1	Frequency-domain data.....	31
5.6.2	Time-domain data	36
5.6.3	Discussion.....	40
6	Conclusions	40

LIST OF ACRONYMS

A	Ampère
AC	Alternating Current
A/D	Analog-to-Digital (Converter)
BP	Band-Pass
CCV	Compensation Control Voltage
CD ROM	Compact Disc Read-Only Memory
CL	Clutter
cm	Centimeter
D/A	Digital-to-Analog (Converter)
DAC	Digital-to-Analog Converter
DAQ	Data Acquisition
dB	Decibels
DC	Direct Current
DR	Detection Range
EMI	Electromagnetic Induction
FD	Frequency Domain
FET	Field Effect Transistor
GE	General Electric Company
GFE	Government Furnished Equipment
GMM	Gaussian Mixture Model
HMMWV	High Mobility Multi-Wheeled Vehicle
Hz	Hertz
I	In-phase
ID	Identification
kHz	Kilohertz
KL	Kullback-Leibler
L-R	Inductive-Resistive
LPF	Low-Pass Filter
m	Meter
mm	Millimeter
MOSFET	Metal Oxide Semiconductor Field Effect Transistor
MR	Magnetoresistive
Ms	Megasample
NVESD	Night Vision and Electronic Sensors Directorate
Q	Quadrature
R&D	Research and Development
SCV	Source Control Voltage
SERDP	Strategic Environmental Research and Development Program
SNR	Signal to Noise Ratio
S/R	Set/Reset
TD	Time Domain
TF	Transfer Function
UXO	Unexploded Ordnance
V	Volts, voltage

VB	Variational Bayes
VCCS	Voltage Controlled Current Source

LIST OF FIGURES

Figure 1. Response of a brass ring showing high-frequency errors.....	2
Figure 2. Response of a ferrite toroidal core without background subtraction.....	2
Figure 3. Same ferrite core response with background subtraction.....	3
Figure 4. Phase-corrected ferrite response curves.	4
Figure 5. Experimental arrangement used to measure the system noise.	5
Figure 6. MR sensor calibration and noise measurement plot.....	6
Figure 7. Block diagram of the FD system.	7
Figure 8. Example of a two-axis sensor calibration window during auto-calibration.	9
Figure 9. Compensation review window (single-axis sensor example).	9
Figure 10. Target response function after subtracting instrumental background.	10
Figure 11. System noise with source field compensation between 10 Hz and 100 kHz showing improvement between the new (red squares) and old (blue diamonds) methods.	11
Figure 12. FD system noise floor as a function of frequency.....	12
Figure 13. TD system block diagram.....	14
Figure 14. Symmetric set/reset pulses.	15
Figure 15. Pulsed source field ramps, showing alternating symmetry (traces superimposed for display purposes).	15
Figure 16. Typical TD background-subtracted response output.....	16
Figure 17. Original S/R pulse	16
Figure 18. Improved S/R pulse.....	17
Figure 19. Left: Sensor output as a function of time as the capacitors dump charge into the coil. Right: Detailed view of the current decaying from the source coil. It takes 4.2 microseconds for the sensor output to go from its maximum to zero.	17
Figure 20. Left: Sensor output while FET is open and then closed. Right: expanded view, showing details during current drainage.	19
Figure 21. UXO targets used in the measurements of characterization standoff range.....	22
Figure 22. Clutter items used in the measurements of characterization standoff range. A 1" scale bar is shown in the lower left hand corner.	22
Figure 23. Other clutter items used in the study.	23
Figure 24. Measurement layout showing the plus-shaped grid and measurement points 1, 2, 3, 4, 5, 6, and 7. Because of the orientation of the target in the y - z plane, there is symmetry with respect to the y -axis and only measurements on one side of the x -axis (i.e., points 6 and 7) need to be recorded.....	24
Figure 25. Picture showing FD laboratory system.....	25

Figure 26. Distribution of mixture components for feature vectors associated with the FD training data. The data index identifies the UXO item used in training, each item measured in each of the three cardinal orientations. Eight training items thus yield twenty-four indices.....	32
Figure 27. Ranking of targets from least likely to most likely of being a UXO using FD data. .	35
Figure 28. Distribution of mixture component for feature vectors associated with TD training data. Data index again corresponds to measurements of eight UXO items, each in three cardinal orientations.....	36
Figure 29. Ranking of targets from least likely to most likely of being a UXO using TD data. .	39

LIST OF TABLES

Table 1. Phase correction vs. frequency as determined from ferrite core data.....	3
Table 2. Functional description and specification of FD system components.	7
Table 3. System calibration algorithm in “pseudo-code”.	8
Table 4. Functional description and specifications of TD system components.....	14
Table 5. Characterization standoff range for TD and FD systems corresponding to a response SNR = 5.	21
Table 6. Summary of detection ranges for different types of UXO, as measured using a Honeywell magnetometer.	26
Table 7. Analysis of FD training data showing the log-likelihood that each training-UXO data set was generated from the UXO GMM (first result column) and from the third and fourth Gaussian mixtures (second and third columns, respectively). Three rows per item represent the log-likelihoods measured in each of the three cardinal orientations of the training item.	33
Table 8. Analysis of FD testing data showing log-likelihood that each testing target measurement was generated from the UXO GMM (first result column) or generated from the third and fourth Gaussian mixture (second and third columns, respectively). Test objects were only measured in one, random orientation, so there is only one row of likelihood estimates per item.	34
Table 9. Analysis of TD training data showing log-likelihood that each training-UXO data set was generated from the UXO GMM and generated from each significant mixture (left to right). Each training item was measured in three cardinal orientations, yielding three rows of likelihoods per item.	37
Table 10. Analysis of TD testing data showing log-likelihood that each testing target data set was generated from the UXO GMM, or from each Gaussian mixture component (right to left). Each test target was measured in only a single, random orientation.	38

ACKNOWLEDGEMENTS

This project was performed by Quantum Magnetix, Inc., a wholly owned subsidiary of the General Electric Company's GE Homeland Protection, Inc. Signal processing investigations were carried out by Professor Lawrence Carin and his group in the Electrical Engineering Department of Duke University.

EXECUTIVE SUMMARY

This project addressed issues of Unexploded Ordnance (UXO) detection, as a key component of the land remediation problem. Remediation is a formidably expensive operation. Much of the cost is a consequence of “dry” holes dug to reveal a benign object instead of the expected hazardous UXO, and of holes dug in the wrong location, or made much larger than they ought, thanks to faulty localization of the ordnance.

The concept proposed for development in the present project is based on the fact that most UXO uses ferrous steel. Its ferromagnetic and conducting properties both distort the earth’s static magnetic field and generate a secondary field in response to a time-dependent exciting field. The proposal and initial statement of work set out to develop a single instrument combining target detection and accurate localization (via passive magnetic gradiometry of the earth’s-field distortion) with target-clutter discrimination (using the response to a broadband exciting field). No such single instrument exists today. The proposed instrument was to incorporate a full tensor magnetic gradiometer inside a three-axis excitation field source. With the source turned off, the gradiometer enables detection and localization. With the source turned on at closer range, the gradiometer measures the broadband response of the object and a classification algorithm, developed independently at Duke University, would decide whether the object was a UXO or not.

Early on in the program, it was recognized that the passive measurement system component is more fully advanced than the multi-axis, broadband excitation component. In order to address the greater technical risk that the latter presents, the program was re-scoped to focus exclusively on the multi-axis, broadband system.

In any “active” system—that is, one that uses a source to generate an excitation field and detects the secondary field caused by the response of an object—a key issue is suppressing the direct coupling of the excitation field to the sensor. This problem is exacerbated when the sensor is a gradiometer making differential measurements of the magnetic field at separate locations.

Another challenge is to make an excitation field source that illuminates the object along three different axes. In particular, it is difficult to make the source both compact and energy-efficient, especially when the object of interest is buried at some distance from the source.

The difficulties presented by these challenges led to a reconsideration of the system design: instead of a gradiometer, we used a three-axis magnetometer, and we further reduced the three-axis source to a single-axis source. The expectation was that measuring the object’s response in three axes might mitigate the loss of information from reducing the number of excitation axes.

We implemented the broadband excitation in two different systems. One, called a “frequency-domain” (FD) system, uses continuous-wave sinusoidal excitation at selectable frequencies covering the band from a few tens of Hertz (Hz) to a few hundred kilohertz (kHz). The other, called a “time-domain” (TD) system, uses a pulsed excitation field that excites a broad spectrum simultaneously. Each has theoretical and practical advantages and drawbacks that have been discussed in the literature (particularly in the context of geophysical exploration systems), without a real resolution concerning their relative merits.

An initial set of measurements on selected UXO (supplied as GFE) and clutter items proved too small to determine the efficacy of target-clutter discrimination. A program review also showed that the data were collected at different signal to noise ratio (SNR) levels, rendering

interpretation highly ambiguous. Work was suspended and then resumed with instruction from the Program Office to focus narrowly on collecting a broad set of data, all at the same SNR, in order to assess the efficacy of broadband, multi-axis discrimination.

Defining SNR for an active system is not a trivial problem. For example, an FD system illuminating the test object at different frequencies yields responses whose individual SNR depends on the frequency. Furthermore, a definition of SNR suitable for an FD system is not appropriate for a TD system where the measurement is inherently broadband, unlike the collection of discrete narrow-band measurements of the FD system. Considerable effort went into defining measures of SNR appropriate for FD and TD systems. Such measures were defined and verified to yield meaningful results. The development of these SNR definitions is, in itself, a key result of the program, since these definitions may be used in assessing data collected by *any* FD or TD system in existence or in development.

Data were collected on a larger sample of UXO and clutter items. All data were collected at ranges from the sensor to the test object that yielded an SNR of five, as a fiducial standard. Data consisted of a training set—data collected from each of the types of UXO in known orientations, with ground truth—used to train the classification algorithms, and a test set—data collected from both clutter and UXO, in arbitrary orientations, with the objects not identified to the classifiers. Duke trained their algorithms, developed independently and based on an algorithm applying variational Bayes statistics and a Gaussian mixture model to the data, on the training set and then tested them against the test set.

The models ranked the unknown test set from lowest to highest in order of likelihood of being UXO.

The FD results are not encouraging. A total of 27 objects, eight UXO and nineteen clutter, were tested with the FD system. If one simply divides the ranked list at the center into two segments and identifies the higher-likelihood segment as UXO and the lower-likelihood segment as clutter, one will have correctly identified exactly half the UXO and half the clutter items: the algorithm and data combine to give the result of a coin toss.

At first, the result of the algorithm applied to the TD system data (using 24 objects, seven UXO and seventeen clutter) looks even worse: only one UXO is identified correctly, and six are misidentified. However, *simply inverting the output* of the Duke algorithm yields six of seven UXO identified correctly, for a successful UXO identification rate of 85.7% and a successful clutter identification rate of 64.7%. Interpreted as conventional detection and false alarm probabilities, one obtains a detection rate of 85.7% at a false alarm rate of 35.3%.

Using internal R&D funds, Quantum Magnetics had developed its own classification algorithms in the context of developing an advanced portal for concealed weapon detection. An initial look at that algorithm—performed at Quantum’s expense, and hence not part of this formal report—suggests that the data provide more discriminatory power than the Duke algorithms were able to use. The concept of multi-axis, broadband response measurements may yet enable significant remediation cost reductions via improved target-clutter discrimination.

1 Implement the improved transmitter amplifier and the ferrite calibration method on the SERDP system for subsequent measurements.

1.1 Improved Transmitter Amplifier

In the closeout proposal, we proposed to borrow a new, improved transmitter amplifier from an internal program and use it in conjunction with the rest of the SERDP system for measurements in the proposed work. We ended using the new power amplifier designed for the Army landmine contract. The new transmitter amplifier design injects less noise into the system than the existing amplifier and thus produces cleaner excitation waveforms. However, while testing the efficacy of the power amplifier in the system, it failed due to a critical sense pin, used in part to protect the amplifier, which had a bad solder joint that led to the failure. We have only recently completed the repair of the power amplifier and have not tested it yet in the system. In the meantime, we decided to proceed and carry out the work with the existing power amplifier due to time constraints.

1.2 Ferrite Calibration and Correction

The ferrite calibration for the frequency-domain system was also investigated. Since ferrite is purely ferromagnetic and nonconductive, it produces a negative constant in-phase (real part) response and a zero quadrature (imaginary) response at all frequencies. Using it to baseline the system response may help calibrate out spurious inductive effects present in the response curve, particularly at high frequencies, by performing a phase adjustment. In other work, we have obtained good success utilizing a ferrite toroidal core to calibrate out broadband systematic phase errors in inductive pickup systems. By measuring the phase error at each frequency and then correcting it at the receiver, one can account for the systematic phase errors. Once phase correction is applied, subsequent measurements of the ferrite core yield classic response curves and the system is calibrated.

In the FD system we operate the magnetoresistive (MR) sensors near the center of the excitation coil, in high axial field. To accomplish this, we wind a small bucking coil around the sensor and drive current in it to null the source field at the sensor. Phase and amplitude must both be accurate to attain an effective null. Perfect phase matching is difficult because the error signals are small and extraction of phase numerically from small signal levels can lead to inaccuracies. Given that, we get fairly good matching except at the lowest and highest frequencies. As an example, measurement of a brass ring should produce an ideal L-R response, but as shown in Figure 1, the response departs from expected at higher frequencies in both components. The quadrature response fails to trend toward zero at high frequency, and the in-phase response does not trend to a constant asymptote.

We attempted to use the ferrite core technique to calibrate out the errors. Figure 2 shows the raw response of the ferrite core without system background subtraction (see Section 2.2.1 for a discussion of measurement procedure and background subtraction). Figure 3 shows the same response with background subtraction. It is clear that the quadrature response departs at low and high frequencies from the expected zero value. We measure the phase correction required to bring the quadrature response at each frequency to zero and apply the corrections to both in-phase and quadrature components. Figure 4 shows the uncorrected and corrected response curves and Table 1 lists the phase required to attain the expected zero-phase quadrature response.

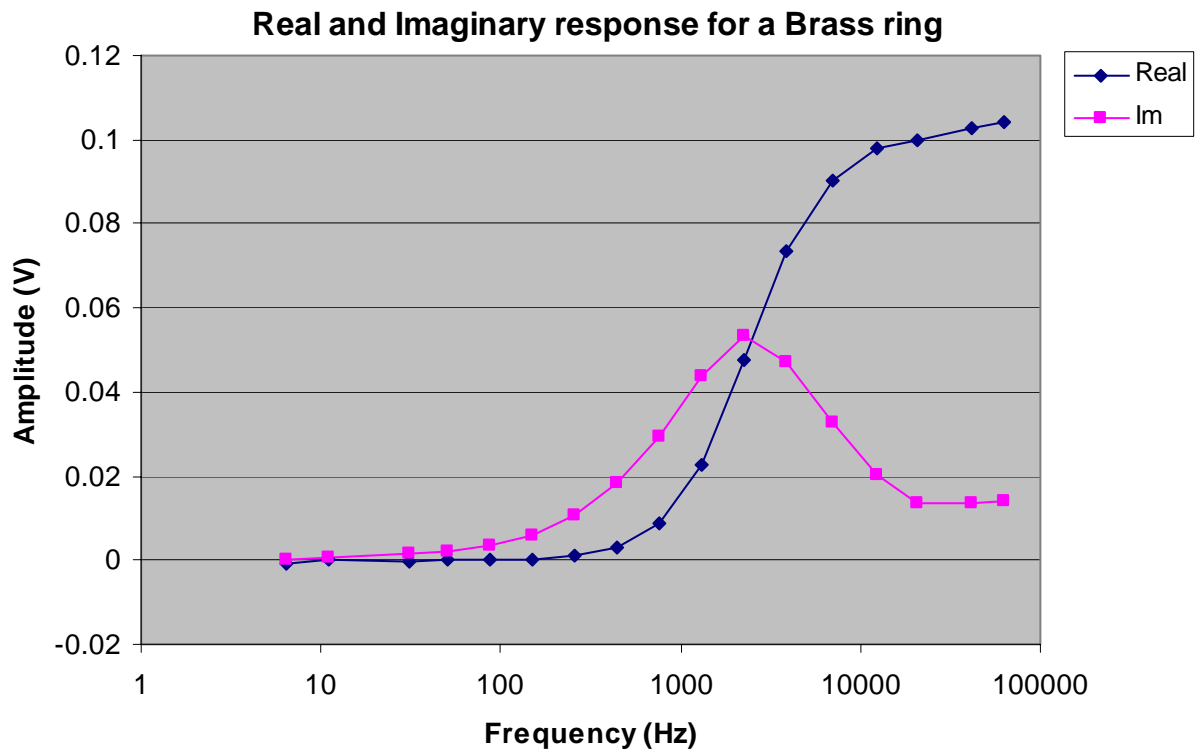


Figure 1. Response of a brass ring showing high-frequency errors.

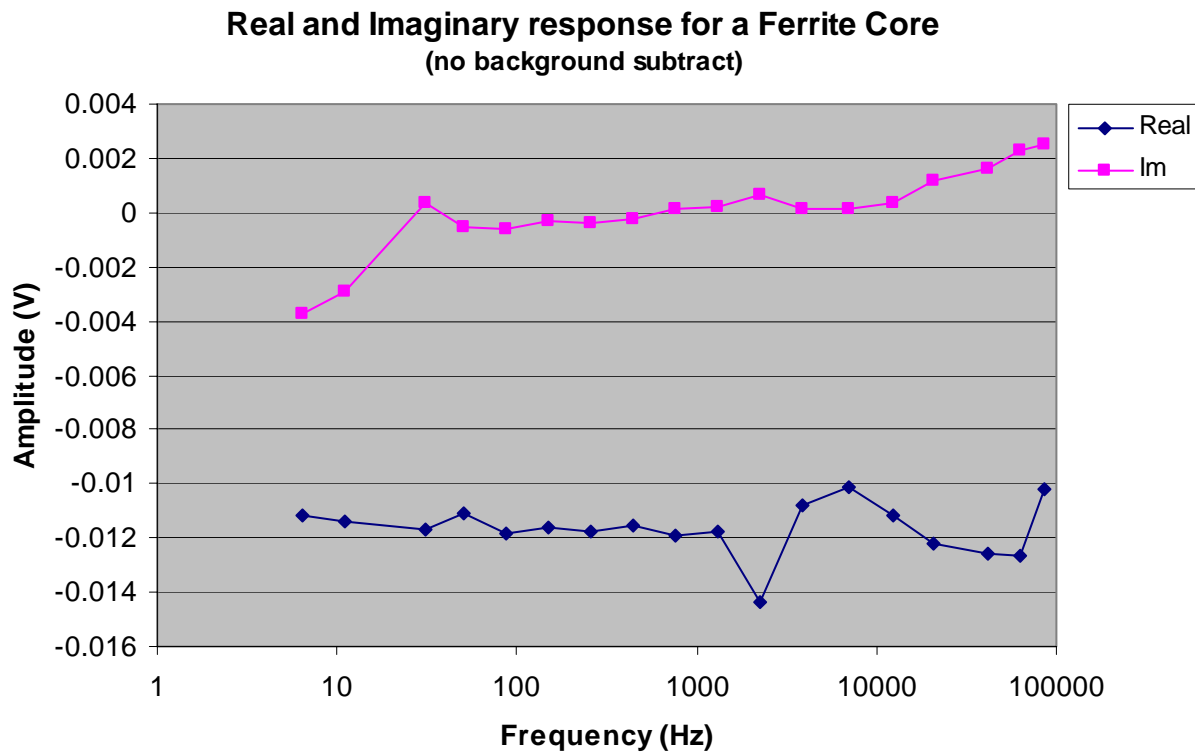


Figure 2. Response of a ferrite toroidal core without background subtraction.

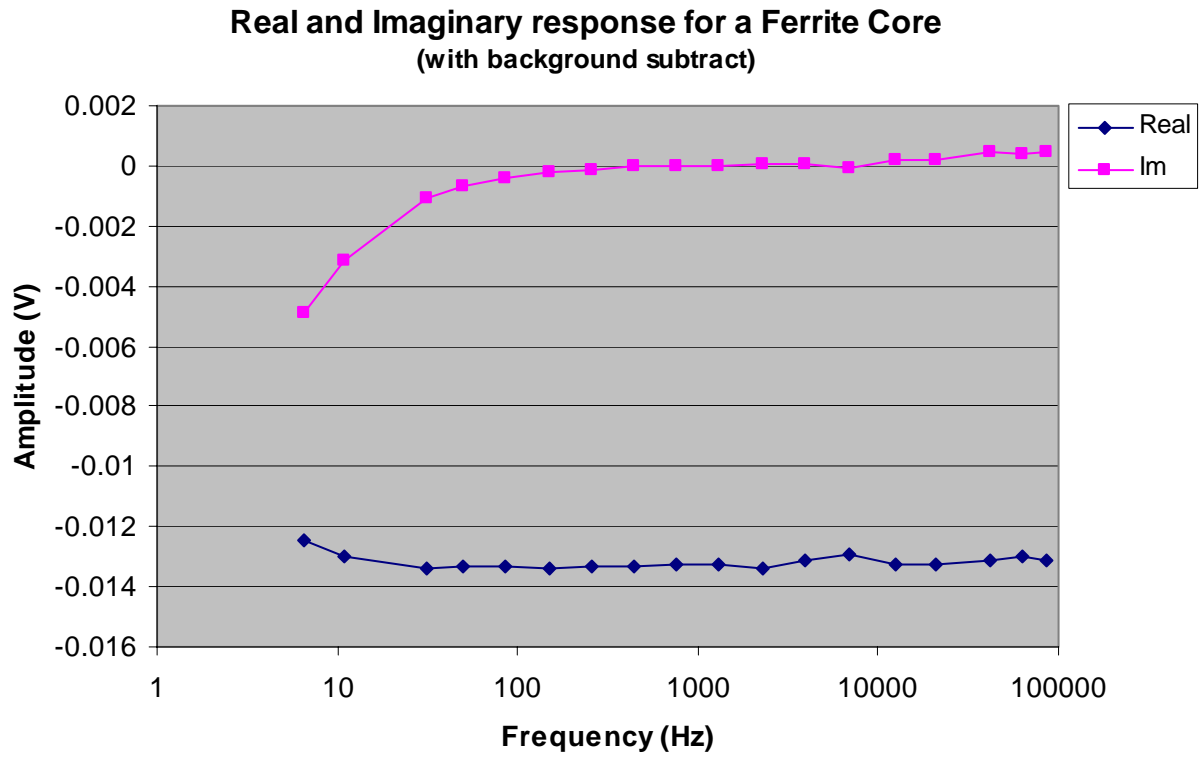


Figure 3. Same ferrite core response with background subtraction.

Frequency (Hz)	Phase Correction (°)
6.49	21.38
10.91	13.53
31.00	4.54
50.08	2.85
86.37	1.89
149.47	0.98
254.92	0.68
446.43	0.16
762.19	0.15
1302.08	0.09
2272.72	-0.27
3906.26	-0.26
6944.43	0.24
12500.00	-0.81
20833.35	-0.78
41666.66	-2.05
62500.03	-1.66
85034.26	-1.98

Table 1. Phase correction vs. frequency as determined from ferrite core data.

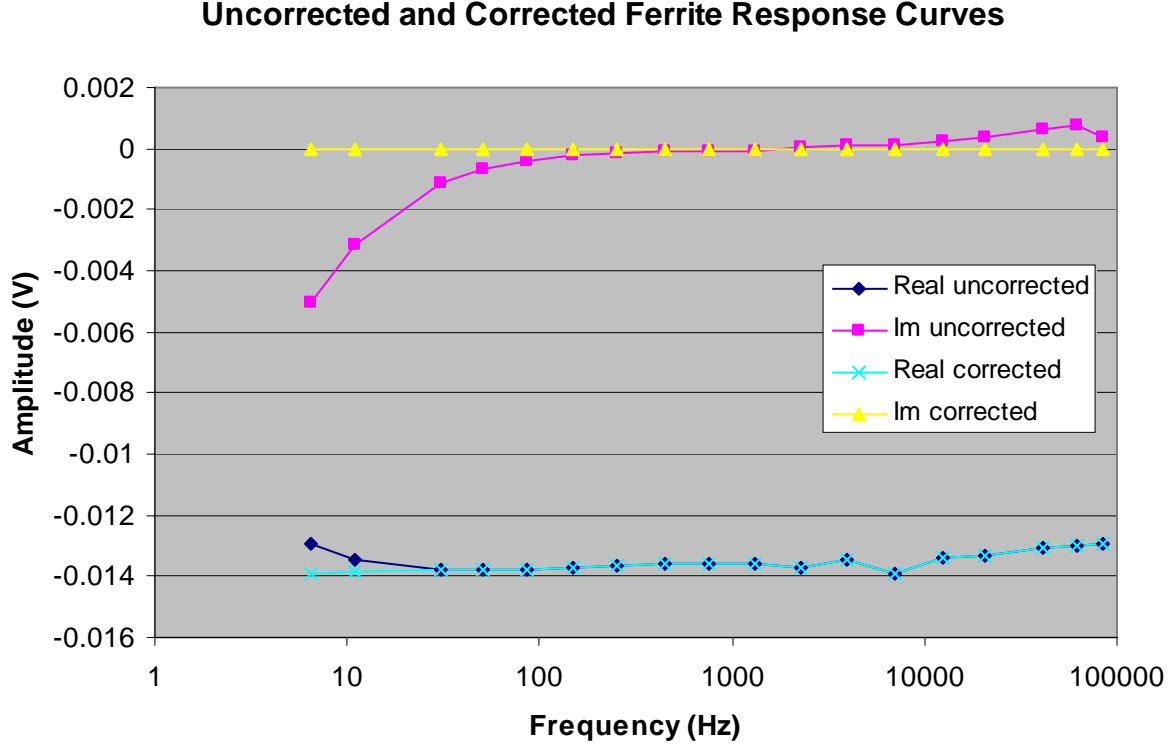


Figure 4. Phase-corrected ferrite response curves.

Although Figure 4 shows that the quadrature response is nulled, the high-frequency departure of the in-phase response from the expected constant value is not corrected at all. In fact, the in-phase ferrite response is unaffected by the phase correction at high frequencies: phase correction in this manner is ineffective.

We verified that applying the same phase correction to the brass ring data of Figure 1 hardly changes either the in-phase or quadrature response at high frequency. For this reason, we did not apply the phase correction to subsequent UXO and clutter data sets.

At this time the cause of the systematic response errors is still uncertain. Given the constraints on remaining project funding, it was decided to curtail the search for the cause in the interest of obtaining and analyzing UXO data within the project budget. If the phase (and/or gain) errors are consistent from one data set to the next, they should not affect the utility of the data for discriminating between UXO and clutter.

2 Measure MR-sensor system noise across the system bandwidth and cancellation of the primary field using improved transmitter amplifier.

2.1 MR Sensor Noise Characterization

We characterized the noise performance of the sensor in the standard way. First, we calibrated the system by injecting a pilot tone of known field magnitude and measuring the through-response to establish a field to voltage transfer function. Then we measured the voltage noise

floor, converted it to spectral density and finally converted to field noise spectral density via the transfer function.

We drove the source coil with a signal of amplitude $V_{in} = 0.200 \text{ V}_{p-p}$ at a frequency $f = 147.0 \text{ Hz}$. The source coil current was measured using the arrangement depicted in Figure 5. At this frequency, the reactance of the source coil is in the sub-milliohm range and is negligible compared to the $4.4 \text{ } \Omega$ current-monitor resistor. We lose no accuracy in assessing the circulating coil current using this method.

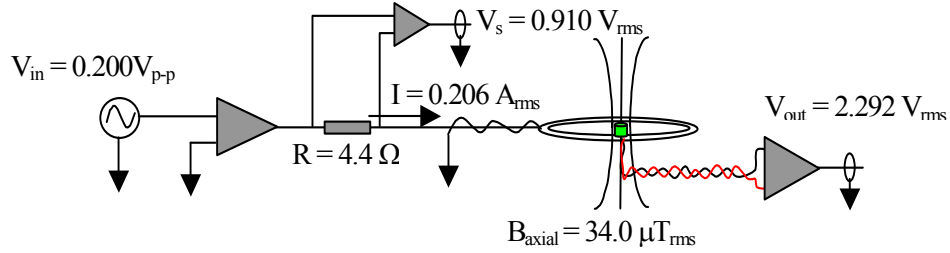


Figure 5. Experimental arrangement used to measure the system noise.

The sense voltage $V_s = 0.910 \text{ V}_{rms}$ yields a coil current $I = V_s/R$ which evaluates to be $I = 0.910 \text{ V}_{rms}/4.4 \text{ } \Omega = 0.206 \text{ A}_{rms}$. To find the injected B-field, we employ the in-plane axial field equation for the source coil given by

$$B_{axial} = \frac{\mu_o NI}{2r}$$

Our coil design has $N = 4$ turns and radius $r = 6.0 \text{ in} = 0.1524 \text{ m}$. Using these values in the field equation gives

$$B_{axial} = \frac{4 \cdot \left(4\pi \cdot 10^{-7} \frac{T \cdot m}{A} \right) (0.206 A_{rms})}{2 \cdot (0.152m)} = 34.0 \mu T_{rms} .$$

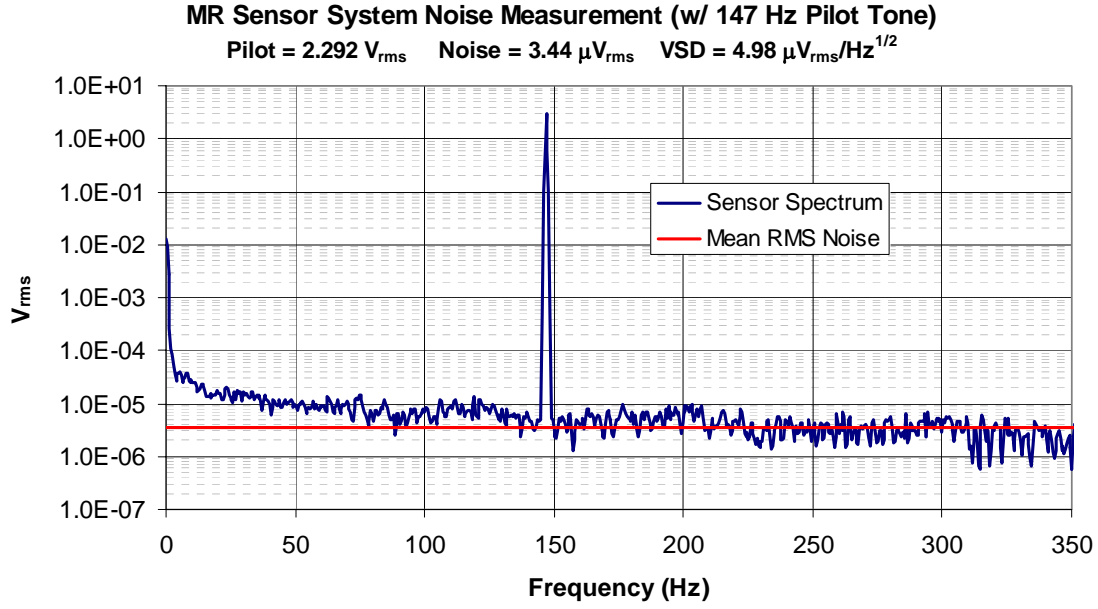


Figure 6. MR sensor calibration and noise measurement plot.

The voltage response of the system was measured to be $V_{out} = 2.292 V_{rms}$ resulting in a transfer function given by

$$TF = \frac{2.292 V_{rms}}{34.00 \mu T_{rms}} = 0.06741 \frac{V}{\mu T}$$

Next, we measure the averaged broadband voltage noise spectral density with the source input set to zero and obtain

$$V_n = 4.98 \frac{\mu V_{rms}}{\sqrt{Hz}}$$

We find the magnetic field noise spectral density

$$B_{noise} = 4.98 \frac{\mu V_{rms}}{\sqrt{Hz}} \cdot \frac{1}{0.06741} \frac{\mu T}{V} = 73.87 \frac{pT_{rms}}{\sqrt{Hz}}$$

This result establishes a limit to the minimum level magnetic signal we are capable of measuring in a finite sampling interval with equivalent averaging. Depending on the signal sampling rate and number of points, the absolute field limit can be determined.

This result applies to both frequency domain and time domain implementations of the sensor.

2.2 Frequency-domain (FD) system

2.2.1 System Description and Operation

The frequency domain system is depicted in the schematic diagram of Figure 7 and its specifications are presented in Table 2. Noise performance of the sensor is discussed in a later section.

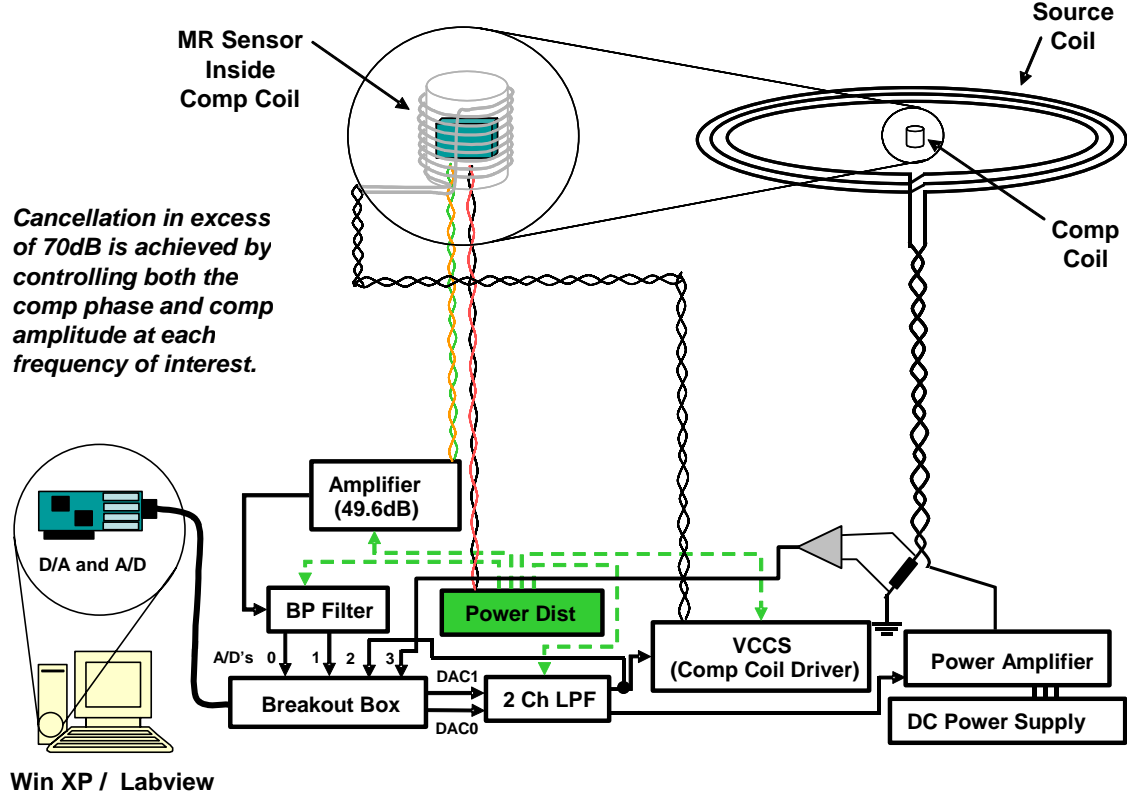


Figure 7. Block diagram of the FD system.

COMPONENT	FUNCTION
Breakout Box	Provides connectivity between acquisition board and system hardware
2 Channel Low Pass Filter	$f_{\text{cutoff}} < 2f_{\text{source}}$, these filters smooth the D/A-generated waveforms that drive the source and compensation circuits
Power Amplifier	Provides broadband high current to source coil
VCCS	Voltage Controlled Current Source that drives the compensation coil
Amplifier (49.6dB)	Differential In/Single-Ended Out with 49.6 dB gain and flat response across full band of interest: boosts output of MR sensor
Bandpass Filter	BP filter: $f_L = \sim 2 \text{ Hz}$; $f_H = \sim 1.7 \text{ MHz}$; gain of 3 dB flat across pass band
Power Distribution	Provides $\pm 12 \text{ Vdc}$ and $\pm 5 \text{ Vdc}$ to the various circuits above
DC Power Supply	Supplies $\pm 48 \text{ Vdc}$ / $\pm 12 \text{ A}_{\text{max}}$ to the power amplifier
D/A and A/D Board	High speed D/A and A/D board (via Labview™ programming) drives both the compensation coil and the source coil and digitizes the output of the BPF (MR boost) and the voltage across the source coil current sense resistor
Win XP/Labview	Labview running under Windows XP controls (via A/D and D/A board) source field and compensation field (both amplitude and phase accurately)
MR Sensor	Honeywell™ Magneto-Resistive multi-axis sensor, Model HMC1002
Source Coil	Produces B-field to elicit eddy current response from the target
Compensation Coil	Produces B-field to cancel the source field at the location of the MR sensor (weakly coupled to the source coil)

Table 2. Functional description and specification of FD system components.

The system uses stepped frequencies, as given in Table 1. We must produce a magnetic null at the sensor for each frequency. This involves matching amplitude and phase at each frequency of operation. Table 3 presents the calibration algorithm used in human-readable “pseudo-code”.

```

Begin: # amplitude and phase compensation calibration
Set Freq to  $f_{max}$ 
Set Comp Control Voltage (CCV),  $v_{cc} = 0$ 
Set Source Control Voltage (SCV),  $v_{sc}$ 
Adjust to max response to obtain,  $V_{sc}$ 
Record  $v_{sc}$  and  $V_{max}$  #corresponding to highest field we can achieve given high
                        # frequency impedance load limitations

# Now let's iterate through frequencies to obtain nulling parameters
For  $f_i$  in ( $f_1, f_2, f_3 \dots f_m$ ):
    Set source_match_cond_met = comp_match_cond_met = false
    Set Freq  $f_i$ 
    Set CCV off
    Set SCV =  $v_{sc,i}$ 
    While (source_match_cond_met == false):
        If ( $V_{max} - V_{s,i}$ ) <= acceptable null threshold (~0.002 Volt):
            Set source_match_cond_met = true
            Record  $v_{sc,i}$  and  $V_{s,i}$ 
            Set SCV off
            Set CCV =  $v_{cc,i}$ 
            While (comp_match_cond_met == false):
                If ( $V_{max} - V_{c,i}$ ) <= acceptable null threshold (~0.002 Volt):
                    Set comp_match_cond_met = true
                    Record  $v_{cc,i}$  and  $V_{c,i}$ 
                    Meas_rel_phase_diffs( $\phi_{c,i}, \phi_{s,i}$ )
                    Set  $\phi_{c,i} = \phi_{s,i} + \pi$ 
                    Set SCV =  $v_{sc,i}$ 
                    Set CCV =  $v_{cc,i}$ 
                    Set  $\phi_{c,i}$ 
                    Meas_atten_level (dB)
                    Append_cal_values_to_file ( $f_i, v_{sc,i}, v_{cc,i}, \phi_{c,i}, \phi_{s,i}, dB$ )
                Else:
                     $v_{cc} = v_{cc} + \beta(V_{max} - V_{c,i})$  # feedback prop to error
            Else:
                 $v_{sc} = v_{sc} + \alpha(V_{max} - V_{s,i})$  # feedback prop to error

End: # System is now calibrated in amplitude and phase

```

Table 3. System calibration algorithm in “pseudo-code”.

Figure 8 shows the Labview user window for the calibration procedure for the two-axis sensor. It displays the status and the compensation values as they are determined by the algorithm of Table 3. Of the quartet of graphs in the upper left of the display, the lower left shows the current drive needed to null the earth's field at the sensor. The upper leftmost graph displays the source drive matching minimization; as the algorithm iteratively approaches the solution, the residual tends toward zero. The two right-hand graphs of the quartet show the drive values of the compensation coil. The pair of graphs at the lower right of the display show the phase of the compensation coil drive which approaches 90° as the source field is nulled.

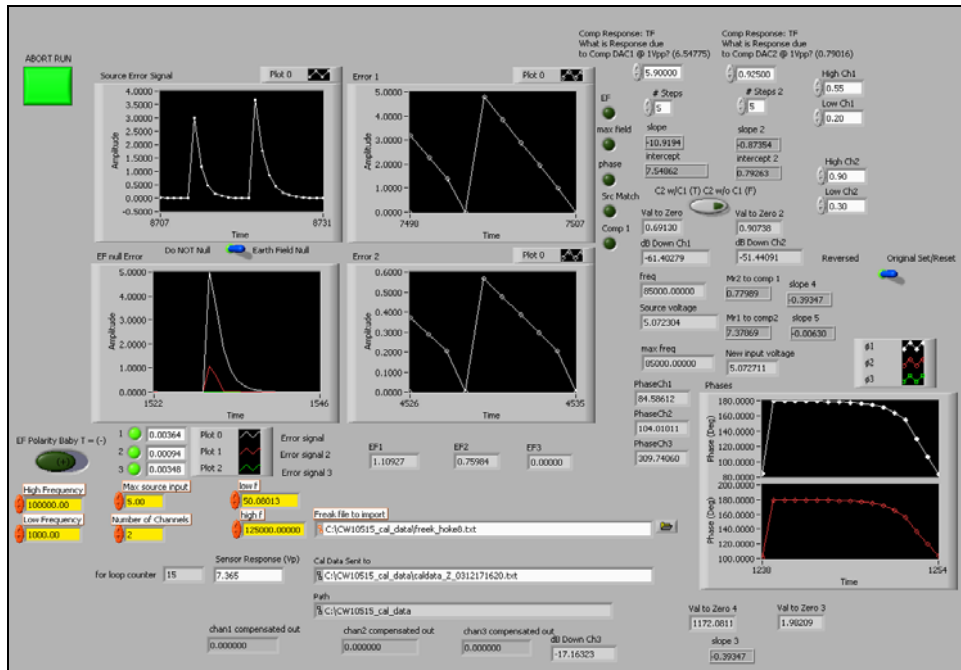


Figure 8. Example of a two-axis sensor calibration window during auto-calibration.

Once the calibration sequence completes, the software presents a review window to see how well the calibration did. Figure 9 is an example of a single-axis review window. The left-hand graphs show the calculated transfer function as a function of frequency; the upper right-hand graph shows the DAC output gain; and the lower right-hand graph shows the resulting attenuation of the source coil field, with a numerical display of the average attenuation, in dB, below.

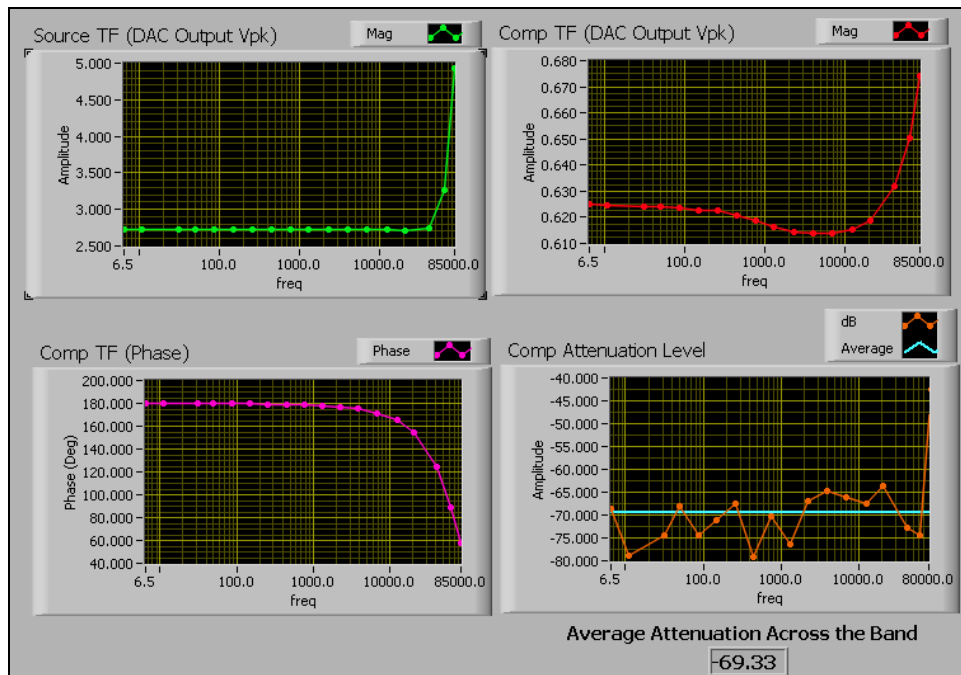


Figure 9. Compensation review window (single-axis sensor example).

Prior to measuring a target, we perform a background (or null target) measurement, stepping through the frequencies. We generally collect a second set of background data and subtract it from the first. If the subtraction yields a null, that indicates that the system is working properly. If not, we repeat the background run. With a target in place we collect data. We then subtract the background from the target data, yielding only the perturbations related to the target as shown in Figure 10 for a typical target run. The Figure shows, in the large left-hand panel, the in-phase (green) and quadrature (red) target response, together with the scalar amplitude response (blue). We produce in-phase and quadrature data and save the run-specific data to a file. This includes amplitudes, phases, frequencies, raw data, subtracted data and the like for each sensor axis.

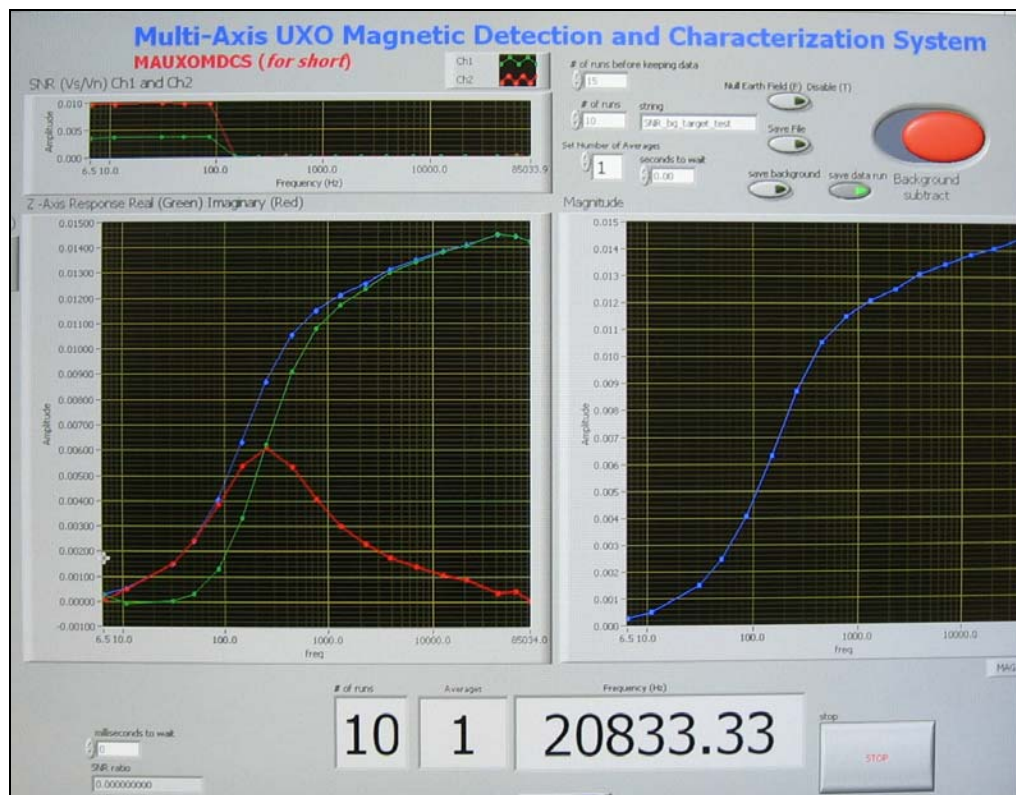


Figure 10. Target response function after subtracting instrumental background.

2.2.2 Hardware modifications

We modified the cable connecting the source coil to the amplifier. We also switched from a wire with twisted pair to a wire with twisted quad, in order to reduce the cable inductance by roughly 50%.

As mentioned above, an unsuccessful attempt was made to switch the previous power amplifier and use the latest PA05 power operational amplifier design currently used in a system developed in another project for landmine detection.

2.2.3 Software development

Calibration software

The calibration routine that we implement steps through each drive frequency to determine the compensation field values needed to null the source field. During further assessment of the

method, we determined the system Transfer Function (TF). It was found that the process could be further optimized to determine more accurate compensation values. After establishing a more accurate TF response, we now obtain an average cancellation of 69 to 70 dB across the frequency band. Our previous best was 60 dB. These results are summarized in Figure 11.

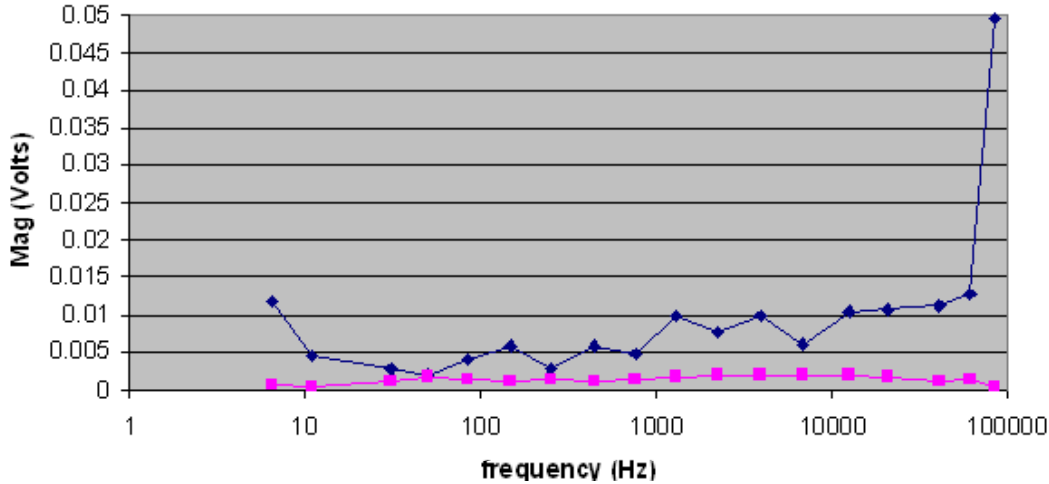


Figure 11. System noise with source field compensation between 10 Hz and 100 kHz showing improvement between the new (red squares) and old (blue diamonds) methods.

Temperature drift characterization

It had been observed that, from run to run, there was some variance in acquired background or null run acquisitions. We pursued two options for addressing this drift. The first was to allow sufficient time between runs enabling all electronics to cool down. The second was to run repeatedly back-to-back essentially heating up the system to an equilibrium point (running hot). Comparing the data sets for various cool down times versus the data sets running the system repeatedly, it was clear that running the system hot produced the most repeatable results. As a result, we now collect larger data sets throwing out the first 15 runs or so and averaging the data we consider to be taken at the equilibrium temperature.

Background subtraction

Applying the temperature drift reduction method discussed above, we now have a greatly improved background subtraction. Previously we collected an averaged background containing a drift component. This was then subtracted from data, which also included a drift component. Now collecting background and target data free from the drift component, we are able to achieve a substantially better background subtraction, essentially improving our system noise floor. Figure 12 shows the noise floor measured at each drive frequency between 10 Hz and 100 kHz measured with field compensation on and no target.

It is worth noting, however, that this is not a realistic way of running the system in the field. Ultimately, it would be essential to address the temperature drift of the PA05 amplifier, which we suspect to be the source of the temperature drift problem.

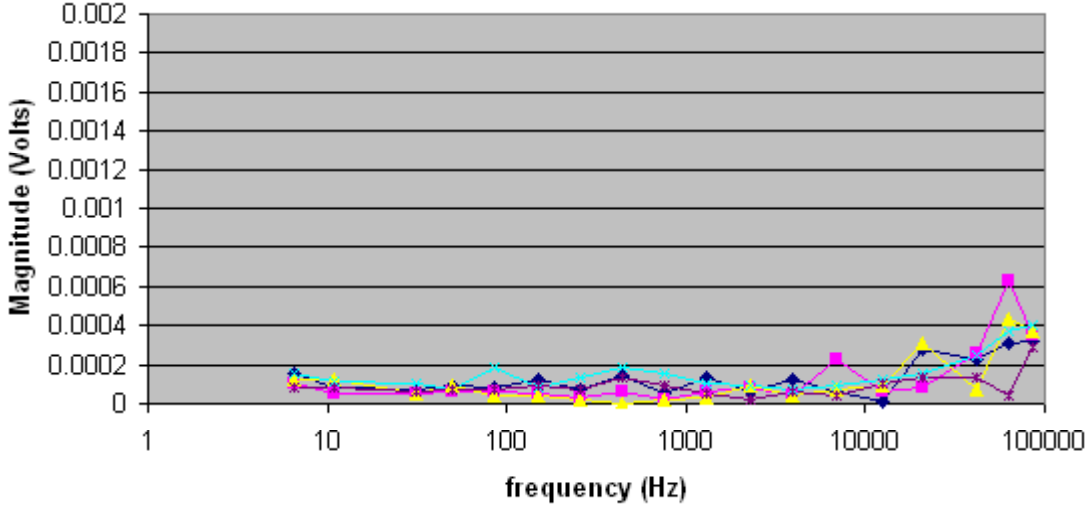


Figure 12. FD system noise floor as a function of frequency.

Signal-to-noise ratio (SNR) computation algorithm

The total energy in a spectrum can be approximated by the sum of signal energies from each of the contributing frequencies in that spectrum. In this calculation, the signal is the magnitude of the sensor output before it is decomposed into in-phase and quadrature components. The approximation approaches the exact value for a very large number of frequencies in a finite bandwidth. The SNR definition that we adopt in this work is the ratio of signal power to noise power or equivalently the ratio of signal energy to noise energy:

$$\text{SNR} = P_s/P_n = E_s/E_n. \quad (1)$$

To compute the energy in a signal at a given frequency, one must divide the signal power by the spectral bin width, which depends on the sampling time. We collect data at 18 frequencies with variable sampling rate. For each frequency, we sample at a different rate f_s but with a fixed number of samples, N , thus using a variable sampling time. In each case, the spectral bin width is $f_s/N = \Delta f$. For 18 frequencies, we then have 18 corresponding bin widths. We could estimate the total energy in the operational bandwidth but that would be less than suitable given that we have 85 kHz of bandwidth but only 18 frequencies. To address that, we interpolate both the signal and the spectral bin width data sets. With the *a priori* knowledge of the structure of the signal amplitude envelope across the band, the noise, and the variable bin width curve, we can easily perform the interpolation and generate 85,000 signals and 85,000 spectral bin widths across the bandwidth. The interpolation allows us essentially to perform a numerical integration to compute the total energy across the band for the signal as well as the noise spectra.

Each energy (ignoring the impedance since the SNR ratio will eliminate it) term is computed as

$$e_i = \frac{V_i^2}{\Delta f_i}. \quad (2)$$

The energies are then summed up

$$E_s = \sum_{i=1}^k e_{si} = \sum_{i=1}^k \frac{V_{S_i}^2}{\Delta f_i}, \quad (3)$$

where $k = 85000$. Next, we do the same thing for the noise spectrum with the noise energy collected in the absence of a target.

$$E_n = \sum_{i=1}^k e_{ni} = \sum_{i=1}^k \frac{V_{n_i}^2}{\Delta f_i}, \quad (4)$$

and finally we compute the energy ratio

$$SNR = \frac{E_s}{E_n}. \quad (5)$$

This is the classic Signal-to-Noise ratio and is typically a ratio of powers (energies). We can take the square root of this if we wish to express our SNR in terms of signal voltage to noise voltage

$$SNR_v = \sqrt{SNR_p} = \sqrt{\frac{E_s}{E_n}} \quad (6)$$

We used a single turn copper ring at 3 inches above the sensor and measured its response. We repeated this for twice the standoff, corresponding to $2^3 = 8$ reduction in signal for a dipole-like sample. We then computed the SNR in each case.

Standoff	SNR _{Power}	SNR _{Voltage}
3 in	3487.0	59.0
6 in	54.9	7.41

The reduction in SNR_v is $59.0/7.41 = 7.96 \cong 8$, which confirms that (1) the estimate of the relative signal strength, determined from the integrated energy, is correct, and (2) the noise energy is not dependent upon the presence of a target. If it had been, we would not have obtained the 1:8 reduction.

2.3 Time-domain (TD) system

2.3.1 System Description and Operation

The time domain system is depicted in the schematic diagram of Figure 13 and described in Table 4.

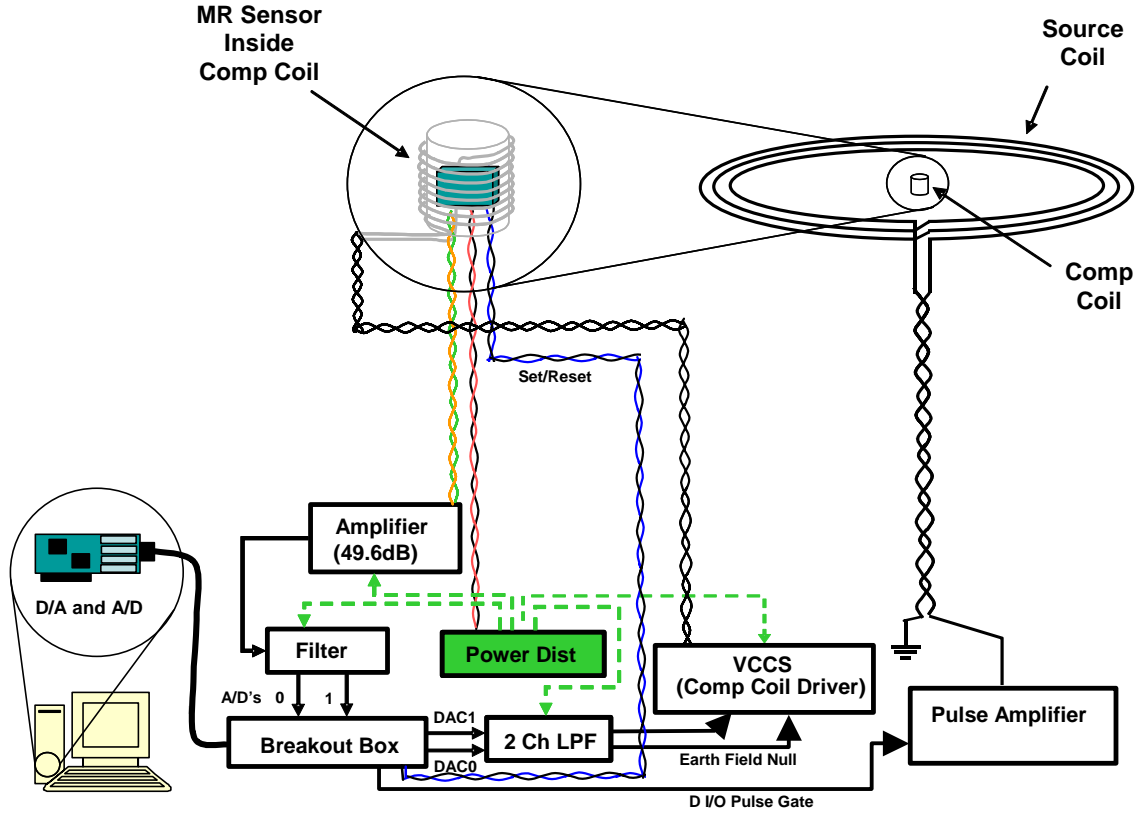


Figure 13. TD system block diagram.

COMPONENT	FUNCTION
Breakout Box	Provides connectivity between acquisition board and system hardware
2 Channel Low Pass Filter	$f_{\text{cutoff}} < 2f_{\text{source}}$, these filters provide a quiet DC signal to drive the compensation circuits
Pulse Amplifier	Provides pulsed power to source coil
VCCS	Voltage Controlled Current Source that drives the compensation coil
Amplifier (49.6dB)	Differential In/Single-Ended Out with 49.6 dB gain and flat response across full band of interest: boosts output of MR sensor
Band Pass Filter	BP filter with $f_L = \sim 2 \text{ Hz}$; $f_H = \sim 1.7 \text{ MHz}$; gain of 3 dB flat across pass band
Power Distribution	Provides $\pm 12 \text{ Vdc}$ and $\pm 5 \text{ Vdc}$ to the various circuits above
DC Power Supply	Supplies $\pm 48 \text{ Vdc}$ / $\pm 12 \text{ A}_{\text{max}}$ to the power amplifier
D/A and A/D Board	High speed D/A and A/D board (via Labview™ programming) drives the DC Earth's Field compensation coils, drives the Set/Reset, drives the Pulse Gate and digitizes the output of the BP filter, the signal of interest
Win XP/Labview	Labview running under Windows XP controls (via A/D and D/A board) source pulse field and DC Earth's Field compensation, collects and processes TD data.
MR Sensor	Honeywell™ Magneto-Resistive multi-axis sensor; Model HMC1002
Source Coil	Produces Pulsed B-field to elicit transient eddy current response from the target
Compensation Coil	Produces B-field to cancel the Earth's field at the location of the MR sensor (weakly coupled to the source coil)

Table 4. Functional description and specifications of TD system components.

The Time Domain system is relatively simple in principle. The MR sensor must be forced into favorable magnetic domain alignment prior to every measurement to insure repeatability. We facilitate this with the sensor set/reset strap and driver hardware controlled by Labview. The set/reset pulse is shown in Figure 14. Figure 15 shows the pulsed field ramp for each of the two cases of a set or reset *state* to demonstrate the phase reversal of the output. Once the sensor magnetic domains have been realigned, we initiate a measurement by enabling the pulse gate, which then turns on the pulse driver, essentially shorting the source coil across a charged bank of capacitors. Once the pulse gate is turned off we acquire data of the eddy current decay. We average several pulses back to back with set/reset operations in between each excitation pulse. This becomes our background time series. Then we measure a target. We subtract the background from the target response and repeat to obtain averaged results. A typical run is shown in Figure 16. The critical issue here is the reproducibility of the pulse gate sequence and timing. This is accomplished with sufficient reproducibility through Labview.

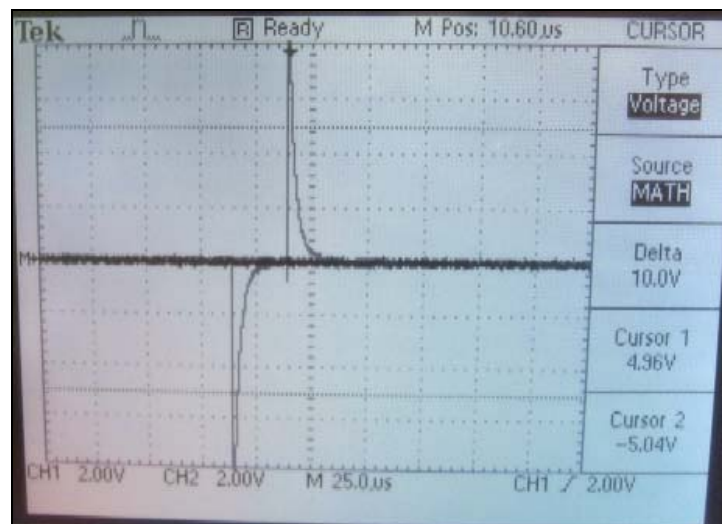


Figure 14. Symmetric set/reset pulses.

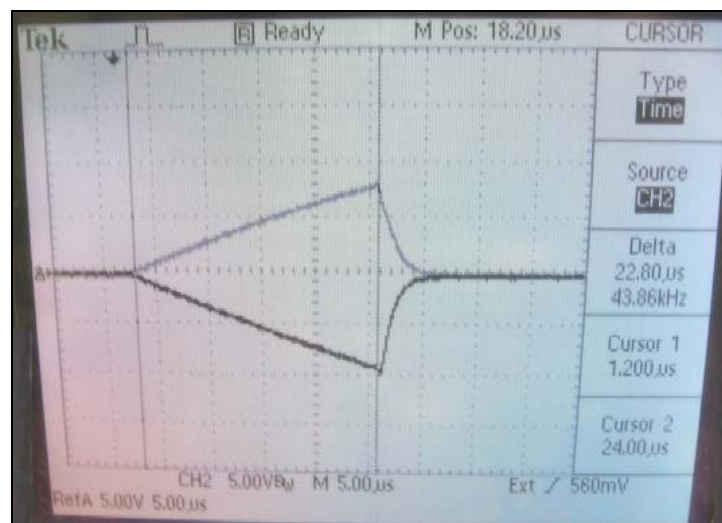


Figure 15. Pulsed source field ramps, showing alternating symmetry (traces superimposed for display purposes).

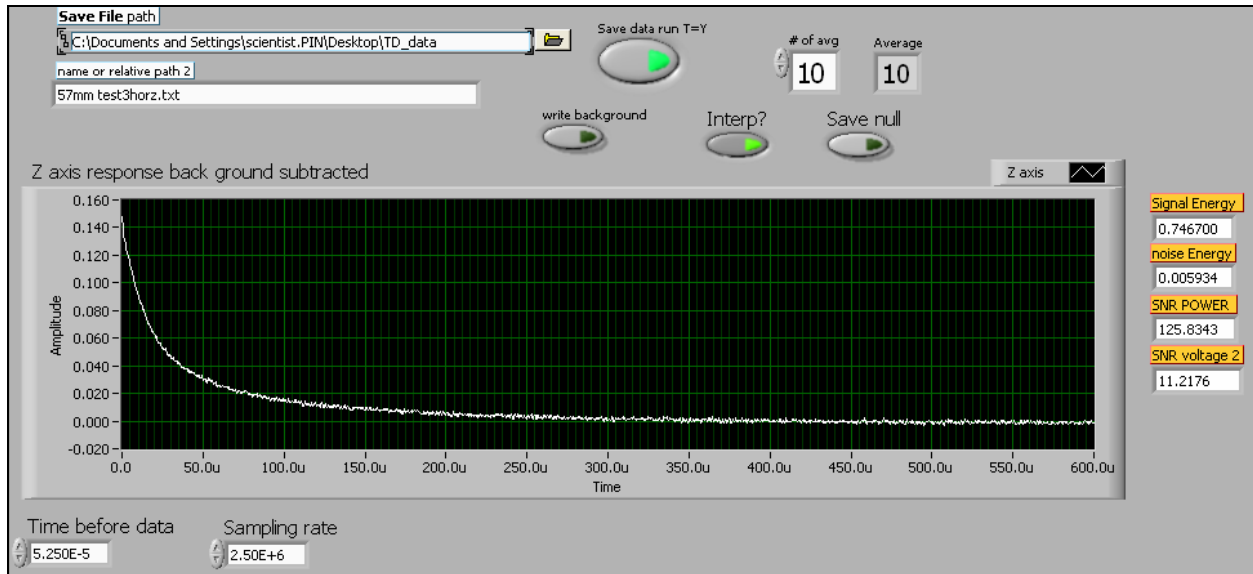


Figure 16. Typical TD background-subtracted response output.

2.3.2 Hardware modifications

While testing the system, we noticed an asymmetry in the magnetic field generated by our source coil as the polarity is switched to apply the field in opposite directions. Field switching is typically performed by pulsing the coil in one direction and acquiring data, then pulsing the coil in the opposite direction while switching the polarity of the sensor, and taking data again. The two resulting data sets are then summed to remove any electronics offsets. However, the asymmetry adds noise to the signal instead of removing it. Rather than spend time and resources to try to diagnose and fix the problem, we decided to apply the field only in one direction and remove any remaining DC offset in software.

The Set/Reset (S/R) pulse was also improved to insure that the sensor return repeatably to its highest sensitivity state after it is hit with the large source field. The initial S/R redesign used two ultra low resistance dual channel MOSFETs in order to produce a tightly controlled turn-on and turn-off S/R pulse. The motivation is to return the sensor to its highest sensitivity state in the shortest time possible in order to start recording the response field of a target as early as possible. The redesigned S/R allows tight control of the S/R pulse length and the ability to turn it off sharply (essentially creating a square pulse) and quickly remove the longer decay from the original design, as shown in Figure 17.

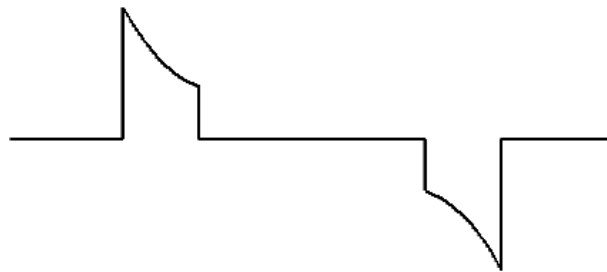


Figure 17. Original S/R pulse

From run to run, however, we observed that the sensor does not always return to the same sensitivity state after a S/R. This issue was resolved by recognizing that the original “square” S/R pulse was actually setting the magnetic domains with the initial spike but then unsetting them with the harsh falling-edge transition of the pulse, yielding varied sensitivity states. We solved this problem by putting a capacitor in series with the S/R strap on each side. This allows the S/R spike to discharge smoothly to zero without disturbing the alignment of the domains, as shown in Figure 18.

Additionally, we increased the value of the power resistor in series with our source coil. This enabled us to decrease the time it takes the current to fully decay from the coil. Currently, it takes 4.2 microseconds to completely drain the current from the coil and start the measurements, as shown in Figure 19.

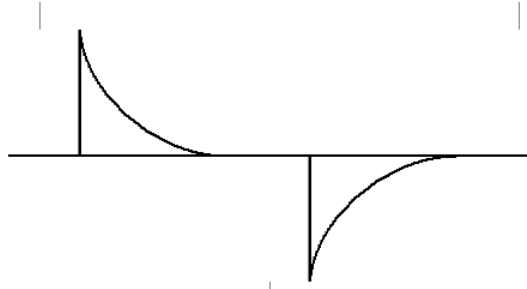


Figure 18. Improved S/R pulse.

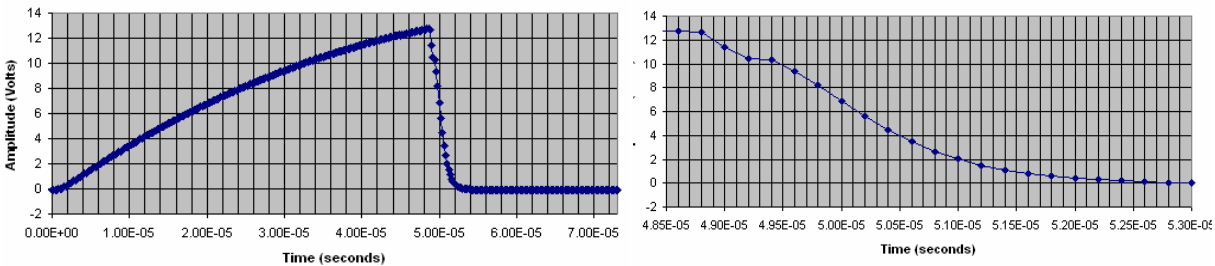


Figure 19. Left: Sensor output as a function of time as the capacitors dump charge into the coil. Right: Detailed view of the current decaying from the source coil. It takes 4.2 microseconds for the sensor output to go from its maximum to zero.

To simplify the sensor operation, we now apply the S/R only before the source pulse. We examined the sensor output for several runs without using a S/R after the field pulse and saw no saturation of the sensor, which has a dynamic range of ± 2 gauss. Not applying a S/R after the source field pulse also allows us to start taking data even earlier than before.

2.3.3 Software development (V. 3)

Acquisition

After developing a much better understanding of the system hardware, we developed a new sequence for the TD data acquisition. First, we null the earth’s field by sending a DC voltage to the sensor’s offset strap. Second, we hit the sensor with a Set/Reset/Set to return it to the same sensitivity as before the run. Third, we pulse the coil. Fourth, we acquire the data without target (background) and with target. And fifth, we average the data by repeating steps 2 through 4,

summing the results, and dividing by the number of runs. The background data is thus subtracted from the target run.

Removing DC offsets

Each data set is in effect a decay curve. The initial amplitude decays in time to an asymptotic value. We select a window of data that is in the asymptotic regime, average the data in that window, and consider the average value as the DC offset. We then subtract that value from each data point in our data set.

Triggering data acquisition after initial pulse

We start collecting data on the rising edge pulse, which allows us to observe the full field behavior. Data can also be collected on the falling edge of the pulse. The collected data exhibited interesting behavior. There is a delay of 3.8 microseconds between the closing of the FET and the current beginning to drain off through our power resistors

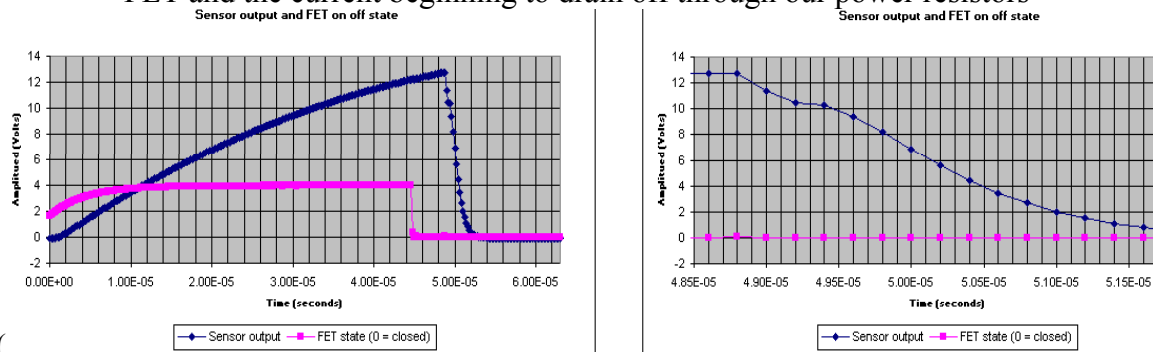


(Figure 20: left). Additionally there is a distinct hump characteristic to the field decay curve

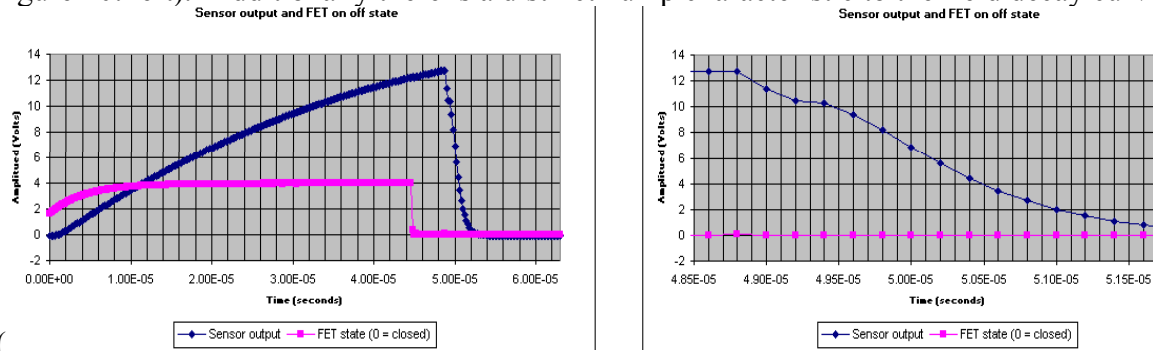


(Figure 20: right).

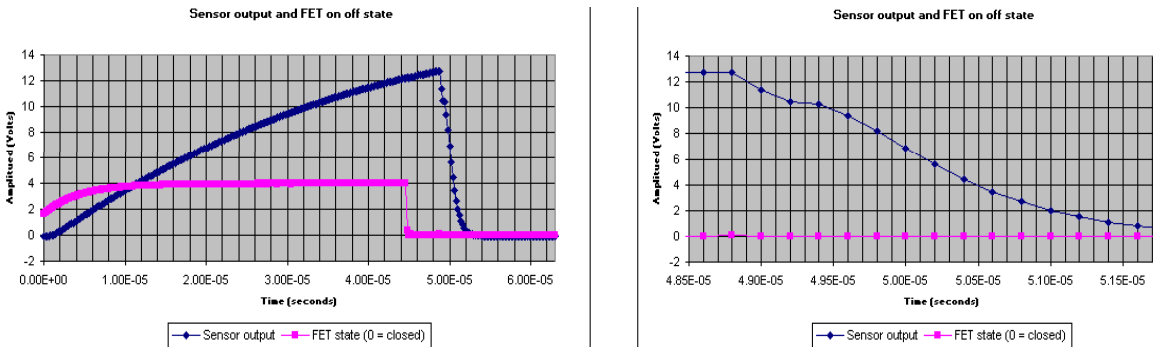


Figure 20. Left: Sensor output while FET is open and then closed. Right: expanded view, showing details during current drainage.

We can start collecting data 49.6 microseconds after the start of the source field pulse, which is approximately 0.8 microseconds after the current begins to drain out of the coil. However, in order to improve the A/D resolution and in turn the averaging, we choose to wait until the sensor output is at or below 2 Volts. This only requires us to wait 2.2 microseconds (instead of 0.8) after the current begins to drain out of the coil.

SNR computation algorithm

The total energy in a spectrum can be approximated based on the sum of energies from each of the contributing frequencies in that spectrum. The approximation approaches exactitude for a very large number of frequencies in a finite bandwidth. The SNR, by definition, is the ratio of signal power to noise power, which is equivalent to the ratio of signal energy to noise energy.

$$\text{SNR} = P_s/P_n = E_s/E_n \quad (7)$$

To compute the energy in a signal at a given frequency, we divide the signal power by the spectral bin width. The spectral bin width depends upon the sampling time. We collect 5000 points at a sampling rate of 5×10^6 samples/second. The resulting spectral bin width is $f_s/N = \Delta f$. Noise computations are similar to those discussed in the FD system.

3 Evaluate and tabulate the maximum range allowing UXO/clutter characterization for discrimination for both Time-Domain and Frequency-Domain systems. Generate response curves for different UXO and clutter items at a constant SNR. This includes modifying the acquisition software to calculate the response SNR in real time.

The purpose of this task is to determine the maximum standoff range at which the FD and TD systems can measure the wideband response of various UXO and clutter targets with a reasonable SNR. As discussed in the proposal, an $\text{SNR} = 5$ was agreed upon as a reasonable value at the On-Site Review Meeting held in September 2004. Thus, all maximum standoff ranges for wideband characterization of all UXO and clutter quoted in this task refer to an $\text{SNR} = 5$ for all targets and clutter. The SNR for a wideband response curve was calculated as discussed above. We also note that for the TD system, only the part of the decay curve for which the SNR exceeds 1 is kept as valid data. The late-time data where the signal becomes buried in the noise is not included in the SNR calculation.

3.1 Measurement setup

The data were collected using a wooden test bed. The sensor head was placed on top of the test bed and the target on a sliding platform underneath the sensor. The sliding platform allows smooth variation of the target-sensor distance while keeping the centers of the coil and target aligned along the same vertical. For UXO objects, the direction of measurements is nose toward the northeast axis of the test bed. The clutter items were also marked with an arrow and measurements were performed with the arrow toward the northeast axis of the test bed. All standoff ranges were measured from the target's center of mass to the magnetic sensor location in the center of the transmit coil.

The maximum standoff range was determined in the following manner. Measurements of the wideband response were performed for each target at three different standoffs. For each measurement, the standoff and the SNR were recorded. Then, the SNR versus standoff was plotted and fit to a curve function. The standoff for $\text{SNR} = 5$ was then estimated using the curve fit function. This accuracy of this method was verified using the 81 mm shell.

The results are summarized in Table 5 below for all UXO and selected clutter items. The standoff ranges are reported in centimeters. It is noteworthy that when the active system is operated in a detection mode (narrow frequency mode), it is capable of “seeing” the targets at much greater distances. The UXO and clutter targets used in these measurements are shown in Figure 21, while Figure 8 shows the clutter items used in the characterization standoff study and Figure 23 shows other clutter items for which data were taken.

Target	TD Standoff (cm)	FD Standoff (cm)
20 mm	9.3	11.2
40 mm	18.8	18.4
57 mm	23.4	22.2
60 mm	19.7	21.5
“Gnarly” 60 mm	19.1	20.7
81 mm	29.7	25.1
81 mm nose up	34.1	36.6
81 mm nose down	35.6	39.3
105 mm	31.9	36.1
155 mm	38.7	39.4
CL0093	12.7	11.4
CL0094	15.5	13.6
CL0095	10.6	10.5
CL0096	12.6	12.2
CL0097	7.6	9.3
CL0099	16.7	14.6
CL0100	10.0	10.9
CL0101	14.4	11.5
CL0102	17.1	13.7
CL0103	26.5	20.8
CL0104	23.2	17.3
CL0105	19.0	15.2
CL0106	18.8	14.7

Table 5. Characterization standoff range for TD and FD systems corresponding to a response SNR = 5.



Figure 21. UXO targets used in the measurements of characterization standoff range.



Figure 22. Clutter items used in the measurements of characterization standoff range. A 1" scale bar is shown in the lower left hand corner.



Figure 23. Other clutter items used in the study.

The wideband response curves for all these UXO and clutter items have been measured with both the time-domain (TD) and frequency-domain (FD) systems. The TD instrument is a 2-axis system (in-plane and out-of plane axes) while the FD system is a 3-axis system. With the present FD hardware, however, we still have a cross-axis coupling issue. As a result, we cannot collect data across all three axes simultaneously. We can collect simultaneous data across two axes only and then take data across the third axis separately. This cross-axis coupling can be resolved with further hardware development but, per SERDP instructions, we needed to use the remaining resources to characterize the system rather than do more hardware development.

A summary of the 27 targets used is provided below:

UXO: 20 mm, 40 mm, 57 mm, 60 mm, 81 mm, 105 mm, 155 mm, 155 mm. Although Figure 21 shows one 155 mm shell only, we did have two distinct 155 mm artillery shells.

Clutter: CL0093, CL0094, CL0096, CL0099, CL0100, CL0101, CL0102, CL0103, CL0104, CL0105, CL0106, CL107, CL108, CL109, CL110, CL111, CL112, CL113, CL114.

All measurements were performed across a “T”-shaped grid, as shown in Figure 24. The grid measurements are important because they provide spatial information, and this plays an important role in reducing ambiguity when doing the parameter inversion. The measurement script is as follows:

UXO training data –We measure the response across the grid for UXO targets at orientations of 0, 90, 180 degrees in the Y-Z plane (0 deg representing target alignment along the Z-axis). The targets are at a depth corresponding to an SNR of at least 5. The X- and Y-axes are in the horizontal plane while the Z-axis is out of the plane.

UXO blind data - Measure the response of same UXO targets across the grid with targets at random angle orientation in the Y-Z plane. UXO targets do not have to be at the same depth as in Step 1 but SNR should at least 5.

Clutter blind data - Measure response of clutter pieces at random angle orientation in the Y-Z plane. The targets will be at a depth corresponding to an SNR of at least 5. There is no preferred target orientation in this case.

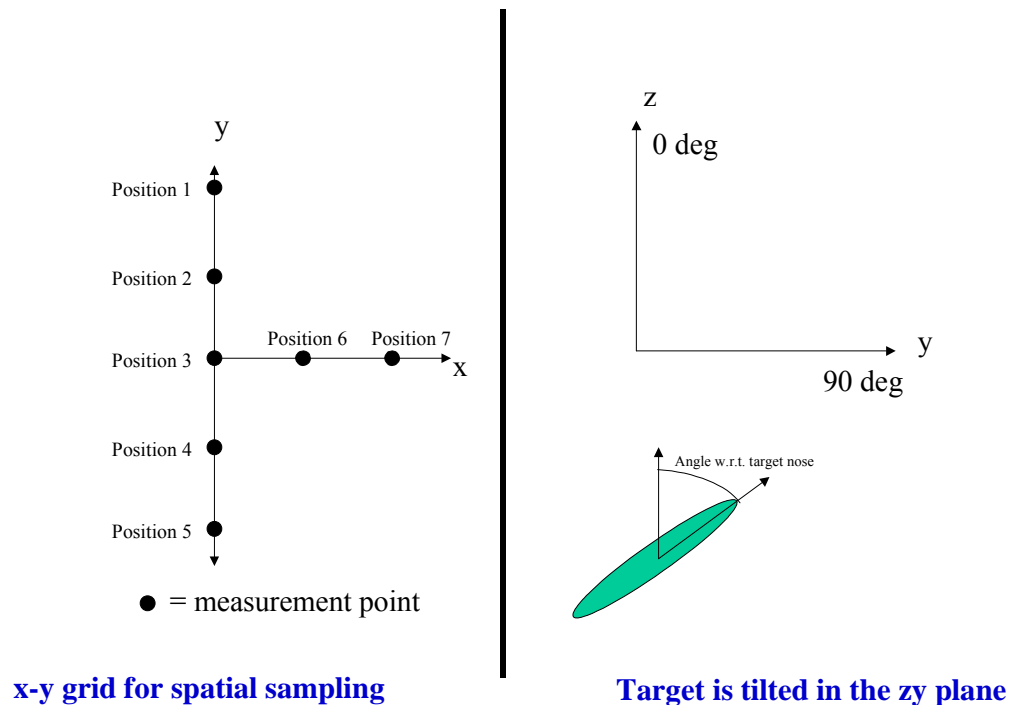


Figure 24. Measurement layout showing the plus-shaped grid and measurement points 1, 2, 3, 4, 5, 6, and 7. Because of the orientation of the target in the y-z plane, there is symmetry with respect to the y-axis and only measurements on one side of the x-axis (i.e., points 6 and 7) need to be recorded.

3.2 Laboratory prototype FD and TD sensors

3.2.1 FD System

The system operates over a bandwidth of 5 Hz – 100 kHz and, in a typical scan, about 15 frequencies are sampled sequentially (i.e., stepped frequency). This stepped frequency mode of operation is not very efficient but it is useful in a laboratory system because it allows one to isolate the signal for each frequency separately and analyze it in a more straightforward manner using a simple diagnostic tool such as an oscilloscope. The system comprises four components briefly described below.

Sensor head

Source coil: [001], 4 turns, diameter = 12"

Bucking coil: 1" diameter

Sensor board: 3-axis MR sensor, electronics

Transmit/Receive electronics

2.5 Ms/sec, 12 bit National Instruments A/D board

5 Ms/sec, 16 bit DAC

Custom low pass filters

VCCS to drive compensation coil

Wideband amplifier

Linear DC supply ($V_{\max} = 48 \text{ V}_{\text{peak}}$; $I_{\max} = 12 \text{ A}_{\text{peak}}$)

Custom power amplifier (bi-polar bridge design)

Inductive load at 100 kHz limits current to 7 A

Computer & software control

Generates waveforms (up to 40 frequencies if needed)

Digitally demodulates signal into in-phase (I) and quadrature (Q) at each frequency

Code for system calibration

Control parameters input through user interface screen

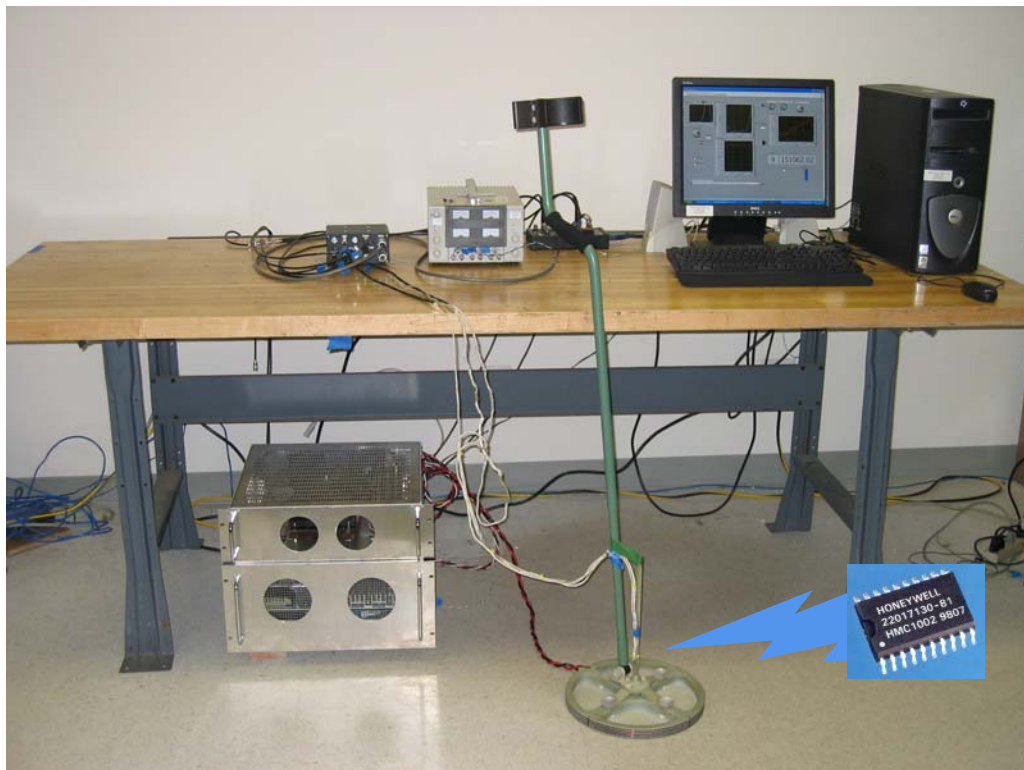


Figure 25. Picture showing FD laboratory system

3.2.2 TD System

In this section, we discuss in detail the characteristics of the wideband TD system. The system operates over a bandwidth of $10 \mu\text{s} - 2800 \mu\text{s}$ and in a typical scan it measures the full decay curve. The system comprises four components briefly described below.

Sensor head

Source coil: [001], 6 turns, 16" diameter

Sensor board: 2-axis MR sensor (Honeywell HMC 1002), electronics

Transmit/receive electronics

Same receive electronics as FD system

Coil driven by 24 V power supply

FET switch is closed to ramp up current in transmit coil to 40 A, left closed for 100 ms, and opened in 100 ns to discharge current

End of current pulse triggers a Set/Reset (3 ms) of sensor, which then triggers data acquisition

Computer

Used for data acquisition and hardware control through a National Instruments multi-function DAQ board

Data input to computer is digitized, displayed in near real time on user interface screen, and stored

All control parameters (acquisition time, number of scans, etc.) are input through this screen.

Representative plots of the testing data taken for the UXO and clutter items listed above can be found in Appendix A at the end of this document.

4 Evaluate and tabulate maximum detection range of UXO targets using passive MR system

Since no work was funded to develop a passive magnetic gradiometer system optimized for this particular application, we used an existing system previously developed for other applications (i.e., not optimized for UXO detection). However, when we tried to revive a mothballed broadband MR magnetic gradiometer previously developed under another contract, we found that the unit was not in a functioning condition. The only other MR system that was available to us was a 3-axis MR magnetometer (not a gradiometer) commercially available from Honeywell (Type HMR2300). Using the Honeywell magnetometer, we measured the magnetic detection range (DR) for a threshold signal corresponding to an SNR = 5. The results are summarized in Table 6.

UXO Type	20 mm	40 mm	57 mm	60 mm	81 mm	105 mm	155 mm
Range @ SNR=5	0.3 m	0.3 m	1.3 m	0.6 m	1.6 m	1.3 m	1.5 m

Table 6. Summary of detection ranges for different types of UXO, as measured using a Honeywell magnetometer.

It is noteworthy that in tests conducted in 2005 and sponsored by NVESD, QM was able to detect 155 mm shells from a 4.6 m standoff using a fluxgate magnetic gradiometer in motion, mounted on a HMMWV. Considering that the noise floor for an MR sensor is about 50 times higher than that of a fluxgate sensor, the corresponding detection range for an MR gradiometer can be inferred by scaling the fluxgate standoff by $50^{1/4}$ since a passive magnetic gradient signal is proportional to the inverse fourth power of the distance. This would correspond to an estimated detection range of 1.7 m for a 155 mm shell using an MR gradiometer. This range inferred indirectly is comparable to the detection range obtained using the commercial, off-the-shelf Honeywell MR magnetometer.

All these values are significantly lower than those obtained in an earlier task using finite-element modeling to simulate the magnetic response of a UXO (e.g., 8 m detection range for a 155 mm). A review of the range estimation shows that it relied on a lower noise floor estimate for the Honeywell MR sensors than we, in fact, achieved. In a separate program, funded by DARPA, we had commissioned Honeywell to design and fabricate a next-generation MR sensor element, which we (and they) had expected to reduce the noise floor by well over an order of magnitude.

The finite-element models were evaluated to provide a range prediction based on the expected lower noise floor. In the event, the prototype sensor elements fabricated by Honeywell, while displaying some improved characteristics relating to sensitivity to off-axis fields, did not improve on the noise floor of their existing commercial models.

5 Process and analyze measurements from Task 2 to address technical issues

5.1 EMI Model

In the ensuing discussion, boldface italic characters represent vectors and un-boldface characters are scalars. Boldface un-italic characters represent tensors.

For sensors sufficiently distant from the target (relative to the target dimensions), the magnetic vector potential may be represented approximately as

$$\mathbf{A}(\mathbf{R}) = \frac{\mu_o}{4\pi} \nabla \frac{1}{R} \times \mathbf{m} = \frac{\mu_o}{4\pi} \frac{\mathbf{m} \times \mathbf{R}}{R^3} \quad (1)$$

where \mathbf{m} is the magnetic dipole moment and \mathbf{R} is the vector from the target center to observation point ($R = |\mathbf{R}|$, $\mathbf{r} = \mathbf{R}/R$). The associated magnetic field is expressed as $\mathbf{H} = \mathbf{r} \frac{1}{2\pi} (\mathbf{m} \cdot \mathbf{r})/R^3$. The dipole approximation in (1) has been applied widely in the context of analyzing magnetometer data for sensing buried UXO, and the accuracy of the magnetic-dipole model fit to measured data is often excellent.

The EMI response of simple targets has been represented in terms of a frequency (time) dependent magnetic dipole, constituting a generalization of the magnetometer model. In particular, the magnetic dipole moment \mathbf{m} of a target is represented as $\mathbf{m} = \mathbf{M} \cdot \mathbf{H}^{\text{inc}}$ where \mathbf{H}^{inc} represents the incident (excitation) magnetic field and \mathbf{M} is a tensor that relates \mathbf{H}^{inc} to \mathbf{m} . For a UXO with axis along the z direction, we may express the magnetization tensor as

$$\mathbf{M}(\omega) = \mathbf{z}\mathbf{z}[m_z(0) + \sum_k \frac{\omega m_{zk}}{\omega - j\omega_{zk}}] + (\mathbf{x}\mathbf{x} + \mathbf{y}\mathbf{y})[m_p(0) + \sum_i \frac{\omega m_{pi}}{\omega - j\omega_{pi}}] \quad (2)$$

where \mathbf{z} is a unit vector in the z direction, and \mathbf{x} and \mathbf{y} correspond to orthogonal unit vectors, each perpendicular to \mathbf{z} . The terms $m_z(0)$ and $m_p(0)$ account for the induced magnetization produced for ferrous targets (valid down to static magnetic-field excitation, $\omega \rightarrow 0$), and the terms in the summations account for the frequency-dependent character. It is important to note that an EMI sensor operated down to zero (or very low) frequency is distinct from a magnetometer, since the excitation magnetic fields are different in these two cases: for a magnetometer the target is excited by the earth's magnetic field, while for the very-low-frequency EMI sensor the excitation fields are generally generated by a loop source. Note in (2) the poles at imaginary frequencies $j\omega_{zk}$ and $j\omega_{pi}$, these corresponding to the magnetic singularities that generalize the SEM method to EMI frequencies. For simple targets, typically we only require the first term in each sum, representative of the principal dipole mode along each of the principal axes.

Given the excitation magnetic fields \mathbf{H}^{inc} , from which we obtain \mathbf{m} using (2), the associated magnetic vector potential is computed using (1). If we assume that the EMI source responsible for \mathbf{H}^{inc} can be represented, as seen from the target, as a magnetic dipole with moment \mathbf{m}_s , then

$\mathbf{H}^{inc} = \hat{\mathbf{r}}_{st} \frac{1}{2\pi} \frac{\mathbf{m}_s \cdot \hat{\mathbf{r}}_{st}}{R^3}$, where $\hat{\mathbf{r}}_{st}$ is a unit vector directed from the source to the target center, with this distance represented by R ($|\mathbf{r}_{st}| = R$). If we assume that the source and observer coils are co-located (or nearly co-located), then the total magnetic field observed at the sensor, \mathbf{H}^{rec} , is represented by

$$\mathbf{H}^{rec}(\omega) \propto \frac{\hat{\mathbf{r}}_{st}}{R^6} \cdot \mathbf{U}^T \cdot \mathbf{M} \cdot \mathbf{U} \cdot \hat{\mathbf{r}}_{st} \quad (3)$$

where the proportionality constant depends on the strength of the dipole source \mathbf{m}_s and the characteristics of the receiver. The 3×3 unitary matrix \mathbf{U} rotates the fields from the coordinate system of the sensor to the coordinate system of the target (the $\mathbf{x}, \mathbf{y}, \mathbf{z}$ coordinate system in (3) is defined by the orientation of the target), and \mathbf{U}^T , which is the transpose of \mathbf{U} , transforms the dipole fields of the target (in the \mathbf{M} coordinate system) back to the coordinate system of the sensor. Clearly the matrix \mathbf{U} contains information about the target orientation (the angles of the target θ and ϕ with respect to the sensor coordinate system).

For the time-domain data, the above frequency-domain analysis is converted analytically into the time domain, and the feature extraction is performed directly in the time domain.

5.2 Feature Extraction

The EMI models are far more sophisticated than the magnetometer model, reflecting the enhanced information content in the EMI data (*vis-à-vis* the magnetometer), but also leading to difficulties with local minima when performing parameter extraction from measured data. With regard to the other parameters in the EMI model, the search range is constrained based on previous experience with previously observed data. For example the EMI resonant frequencies $\omega_{zk}^n / 2\pi$ and $\omega_{pi}^n / 2\pi$ typically range from a couple hundred to several thousand Hertz, and such a range is considered in the parameter inversion.

Within the context of (2) and (3), we here assume that only one term is required in each sum. The parameters to be determined are the approximate target center (constrained via the magnetometer inversion), the target orientation (characterized by the unitary matrix \mathbf{U}), $m_z(0)/m_p(0)$ (for ferrous targets), m_z/m_{p1} , and ω_{z1} and ω_{p1} . These parameters are determined via a multi-dimensional gradient search. To circumvent problems associated with local-optimal solutions, we consider numerous solutions for the model parameters, based on random initializations of the parameters in (2). We typically find that most of the initializations lead to the same minima, while there are also several additional but less frequently visited “stray” minima. The final parameters are taken as those that correspond to the minimum mean-square error between the measured and model data.

5.3 Classifier Model Design

We designed a Gaussian Mixture Model (GMM) to characterize the statistical representation of the UXO features. In the testing phase, we may use this GMM to quantify the likelihood that the data under test is similar to the UXO training data. If the likelihood of a testing item is high it is deemed to be UXO-like, and otherwise it is defined to be clutter (because it has a low likelihood of being like the UXO items seen when training). The GMM representation used here is semi-

parametric, which implies that the model is based on a Gaussian structure, but the number of mixture components is unknown *a priori* and is inferred from the training data. Below, we provide details on this model.

Let \mathbf{v} represent a feature vector extracted from the EMI model, as discussed above. A Gaussian mixture model is represented as

$$p(\mathbf{v}|K, \mathbf{w}, \boldsymbol{\Theta}) = \sum_{k=1}^K w_k p(\mathbf{v}|\boldsymbol{\Theta}_k) \quad (4)$$

where $p(\mathbf{v}|\boldsymbol{\Theta}_k)$ is a Gaussian distribution with mean and covariance defined by the associated vector $\boldsymbol{\Theta}_k$, and w_k represents the probability that the k^{th} mixture component is used, with $\sum_{k=1}^K w_k = 1$. If we have N training vectors $\mathbf{D} = \{\mathbf{v}_n\}_{n=1, N}$, then Bayesian theory may be employed to constitute a posterior estimate on the model parameters \mathbf{w} and $\boldsymbol{\Theta}$, specifically

$$p(\mathbf{w}, \boldsymbol{\Theta}|\mathbf{D}, K) = \frac{\prod_{n=1}^N \left\{ \sum_{k=1}^K w_k p(\mathbf{v}_n|\boldsymbol{\Theta}_k) \right\} p(\mathbf{w}) p(\boldsymbol{\Theta})}{p(\mathbf{D}|K)} \quad (5)$$

where the denominator in (5) is computed in principle by “integrating out” the parameters \mathbf{w} and $\boldsymbol{\Theta}$ in the numerator. This process is difficult to achieve without approximation, and here we utilize the variational Bayes algorithm.

Our objective is to obtain the posterior probability distribution of the hidden variables $\boldsymbol{\theta}$ based on a set of observed variables $\mathbf{D} = \{\mathbf{v}_n\}_{n=1, N}$. Here $\boldsymbol{\theta}$ are defined by \mathbf{w} and $\boldsymbol{\Theta}$, *i.e.*, $\boldsymbol{\theta} = \{\mathbf{w}, \boldsymbol{\Theta}\}$. Since an exact inference of the hidden variables $\boldsymbol{\theta}$ based on the observed variables \mathbf{D} is intractable for all but the simplest model structures, our goal is to find a tractable variational distribution $Q(\boldsymbol{\theta})$ that closely approximates the true posterior distribution $p(\boldsymbol{\theta}|\mathbf{D})$.

Let $p(\mathbf{D})$ denote the marginal probability of the observed data \mathbf{D} . The log-marginal can be written as

$$\ln p(\mathbf{D}) = L(Q) + KL(Q\|P') \quad (6)$$

where

$$L(Q) = \sum_{\boldsymbol{\theta}} Q(\boldsymbol{\theta}) \ln \frac{p(\mathbf{D}|\boldsymbol{\theta}) p(\boldsymbol{\theta})}{Q(\boldsymbol{\theta})} \quad (7)$$

and

$$KL(Q\|P') = \sum_{\boldsymbol{\theta}} Q(\boldsymbol{\theta}) \ln \frac{p(\boldsymbol{\theta}|\mathbf{D})}{Q(\boldsymbol{\theta})} \quad (8)$$

with $P' = p(\boldsymbol{\theta}|\mathbf{D})$. The summations in (7) and (8) are replaced by integrals if the hidden variables $\boldsymbol{\theta}$ are continuous.

Note that the above expression is true for any approximating variational distribution $Q(\boldsymbol{\theta})$. The term $KL(Q\|P')$ represents the Kullback-Leibler (KL) divergence between the true posterior $p(\boldsymbol{\theta}|\mathbf{D})$ and its variational approximation $Q(\boldsymbol{\theta})$. Our objective is to optimize $Q(\boldsymbol{\theta})$ to minimize the KL divergence between $Q(\boldsymbol{\theta})$ and $p(\boldsymbol{\theta}|\mathbf{D})$. However, since the posterior density function $p(\boldsymbol{\theta}|\mathbf{D})$ is known, and is the subject of this analysis, the KL divergence in (8) cannot be evaluated. However, since $KL(Q\|P')$ is always non-negative, the term $L(Q)$ forms a lower bound of the log-marginal, $\ln p(\boldsymbol{\theta})$. Consequently, minimization of $KL(Q\|P')$ with respect to Q is equivalent to maximization of $L(Q)$ since the left hand side $\ln p(\mathbf{D})$ is independent of the variational distribution Q . All of the terms in (6) can be evaluated, and therefore the Variational Bayes (VB) approximation to $p(\boldsymbol{\theta}|\mathbf{D})$ reduces to attempting to determine the $Q(\boldsymbol{\theta})$ that maximizes the variational expression $L(Q)$.

For the sake of tractability, we assume that the hidden variables are independent of each other, meaning $Q(\boldsymbol{\theta})$ may be written in a factorized form as $Q(\boldsymbol{\theta}) = \prod_i Q_i(\theta_i)$, where $\{\theta_i\}$ is the set of disjoint hidden variables indexed by i constituting $\boldsymbol{\theta}$. In variational inference, we optimize the factors of the variational distribution one at a time, cycling sequentially through all factors. We accomplish this by separating out the terms involving a factor $Q_i(\theta_i)$ (approximating the distribution for hidden variable θ_i). We can therefore maximize the lower bound $L(Q)$ with respect to a single factor Q_i (assuming all $Q_{j,j \neq i}$ are temporarily fixed), and then cycling through each hidden variable θ_i in turn replacing the current distribution $Q_i(\theta_i)$ with a revised estimate $Q_i^*(\theta_i)$.

This iterative VB analysis can be performed efficiently if each $Q_i(\theta_i)$ is conjugate to the likelihood function with all $\theta_{j,j \neq i}$ equal to a constant. Specifically, this conjugacy property allows the update equations to be performed analytically, thereby yielding a VB algorithm with computational speed commensurate with the widely used EM algorithm employed in ML point estimates of the parameters $\boldsymbol{\theta}$.

5.4 Evaluation of testing data

As a product of the training process, we have the model

$$p(\mathbf{v}|\mathbf{K}, \mathbf{w}, \boldsymbol{\theta}) = \sum_{k=1}^K w_k p(\mathbf{v}|\boldsymbol{\theta}_k) \quad (9)$$

where in principle we may integrate out the parameters \mathbf{w} and $\boldsymbol{\theta}$, since from the VB analysis above we have a full posterior density function on these parameters, based on the training data \mathbf{D} . Any feature vector \mathbf{v} under test may be submitted to (9), yielding the likelihood that the item under test looks like items seen while training. The larger this quantity, the more likely it is that the item under test was seen while training. In addition, we may quantify the likelihood that the testing item is associated with any particular mixture component in (9). By understanding the training items associated with a given mixture component, one may also infer which training item(s), the testing item looks most like, providing an opportunity for classification.

5.5 Presentation of results

The GMM developed for characterization of the EMI-based features \mathbf{v} defines the density function $p(\mathbf{v}|K, \mathbf{w}, \boldsymbol{\theta}) = \sum_{k=1}^K w_k p(\mathbf{v}|\boldsymbol{\theta}_k)$, where this is designed based on the training data. For a given testing vector \mathbf{v}_t , from the testing targets, the likelihood that the vector \mathbf{v}_t is associated with (similar to) the training data is computed via the likelihood

$$\text{Likelihood of being UXO} = p(\mathbf{v}_t|K, \mathbf{w}, \boldsymbol{\theta}) = \sum_{k=1}^K w_k p(\mathbf{v}_t|\boldsymbol{\theta}_k) \quad (10)$$

with this used to rank the item likelihood of being a UXO. We may also compute the likelihood that the item under test is associated with any of the mixture components, this defined by $p(\mathbf{v}_t|\boldsymbol{\theta}_k)$. By understanding which training UXOs are most likely for a given mixture component, one may infer which UXO type the item under test looks most like.

Assume that the item under test has been detected as being a UXO, and one wishes to determine the mixture component with which it is most probably associated. Again, by mapping the item under test to a given mixture component, and by understanding which training UXO are associated with a given mixture component, one may infer which UXO type the item under test looks most like. The probability that testing feature vector \mathbf{v}_t is associated with mixture component k is expressed as

$$p(k|\mathbf{v}_t, K, \mathbf{w}, \boldsymbol{\theta}) = \frac{w_k p(\mathbf{v}_t|\boldsymbol{\theta}_k)}{\sum_{k=1}^K w_k p(\mathbf{v}_t|\boldsymbol{\theta}_k)} \quad (11)$$

5.6 Results

5.6.1 Frequency-domain data

The VB GMM analysis uses 5 mixture components, of which there are two dominant mixture components, and three insignificant ones. Specifically, the results indicate that most of the feature vectors for the training data are associated with the same dominant mixture component (component 3) while the rest (corresponding to the 57 mm shell) are associated with mixture component 4, as seen in Figure 26. Mixture components 1, 2 and 5 have insignificant contributions.

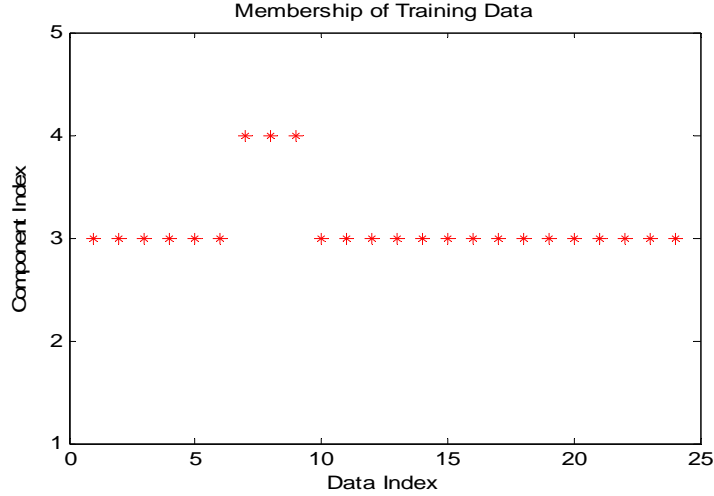


Figure 26. Distribution of mixture components for feature vectors associated with the FD training data. The data index identifies the UXO item used in training, each item measured in each of the three cardinal orientations. Eight training items thus yield twenty-four indices.

We also summarize the results for the training data in Table 7, where we show the log likelihood that the data are associated with the entire UXO mixture model, as well as the likelihood of being associated with the third and fourth mixture components separately. Likelihoods are tabulated for each cardinal orientation of each UXO item, giving three rows of likelihoods per item.

These results are not consistent in the sense that the parameters extracted from the model are not consistent as a function of target orientation. Different orientations of the same target yielded different parameters for the target model. This made it very hard to do any classification. Moreover, the algorithms used by Duke worked well when only the z -field component is used presumably because the other components (i.e., x and y) had weak energy and were often noisy. For these reasons, the classification results that will be discussed herein involve the analysis of the vertical z -fields only.

UXO Index	Log-likelihood from UXO Mixture	Log-likelihood from 3rd Gaussian	Log-likelihood from 4th Gaussian
20 mm	9.8262	12.9526	0.000181
	6.132	8.0829	0.000238
	7.6416	10.0729	0.000169
40 mm	4.4677	5.8891	0.000168
	2.6409	3.481	0.00021
	0.1032	0.13587	0.000544
57 mm	0.005247	1.81E-13	0.038016
	0.007633	9.88E-16	0.055305
	0.007185	8.30E-13	0.051987
60 mm	5.0982	6.7203	0.000123
	5.129	6.7609	0.000125
	5.8127	7.6621	0.000126
81 mm	0.56959	0.75071	0.000197
	6.5351	8.6143	0.000179
	3.7782	4.9802	0.000135
105 mm	8.1113	10.6921	0.000179
	5.7769	7.6149	0.000206
	5.5483	7.3136	0.000296
155 mm	5.7069	7.5226	0.000171
	7.0992	9.3579	0.000151
	6.8867	9.0779	0.000166
155 mm	8.5944	11.3289	0.000184
	8.0995	10.6766	0.000166
	3.9959	5.2672	0.000217

Table 7. Analysis of FD training data showing the log-likelihood that each training-UXO data set was generated from the UXO GMM (first result column) and from the third and fourth Gaussian mixtures (second and third columns, respectively). Three rows per item represent the log-likelihoods measured in each of the three cardinal orientations of the training item.

The results of the likelihood that the testing data are similar to the UXO training data are shown in Table 8, which ranks all the targets (including clutter items). The table also shows the likelihood that the item under testing is associated with any of the individual 3rd and 4th mixture components. When the target indexes are compared with the target truth table, we obtain the classification results shown in Figure 27.

Target Index	Log-likelihood from UXO mixture	Log-likelihood from 3rd Gaussian	Log-likelihood from 4th Gaussian
9	9.5574	12.5983	0.000201
2	9.0959	11.9899	0.000174
23	8.436	11.1201	0.000183
1	7.4288	9.7923	0.000224
20	6.8672	9.0521	0.000191
13	6.692	8.8212	0.000167
22	6.4421	8.4917	0.000174
5	5.7955	7.6395	0.00019
15	5.3998	7.1178	0.000214
18	4.2668	5.6242	0.000181
19	3.7989	5.0075	0.000186
14	3.0078	3.9648	0.000246
3	1.4068	1.8543	0.000428
11	0.8303	1.0944	0.000117
12	0.54347	0.71628	0.000108
4	0.31973	0.42136	0.000163
26	0.075744	0.099704	0.00031
27	0.007461	7.82E-12	0.053987
17	0.001716	0.002041	0.000821
6	0.000912	0.000866	0.001496
21	0.000226	0.000237	8.63E-05
24	0.000187	0.00018	4.09E-05
25	2.27E-05	9.44E-14	2.07E-05
7	1.16E-05	8.99E-12	4.98E-05
10	1.04E-05	1.68E-12	1.45E-06
8	7.19E-07	2.64E-19	2.49E-06
16	3.44E-08	2.01E-26	3.62E-10

Table 8. Analysis of FD testing data showing log-likelihood that each testing target measurement was generated from the UXO GMM (first result column) or generated from the third and fourth Gaussian mixture (second and third columns, respectively). Test objects were only measured in one, random orientation, so there is only one row of likelihood estimates per item.

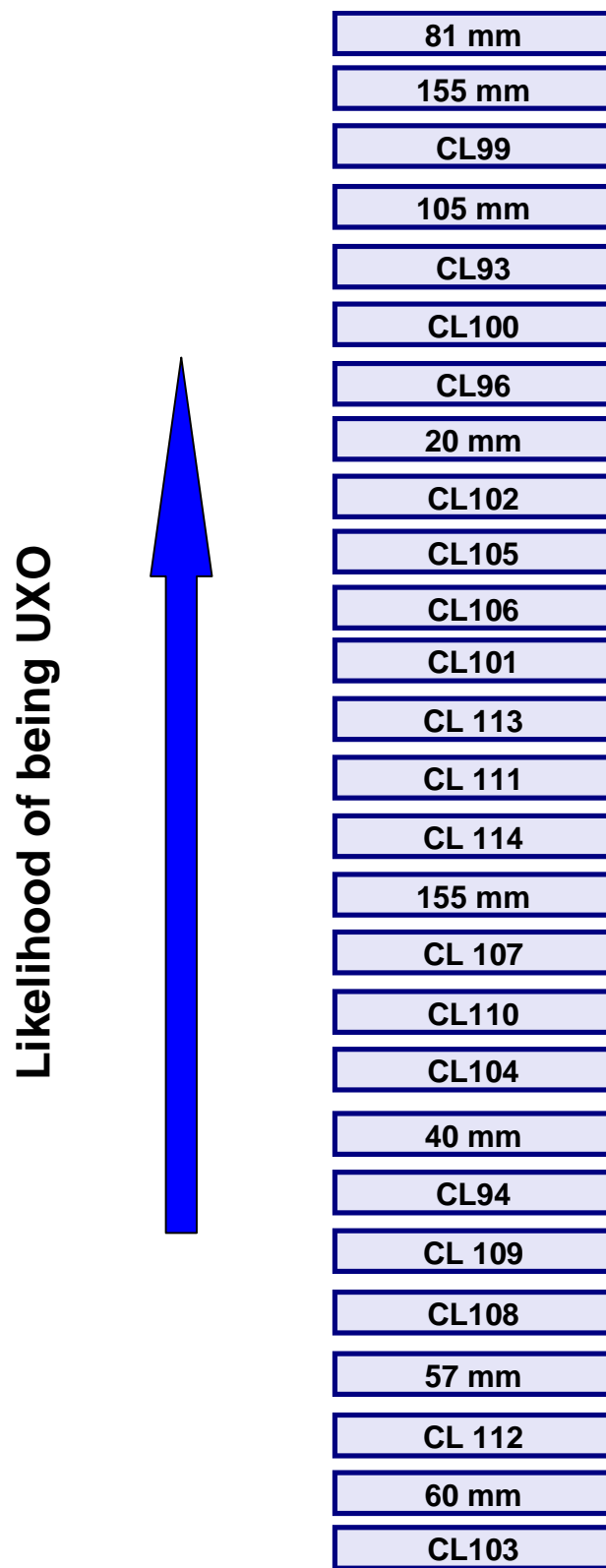


Figure 27. Ranking of targets from least likely to most likely of being a UXO using FD data.

5.6.2 Time-domain data

The VB GMM analysis of the training data with 5 mixture components yields four significant mixture components (components 1, 3, 4, 5) and one insignificant one (component 2), as seen in Figure 28 which displays the component index versus the data index. Most of the items are associated with the same (most dominant) mixture component. Most of the feature vectors are associated with the same mixture component (component 4), and the rest are associated with mixture components 1, 3, and 5. Mixture component 2 has an insignificant contribution.

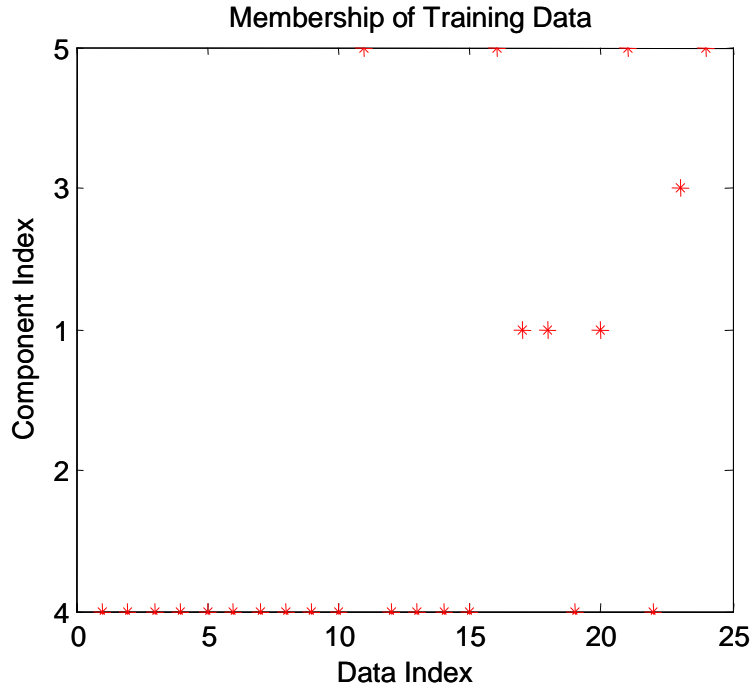


Figure 28. Distribution of mixture component for feature vectors associated with TD training data. Data index again corresponds to measurements of eight UXO items, each in three cardinal orientations.

The results for the training data are summarized in Table 9, where the log likelihood that the data are associated with the entire UXO mixture model is shown, as well as the likelihood of being associated with the first, third, fourth, and fifth mixture components separately. As with Table 7, so here each UXO item is associated with three sets of likelihoods, corresponding to measurements in three cardinal orientations.

The results of the likelihood that the testing data are similar to the UXO training data are shown in Table 10, which ranks all the targets (including clutter items). The table also shows the likelihood that the item under testing is associated with any of the individual 1st, 3rd, 4th, and 5th mixture components. When the target indexes are compared with the target truth table, we obtain the classification results shown in Figure 29.

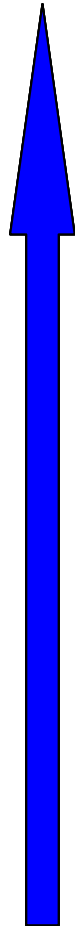
UXO Index	Log-lik from UXO mixture	Log-lik from 1st Gaussian	Log-lik from 3rd Gaussian	Log-lik from 4th Gaussian	Log-lik from 5th Gaussian
20 mm	0.58656	0.003673		1.0015	0.008556
	0.60435	0.003761	0.001859	1.0318	0.009133
	0.57369	0.003598	0.001806	0.97949	0.008293
40 mm	0.6374	0.004738	0.002269	1.0856	0.017447
	0.63139	0.006252	0.002358	1.0739	0.021072
	0.3602	0.006257	0.003	0.60241	0.042755
57 mm	0.58224	0.003717	0.001797	0.99415	0.00823
	0.57643	0.003655	0.001795	0.98423	0.00817
	0.57858		0.001797	0.9879	0.008203
60 mm	0.19157	0.009751	0.003505	0.3022	0.076898
	0.06686	0.006144	0.011499	0.000503	0.36912
	0.56239	0.00496	0.001862	0.95938	0.009696
81mm	0.66977	0.004302	0.00201	1.1429	0.011903
	0.63771	0.003	0.001954	1.0884	0.010728
	0.62637	0.003	0.001903	1.0693	0.009873
105 mm	0.062	0.006344	0.008645	0.002353	0.33974
	0.022996	0.1653	0.000833	5.69E-09	0.00033
	0.016908	0.12153	0.000691	3.47E-10	0.000158
155 mm	0.18715	0.007465	0.003623	0.29499	0.077421
	0.014865	0.089913	0.002659	1.95E-05	0.012131
	0.0729	0.010096	0.009264	0.00089	0.40001
155 mm	0.1382	0.008204	0.001811	0.23168	0.009071
	0.007845	0.00021	0.1102	1.45E-09	0.000774
	0.062632		0.008524	0.00073	0.3404

Table 9. Analysis of TD training data showing log-likelihood that each training-UXO data set was generated from the UXO GMM and generated from each significant mixture (left to right). Each training item was measured in three cardinal orientations, yielding three rows of likelihoods per item.

Target Index	Log-lik from UXO mixture	Log-lik from 1st Gaussian	Log-lik from 3rd Gaussian	Log-lik from 4th Gaussian	Log-lik from 5th Gaussian
15	0.68842	0.005239	0.002213	1.1732	0.01669
21	0.67879	0.00528	0.002262	1.1563	0.01786
19	0.65942	0.004231	0.001942	1.1256	0.010706
3	0.65808	0.004332	0.002094	1.1224	0.013439
13	0.64597	0.004925	0.002295	1.1	0.018245
5	0.63872	0.003995	0.001954	1.0901	0.01074
11	0.6226	0.003948	0.001863	1.0629	0.0093
12	0.60958	0.005217	0.002416	1.0366	0.021586
10	0.60041	0.003974	0.001813	1.0251	0.008585
14	0.59388	0.003742	0.001823	1.014	0.008603
26	0.58957	0.003867	0.001797	1.0067	0.008313
22	0.58445	0.003741	0.001798	0.99793	0.008261
20	0.57961	0.003623	0.001818	0.9896	0.008472
16	0.57135	0.006433	0.002149	0.97252	0.01583
23	0.47588	0.005653	0.002706	0.80451	0.03074
7	0.46482	0.005427	0.001837	0.79212	0.009393
24	0.22769	0.006733	0.003405	0.36919	0.062476
27	0.18945	0.007595	0.003618	0.29882	0.077722
6	0.081317	0.011143	0.004423	0.090756	0.15013
17	0.072237	0.008682	0.007738	0.004439	0.38609
18	0.069196	0.010037	0.004928	0.058026	0.19056
8	0.067214	0.007328	0.007999	0.003859	0.36035
4	0.061496	0.006963	0.007563	0.005145	0.32394
9	0.022427	0.012986	0.001764	0.032445	0.00794
25	0.013184	0.013646	0.001675	0.01687	0.006573
1	0.006246	0.038095	0.001508	0.000134	0.003666
2	0.00213	4.10E-05	0.02993	1.01E-11	5.78E-05

Table 10. Analysis of TD testing data showing log-likelihood that each testing target data set was generated from the UXO GMM, or from each Gaussian mixture component (right to left). Each test target was measured in only a single, random orientation.

Likelihood of being UXO



CL102
CL94
CL106
CL113
CL100
20 mm
CL111
CL114
CL112
CL101
CL107
CL96
CL 93
CL103
CL99
57 mm
CL109
CL110
40 mm
CL104
CL105
60 mm
155 mm
81 mm
CL108
105mm
155 mm

Figure 29. Ranking of targets from least likely to most likely of being a UXO using TD data.

5.6.3 Discussion

Based on the likelihood factor as a ranking factor, the results shown in Figure 27 and Figure 29 indicate that the classification algorithms worked poorly both for the time-domain and the frequency-domain data. For the sake of discussion, let us define a tentative threshold that roughly divides the likelihood scale in Figures 12 and 14 in two halves, where the upper and lower halves correspond to most likely and less likely to be a UXO, respectively. For the FD data, only four out of the eight UXO items place in the upper half of the likelihood scale. The difficulty arises mostly from discriminating UXO from small clutter items such as CL099, CL093, CL100, CL96, and CL102. For the TD data, the results are not any better with most of the UXO item placing in the lower half of the likelihood scale (i.e., classified as not likely to be UXO).¹ To put these results in perspective, it is useful to recall that these results have been obtained using only one field component, namely the vertical z component. The algorithm used in this analysis did not work well for the x and y components and as such these components were not utilized. What these results may be confirming is that it is not possible to do an adequate classification with only one field component, especially with the variety of clutter and sizes used in the study.

The extended sensor bandwidth afforded by the FD and TD sensors did not seem to help, which suggests that the signal does not carry significant information at high frequencies/early times. This is not totally unexpected considering that UXO items are large bodies and as such much of the signal variation occurs at low frequencies/late times. However, we cannot provide a definitive answer on the usefulness of the extended bandwidth based on the present analysis. To do so requires doing an appropriate analysis first and then studying how the results change as the bandwidth is adjusted.

It is also noteworthy that the classification algorithm used in the analysis relies on a dipole model, which assumes that the distance between the target and sensor is several times the size of the target. In this work, however, the sensor-target distance is at best 1.5 times the length of the target (for small UXO items) due to SNR considerations and in this regime the EMI model used is not appropriate. One indicator is that the parameters extracted from the model are not consistent as a function of target orientation, in that different orientations of the same target yielded different (often very different) parameters for the target model.

The likelihood of being associated with a particular mixture component tracks very closely the likelihood from the UXO mixture. Thus, an attempt to do classification of testing data based on the mixture components would yield the same results.

6 Conclusions

The objective of this work was to examine in the laboratory the potential of wideband EMI, multiple field component measurements, and combined frequency-time domain measurements in improving UXO/clutter discrimination. The approach was to build research instruments

¹ The main text represents the conclusions of the co-author in charge of the classification effort (L. Carin). However, the reader should note that the TD classifier performance seems significantly improved simply by inverting the sign of the output: fully 7 out of the 8 UXO appear in the bottom half of the scale, so inverting the scale provides a probability of detection of 87.5%. Whether this is a meaningful result, is debatable. However, it is very unlikely to occur by chance.

(frequency-domain and time-domain) using magnetoresistive (MR) sensors, use them to collect in-air data (as a function of frequency, position, orientation, and depth) in the laboratory on selected canonical targets (both UXO and clutter) and then process the data using modeling tools and algorithms. The data processing was performed entirely by Professor Carin's group using tools and algorithms developed at Duke University.

To that end, we built and tested two wideband, multi-axis laboratory systems: a FD operating over the frequency range 5 Hz – 100 kHz and a TD system with the capability of measuring the full decay curve over the time window 10 μ s – 2800 μ s. During the course of this program, significant effort was required to design and build these prototype systems, which incorporate several technological “firsts”: the first truly wideband system (at both high *and low* frequencies), the first multi-component receiver, and the first to incorporate compact, solid-state magnetoresistive (MR) sensors. The development of such a system did not simply amount to an assembly of off-the-shelf components but entailed an R&D effort.

Using these systems, we collected FD and TD data on a set of canonical UXO targets and clutter items at various orientations and standoffs. Signature data were collected by moving the sensor over an x - y grid for spatial sampling. Two types of measurements were made for each target: a training data set and a “blind” data set. For the training data, target ID, standoff depth and orientations (0°, 90°, 180°) were made known to Duke for training their algorithms, while the blind data collected at random angles was provided without any target, orientation or standoff information.

The goal of this study was to address the following main issues pertaining to the UXO problem:

1. Define critical parameters for active sensor using research tool. Parameters include number of axes needed in the receiver, optimal bandwidth, and FD versus TD performance.
2. Can an active sensor have sufficient SNR to achieve discrimination?

An initial study, performed with a small number of targets and clutter, yielded the following qualitative results. The average data correlation decreases as bandwidth increases, indicating enhanced classification ability with increasing bandwidth up to 100 kHz. The result, however, was based on a small dataset and may not be true for a larger body of data. Furthermore, the analysis used only UXO data and did not include clutter data. Thus, the bandwidth analysis needed to be performed using signature data from both UXO and clutter. Simulated and experimental data suggested that discrimination with z -data only was not likely to be useful, but that utility improved with the addition of x - and y -data. A comparison of the FD and TD results, however, was also inconclusive due to the limited amount of data. After a SERDP Program Office review, it was concluded that the results could only be validated with a larger set of targets and realistic clutter objects, especially small size fragments. Another recommendation was to insure that the SNR of the response signals be the same across all the UXO targets and be equal to at least 5. It would be useful at this point to point out that the standoff range we refer to is the standoff range for characterization, not detection. Active detection is usually performed at a single frequency whereas the AC response for characterization is performed across a wide frequency band and, as such, the coil impedance at the highest frequencies limits characterization range.

Following the recommendations of the Program Office, we then focused on characterization of the sensor capabilities using a more extended set of clutter items, as shown in Figures 8 and 9. Even though the standoffs were not significantly different from the initial study, the data processed by Duke University yielded classification results that are poorer than in the initial study, even when utilizing the z -field component only. From that point of view, we feel that even though some data exhibit noise for particular orientations/grid positions, there is still significant information in the x - and y -responses for many targets; the Duke study elided all this data, regardless of the particular signal to noise ratio. The effect of bandwidth and the comparison of FD and TD instruments were not done because the classification analysis did not yield decent results.

These results could be partly or wholly due to the following:

1. The models used by Duke do not work well since they do not apply when the distance between the sensor and the target is smaller than several times the largest target dimension (i.e., the target is not in the dipole limit). To overcome this difficulty, one must utilize more general models that do not make any assumptions on the sensor-target distance.
2. The particular mix of UXO and clutter items used in this study contained many fragments and small clutter items. This could present a challenge in the discrimination process, especially when using only one field component (the z -component). The initial study that yielded better results included only relatively larger clutter items. However, the extended high-frequency system bandwidth ought to have been more useful, since the smaller an object, the higher the frequency of its response variation. Furthermore, the constraint of performing all measurements at the same (high) SNR value removes another useful piece of discriminatory information: the overall signal *amplitude*, which in the high-frequency limit is proportional to the solid angle subtended by the target in the excitation field. Since small targets were measured nearer the system in order to maintain SNR, the total signal amplitude variation was much smaller than it would have been, had all targets been measured instead at the same distance (for example).
3. In this work, the excitation field is applied along one direction only (i.e., the vertical direction) while the response signals were measured along all three axes. It is then not surprising that the z -axis signal is strong and the x - and y -axes are weak. To remedy this problem, we need to use a multi-axis transmit coil. The requirement for impractically large size and power made us drop our initial attempt to develop such a multi-axis coil. We are aware that other SERDP projects have been working on developing a fieldable 3D coil but are not aware of any existing hardware available for immediate use.

Note that the TD results may be more usable than the FD. While the FD classification results are to all intents and purposes identical to a coin toss, the TD results, when inverted, yield a probability of detection (correct identification of UXO) of 85.7% and a probability of false alarm (incorrectly classifying clutter as UXO) of 35.3%. Why this should be so is unknown, and we do not unequivocally claim significance for the result—let alone claim an understanding of its origin. However, we point out that if the data are truly uncorrelated across item classes, then the performance, statistically, converges to that of a coin toss (as the FD results appear to have

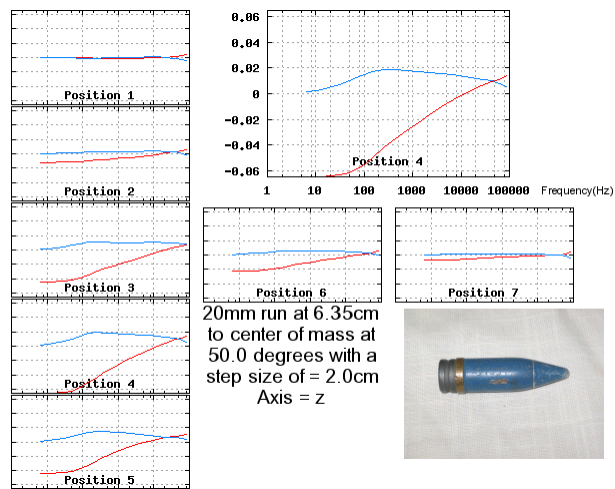
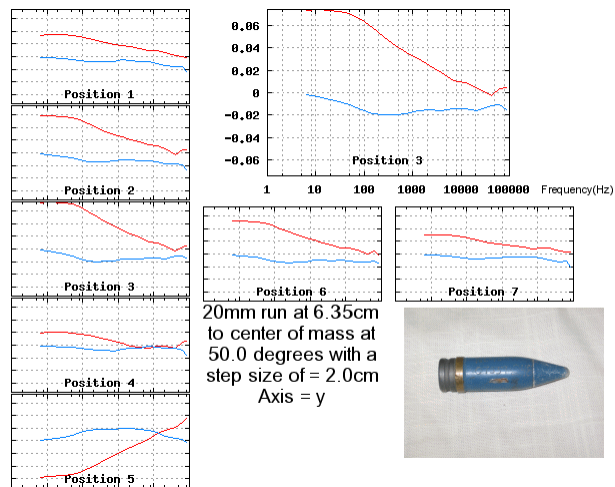
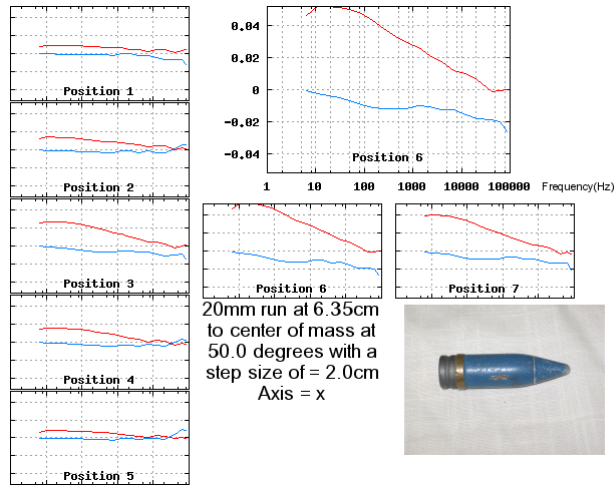
done). In that case, it is statistically extremely unlikely for the results to deviate as strongly from a coin toss as the TD results did. Such an unlikely result—seemingly significantly worse than a coin toss—probably arises from a systematic effect: either an unaccounted systematic error (such as a change in system operation or procedure between taking the training set and the test set) or an error in the processing of the test results (a simple, unnoticed inversion of the result). Quantum Magnetics observed no change in system performance during acquisition of the TD training and test data sets, and Duke University observed no “sign error” in its processing. Thus, the conclusion must remain, to our frustration, ambiguous.

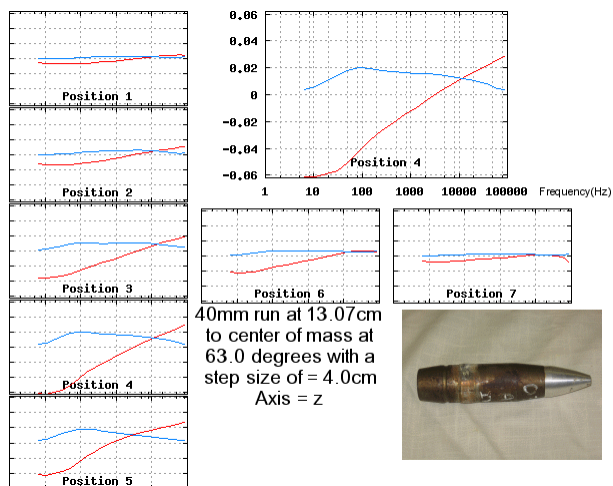
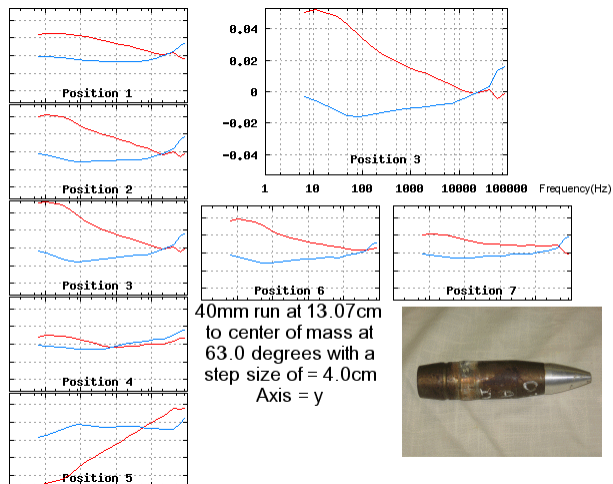
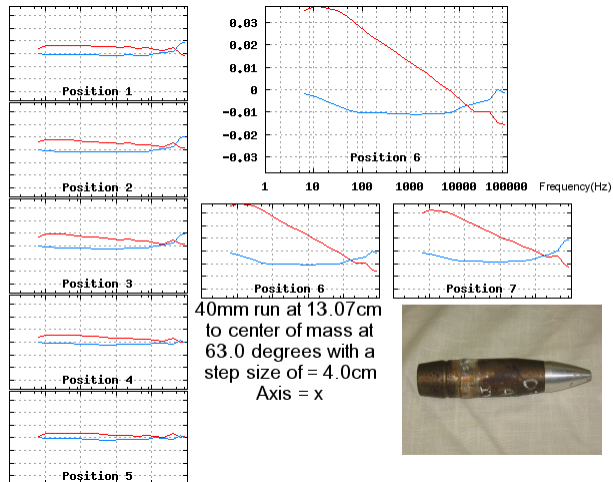
Quantum Magnetics, in a separate, internally funded project to develop an improved concealed weapon detection portal, developed its own classification algorithms. A preliminary look at applying these algorithms to the FD data suggest that they may provide usable detection and classification performance, comparable to the inversion of the Duke TD algorithm outputs. Quantum Magnetics plans, using internal funds, to carry out a more detailed investigation of this prospect in the future.

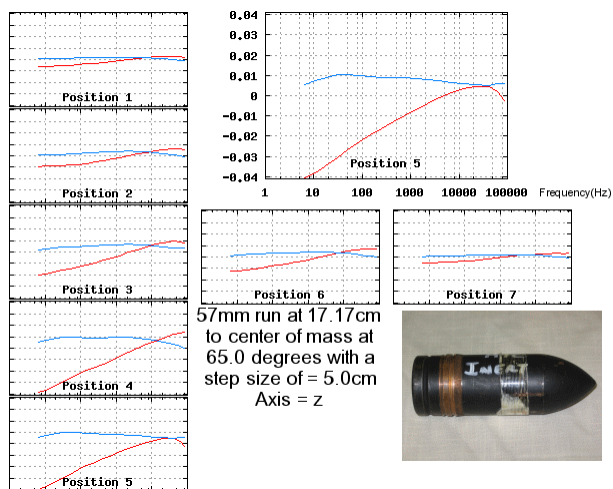
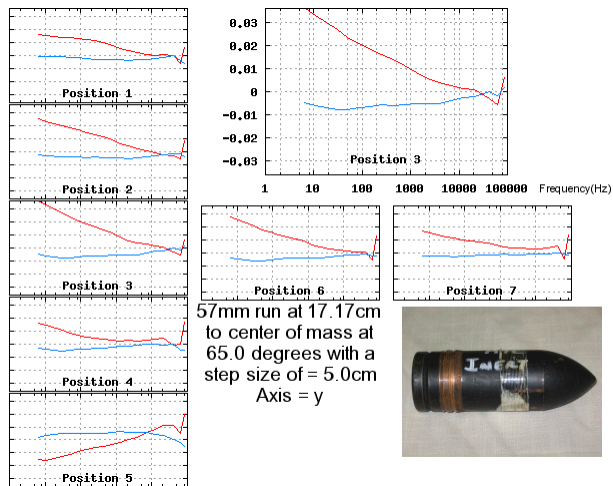
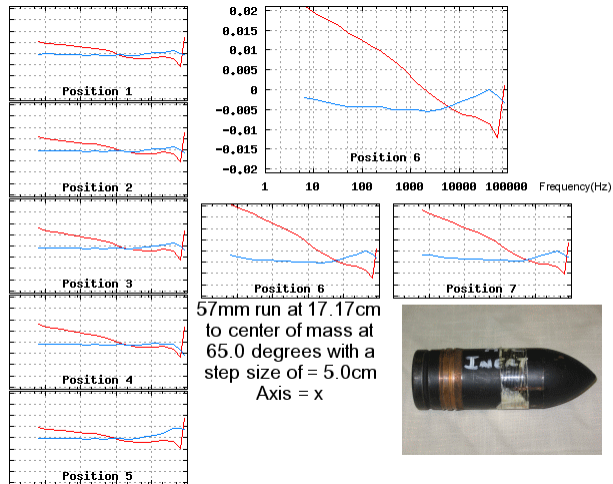
The concept of using multi-axis, broadband target response measurements to achieve reliable, robust discrimination of buried UXO from buried clutter is not yet demonstrated. Magnetoresistive sensor noise has failed to drop as predicted, despite several years of sensor and product development by several commercial manufacturers. However, indications do exist that further work on these sensor systems and classification algorithms may yet enable significant cost reductions in UXO remediation.

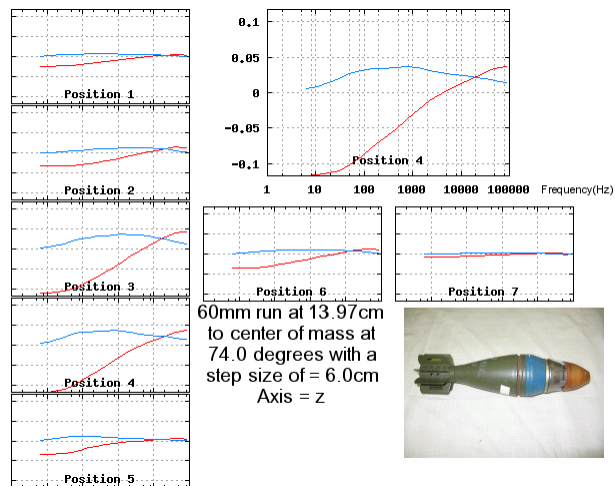
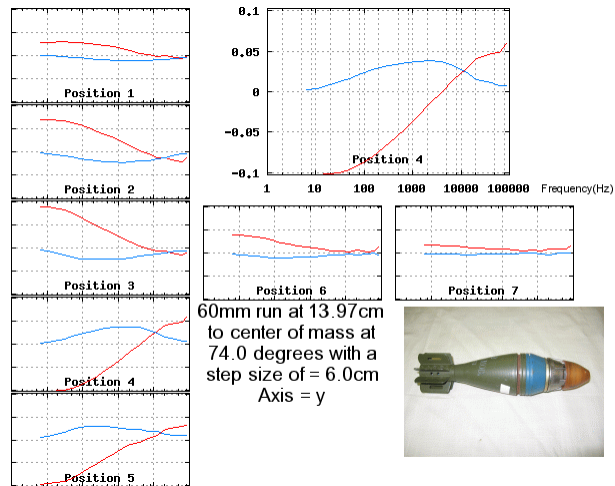
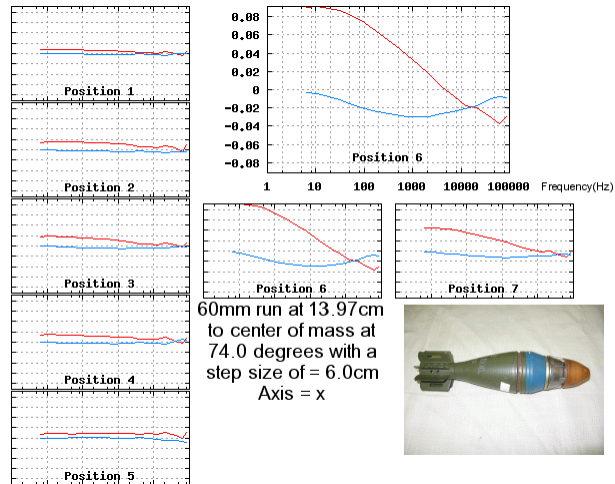
APPENDIX A: FD testing data

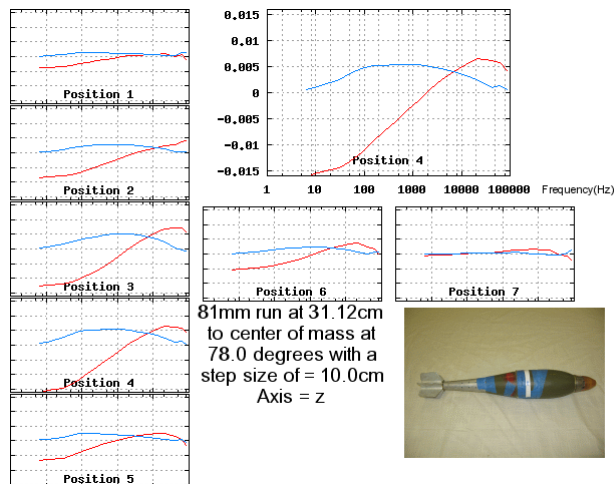
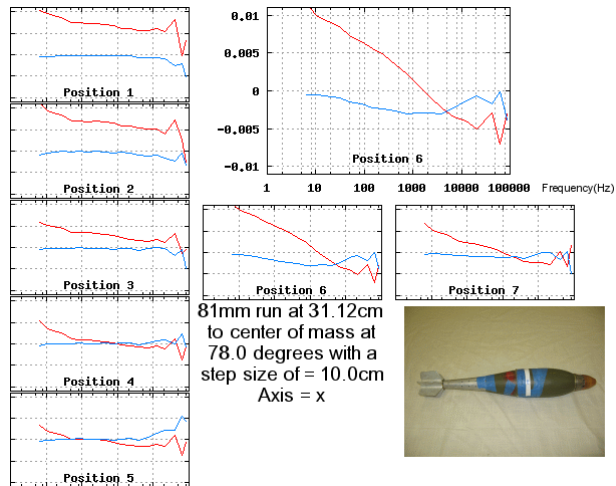
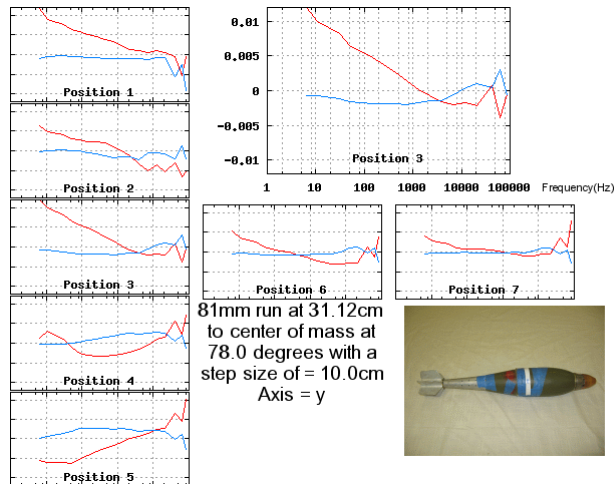
This appendix presents the complete set of raw FD data collected for all UXO and clutter items. Visual inspection of the data may persuade the reader that characteristic differences do exist, that can lead to development of an effective classification algorithm. A separate set of CD ROMs includes the data in numerical form, providing an archive for use in further algorithm development.

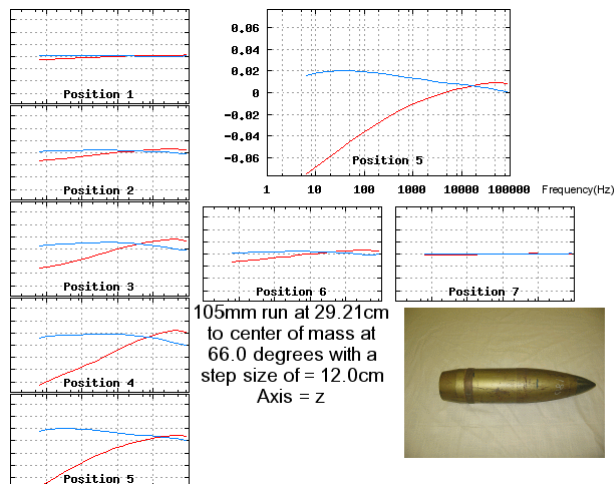
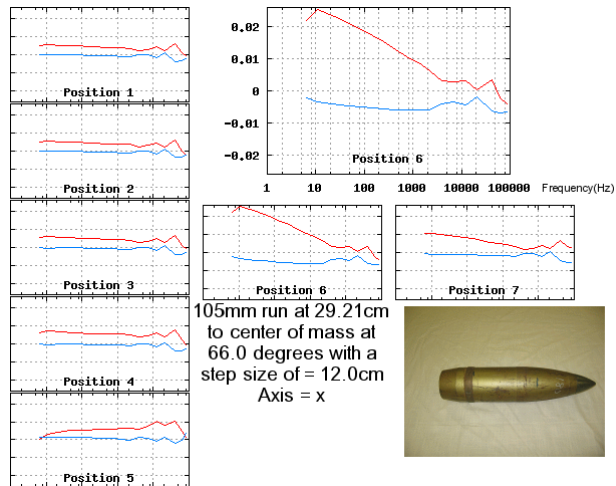
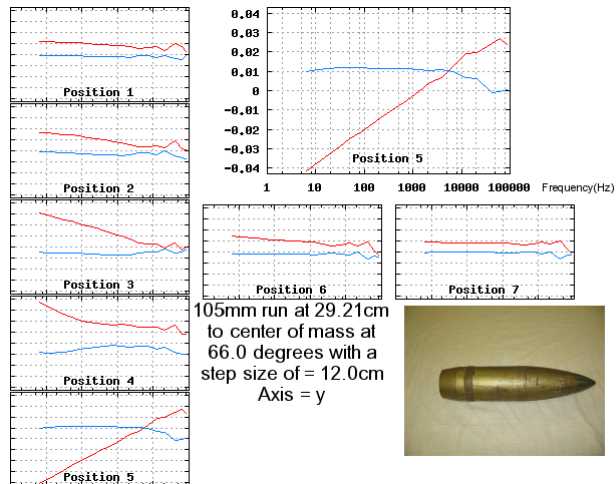


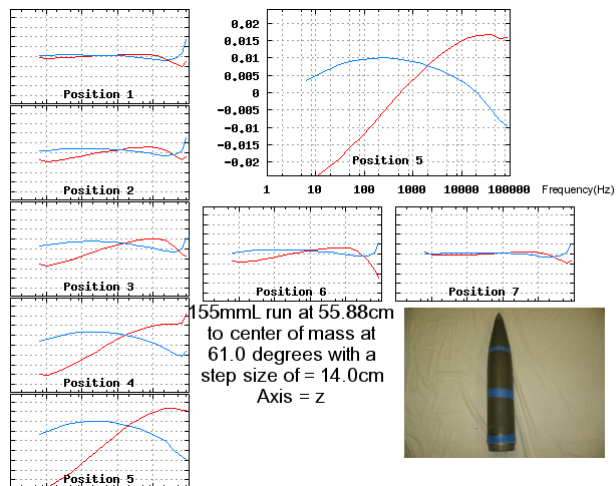
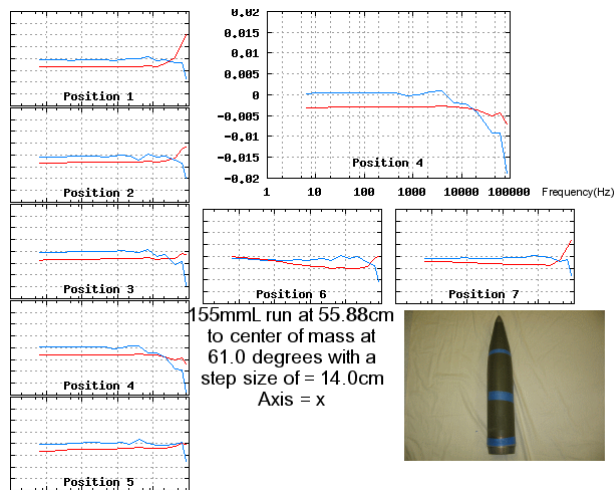
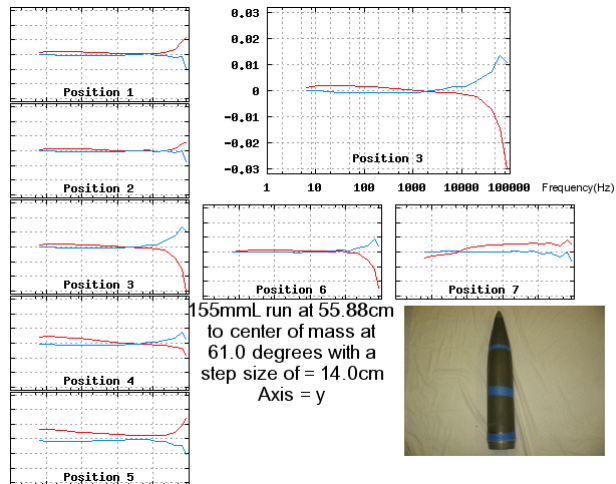


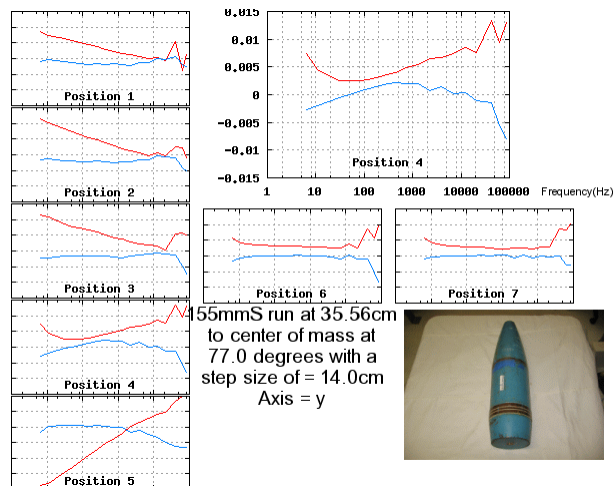
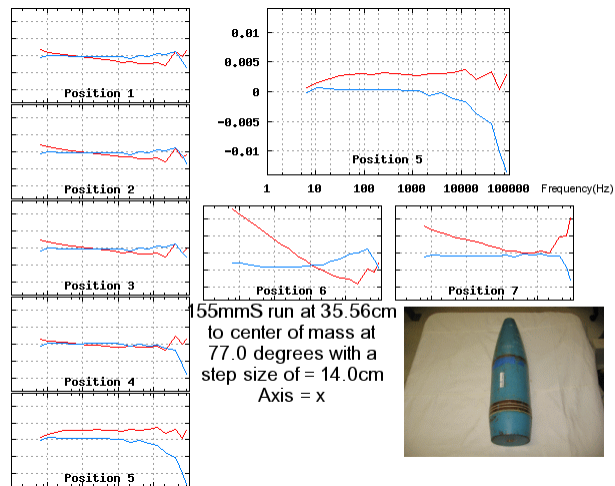
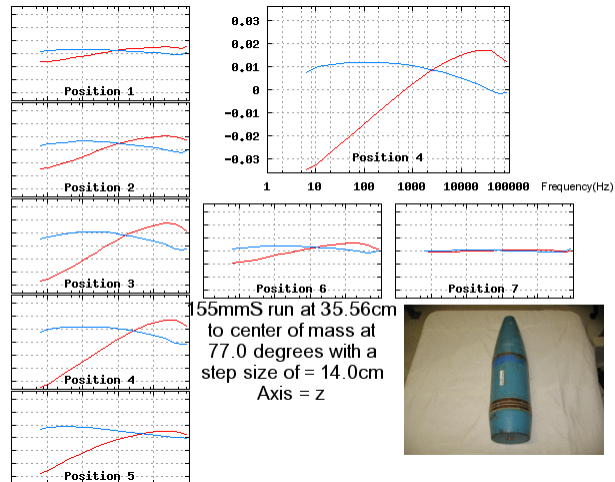


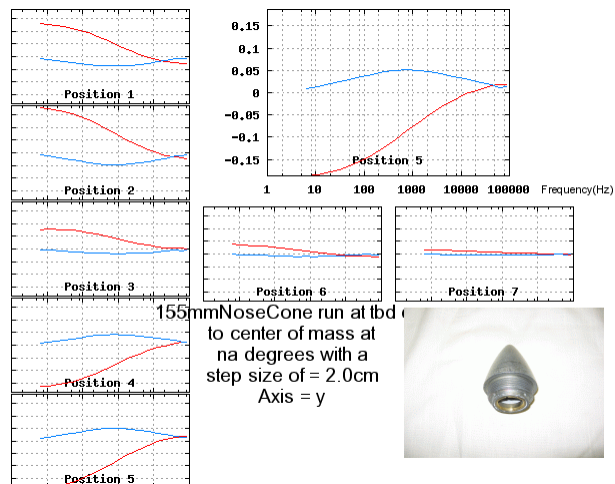
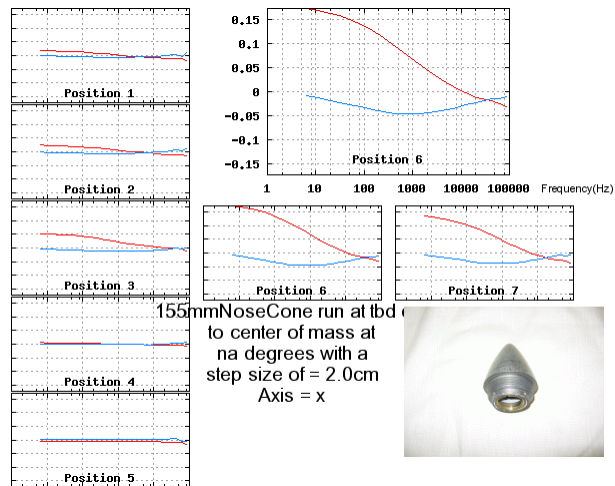
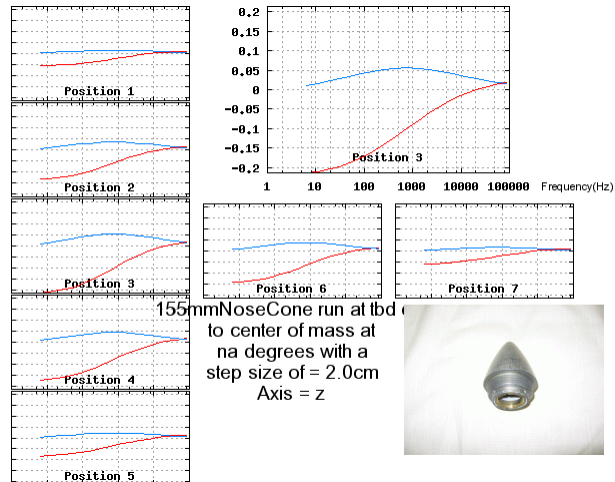


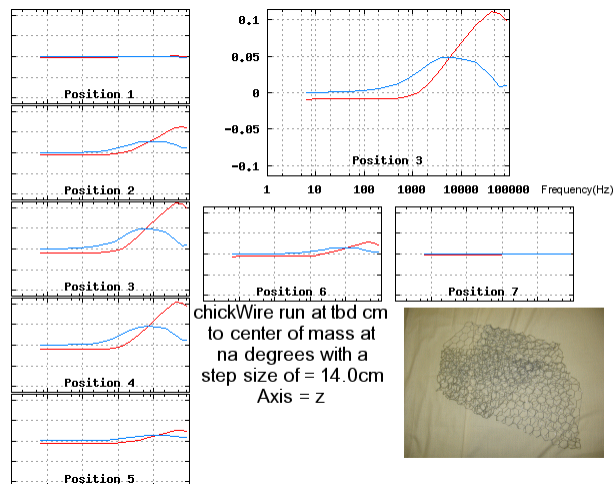
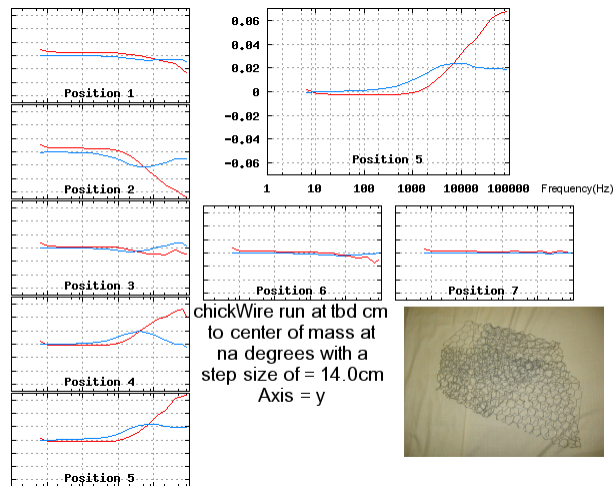
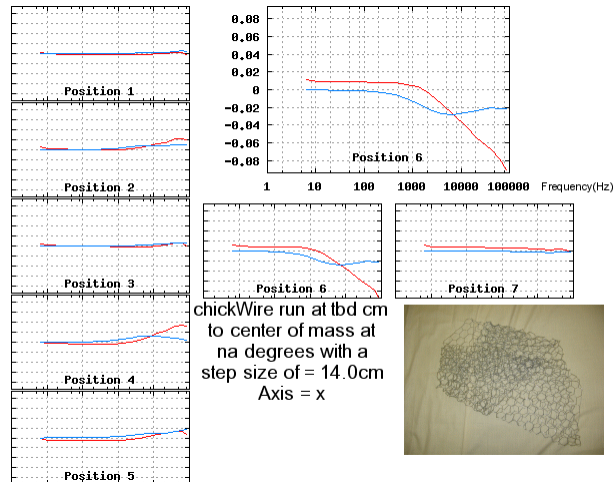


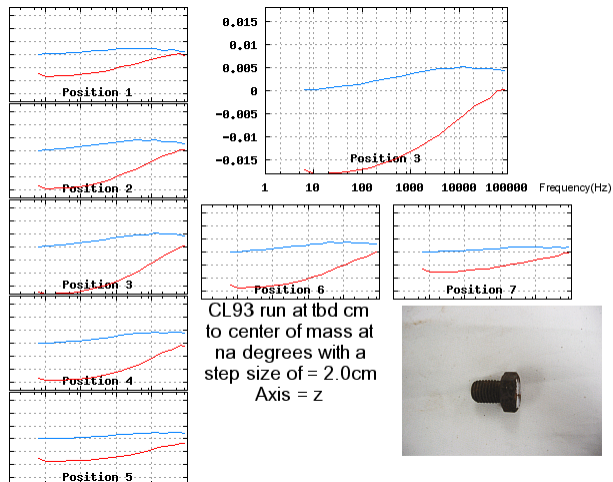
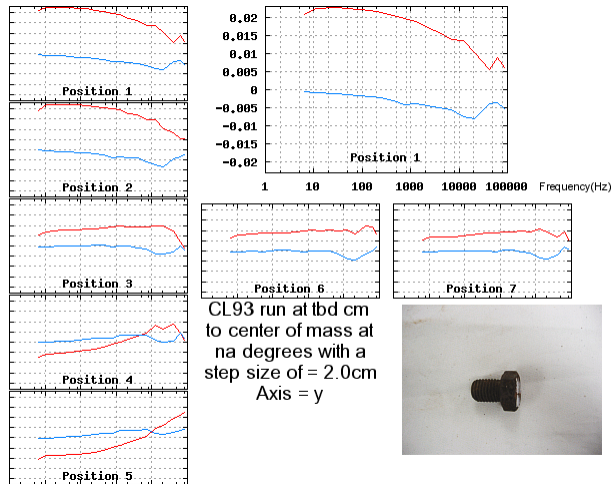
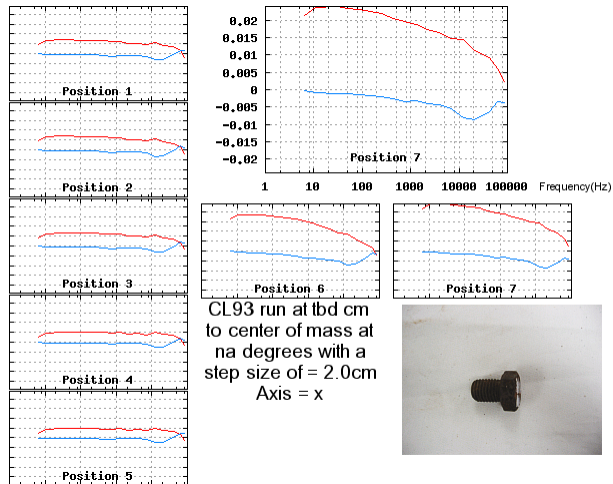


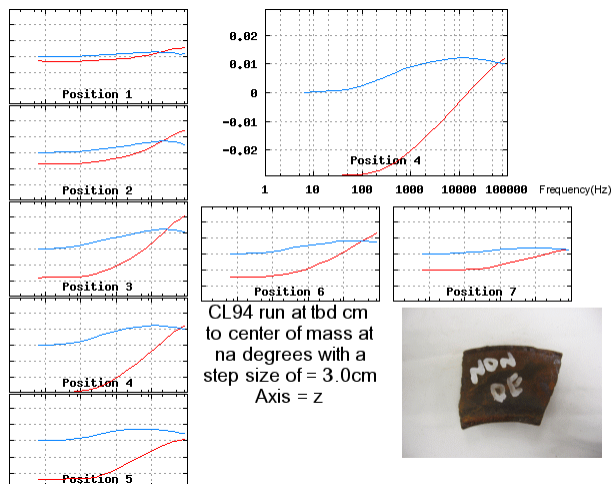
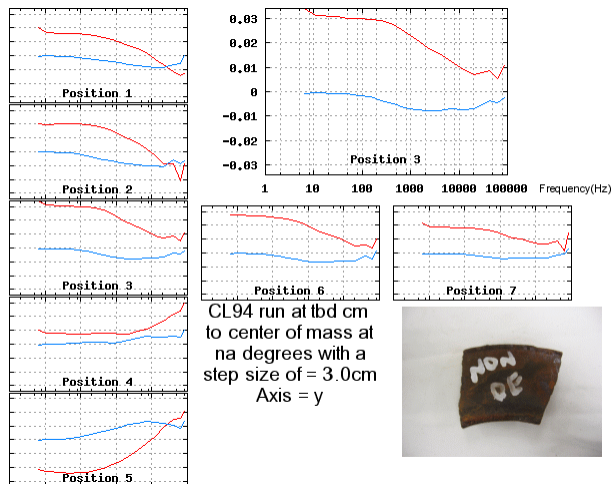
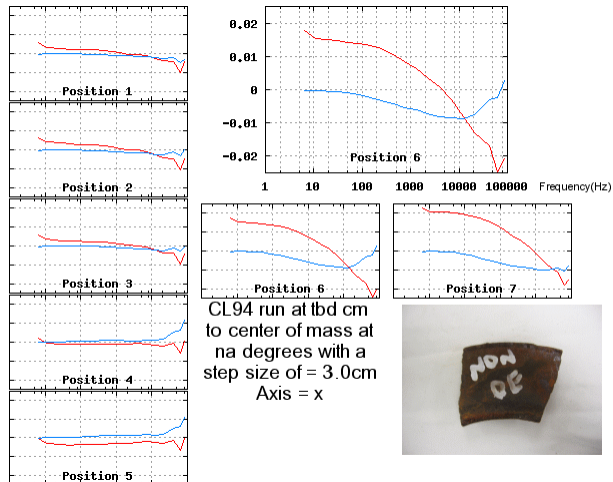


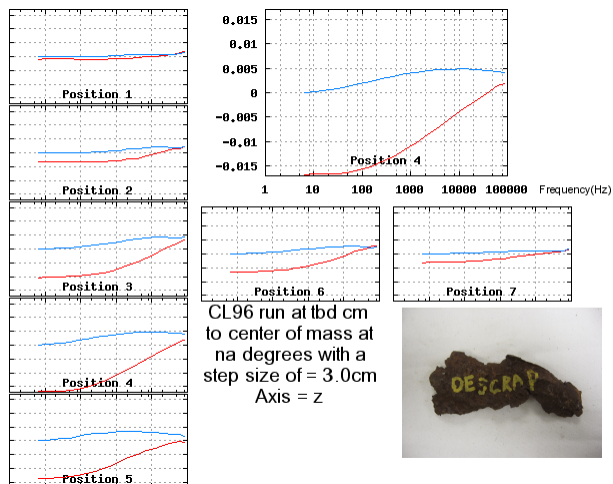
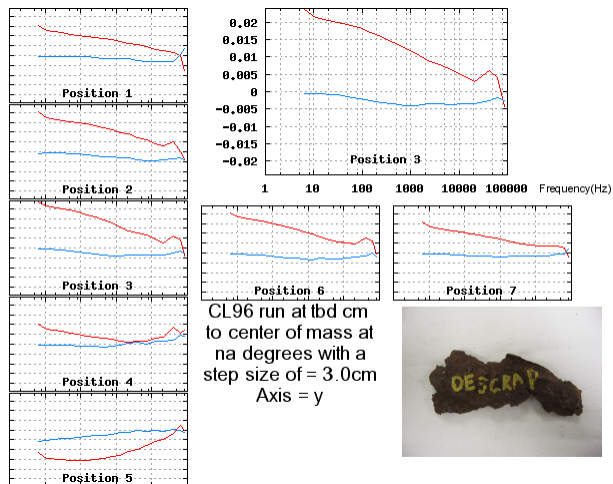
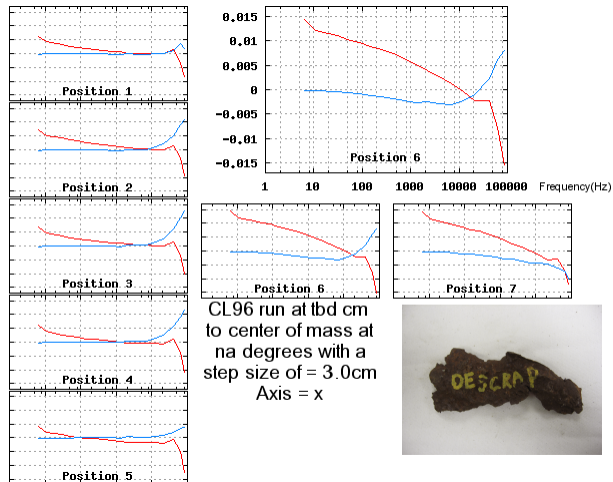


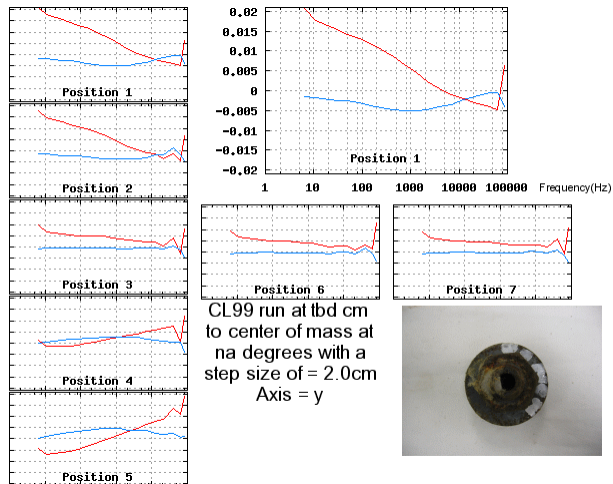
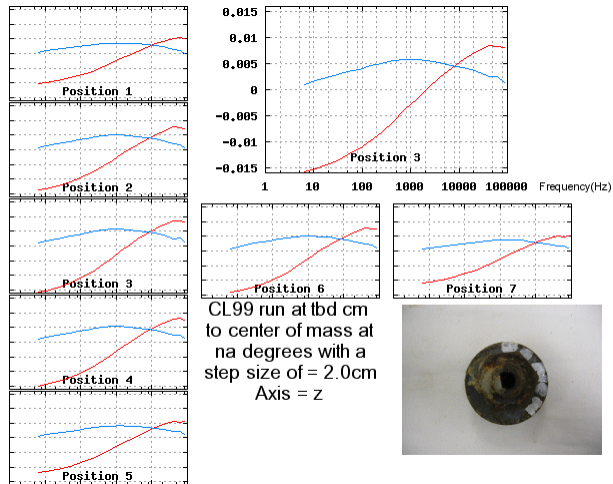
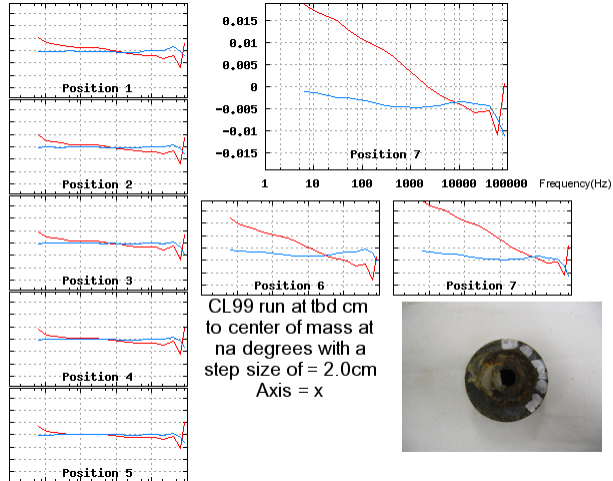


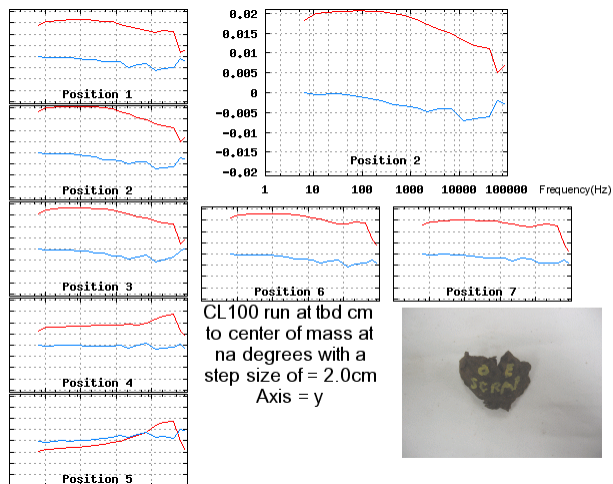
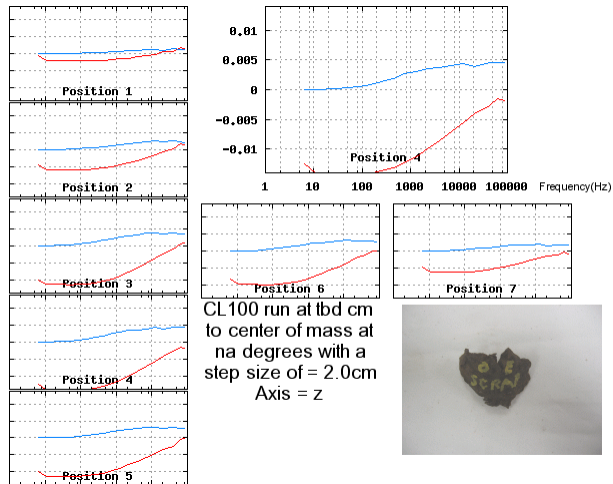
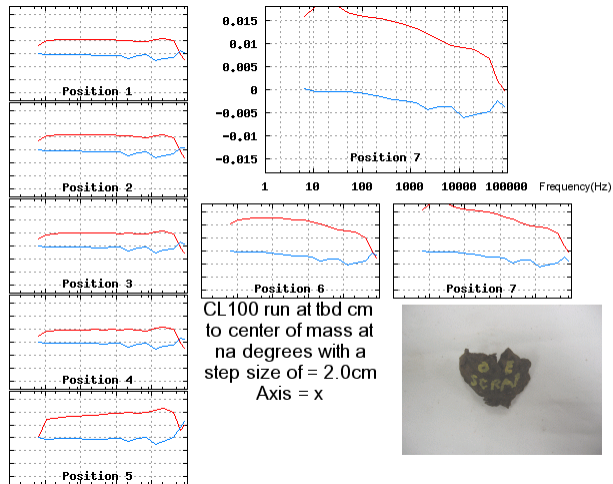


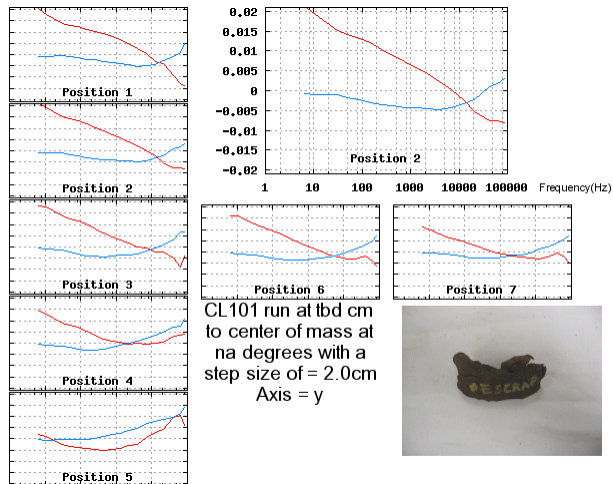
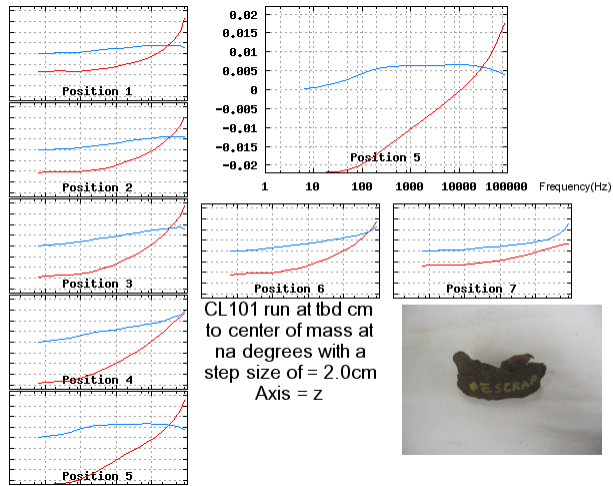
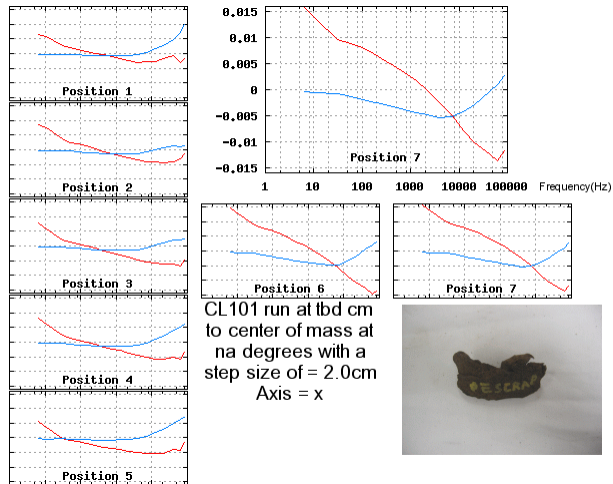


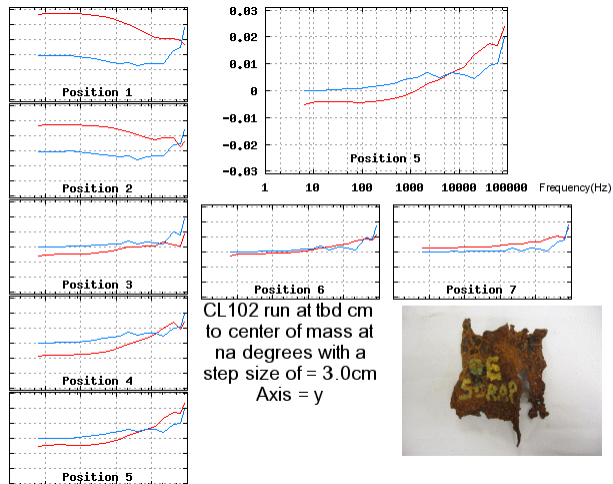
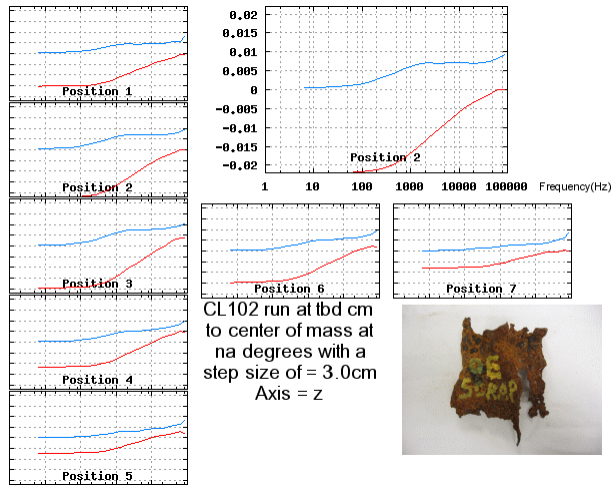
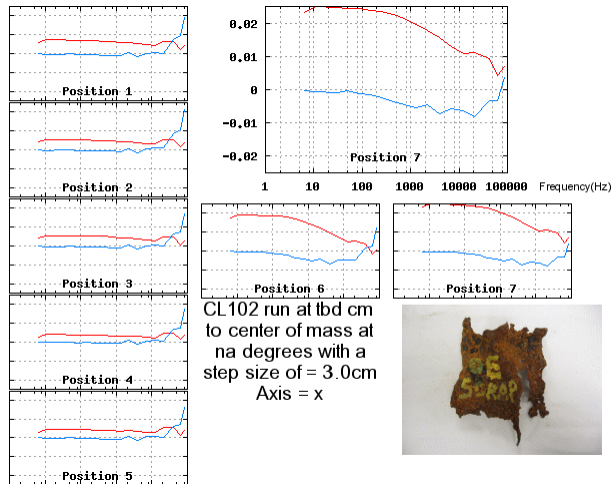


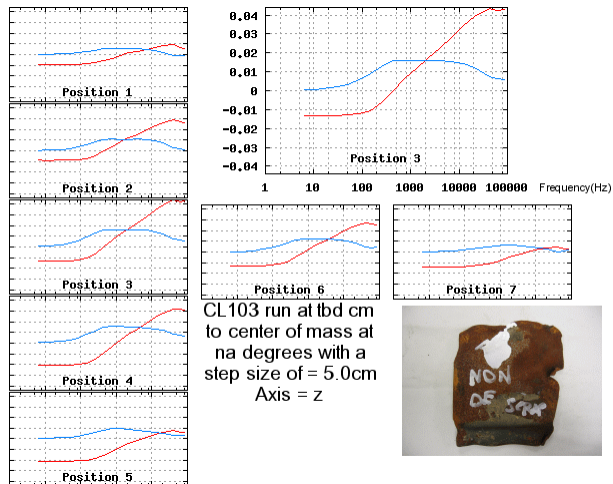
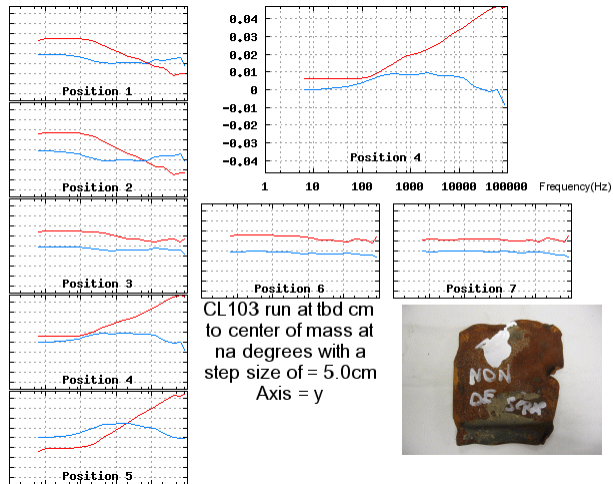
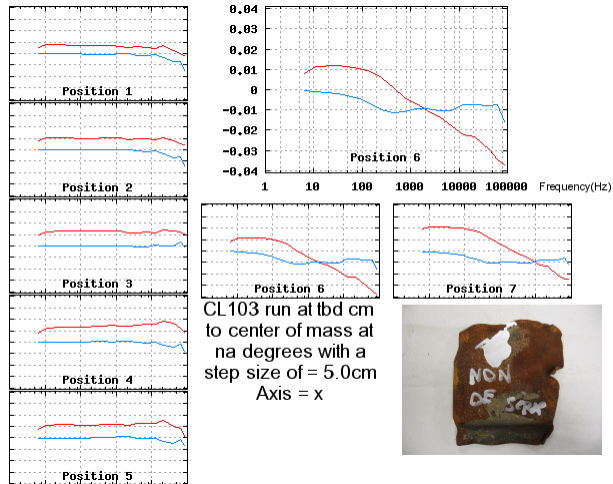


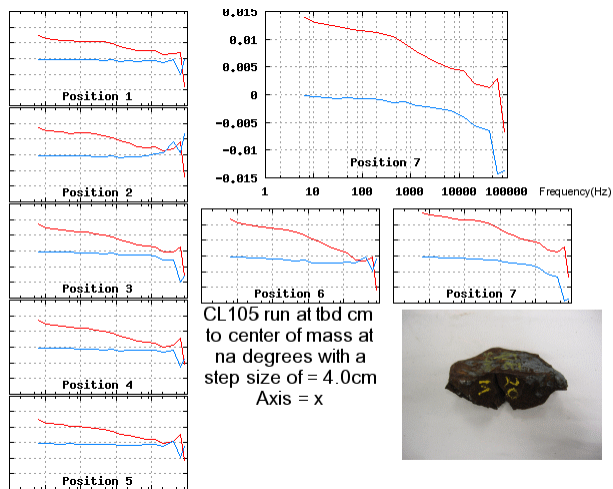
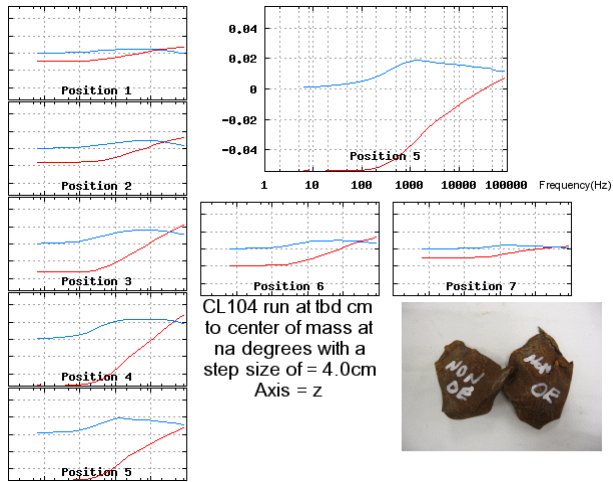
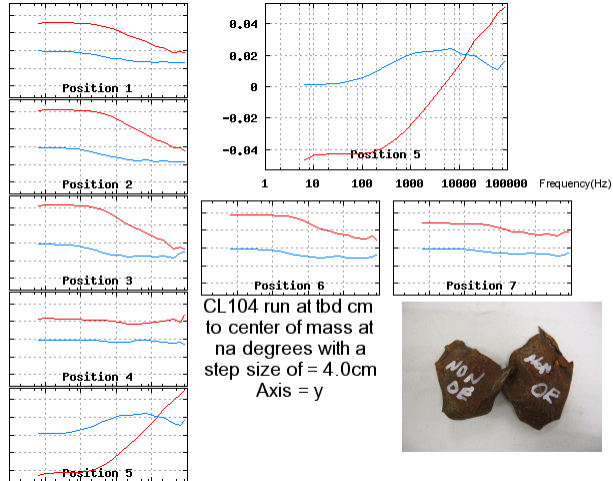


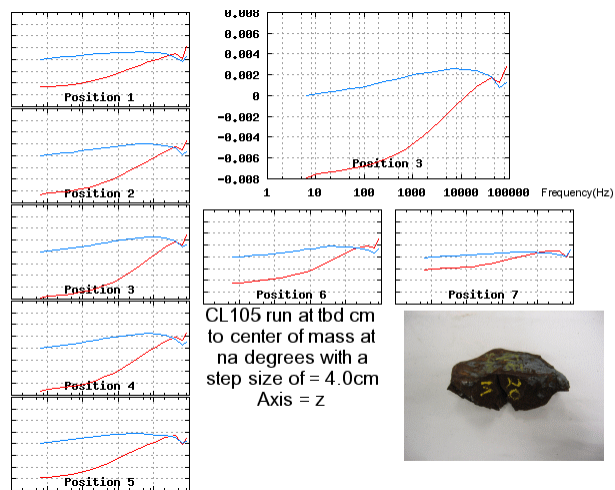
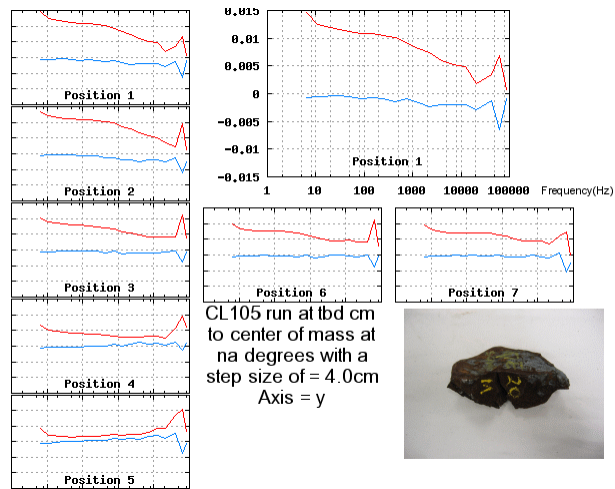
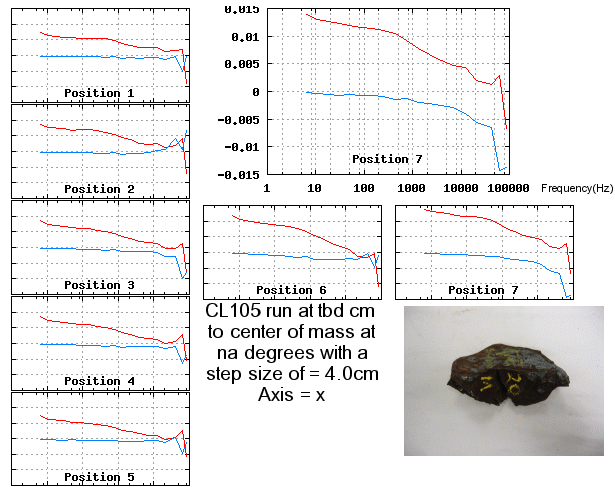


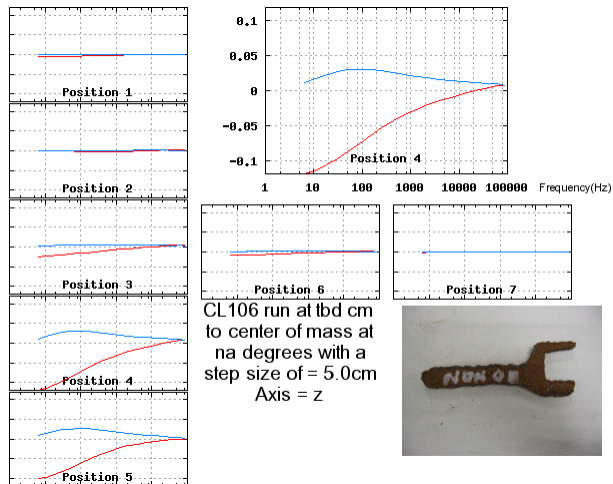
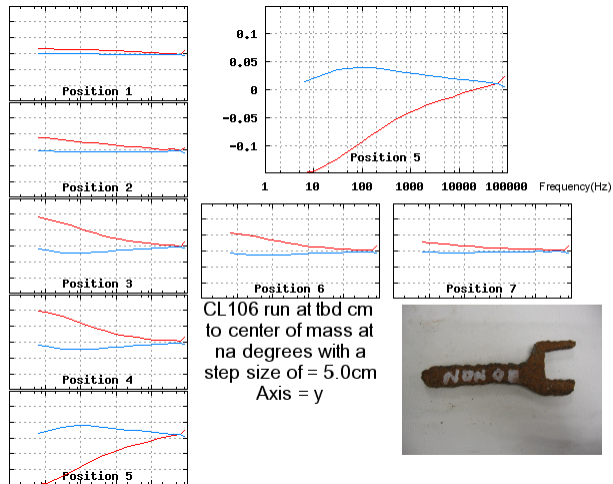
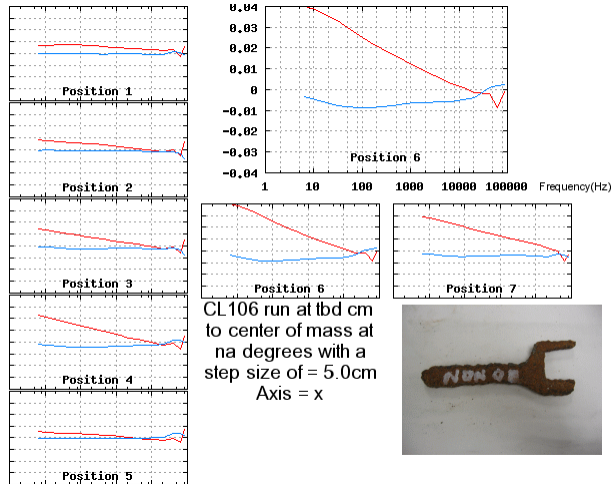


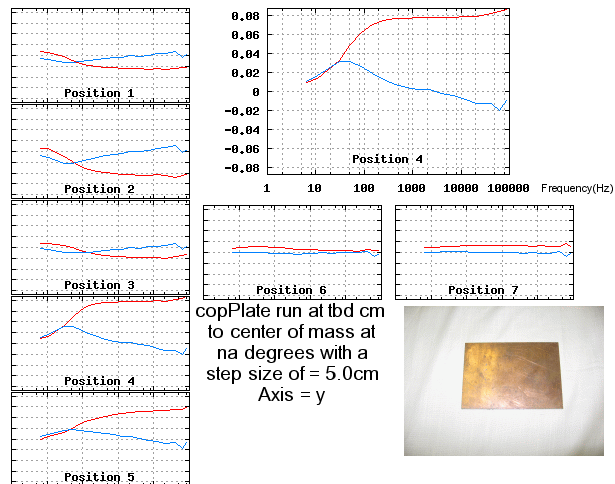
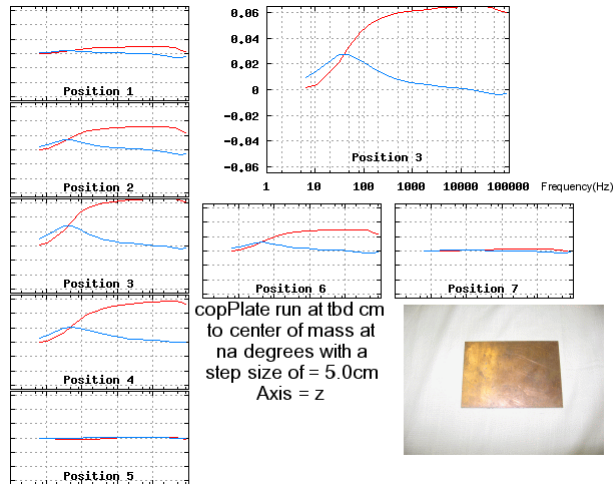
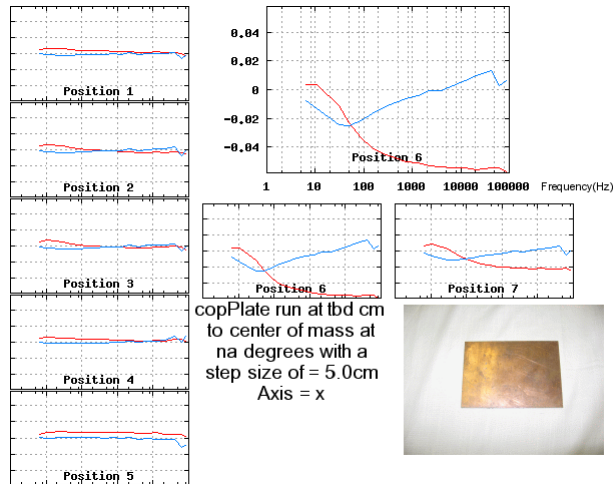


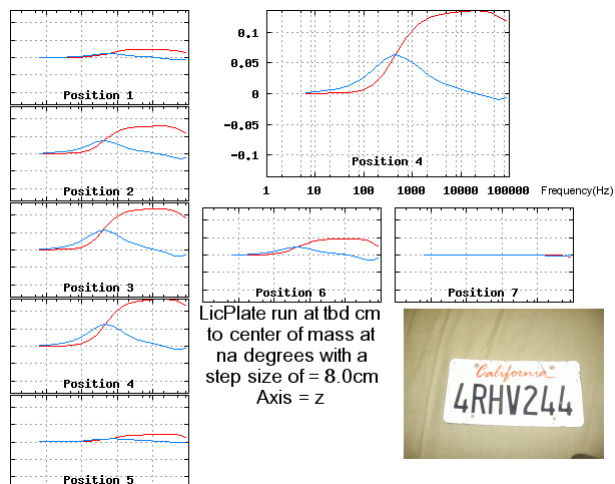
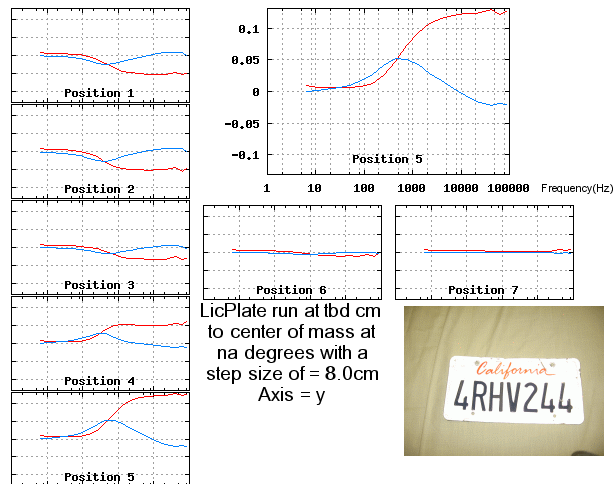
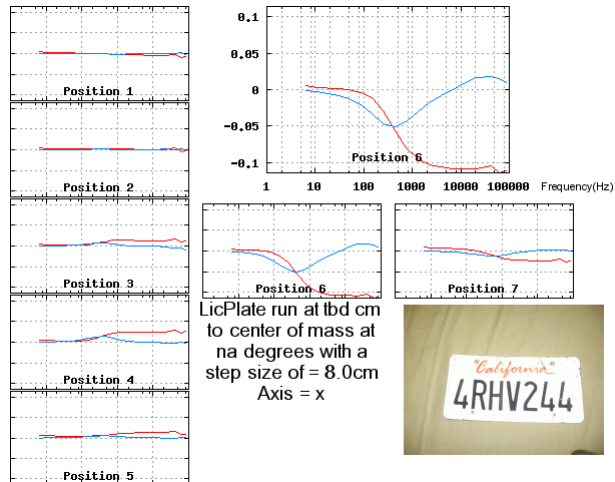


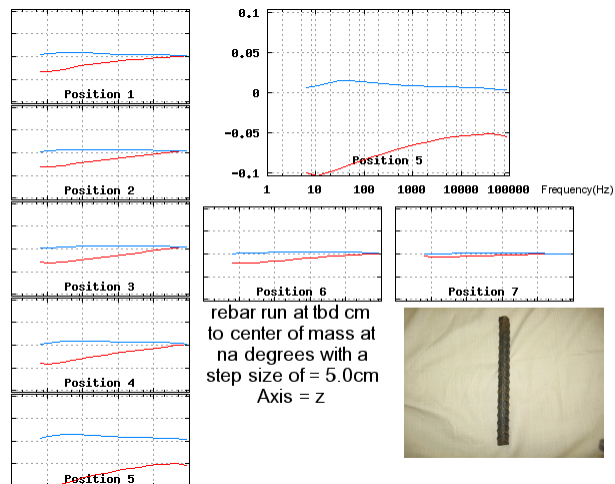
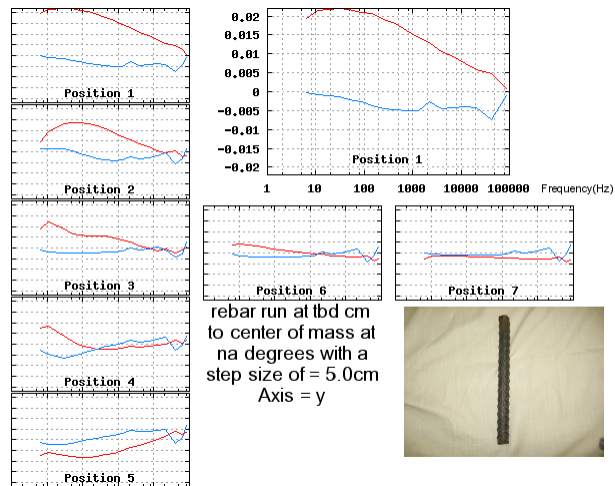
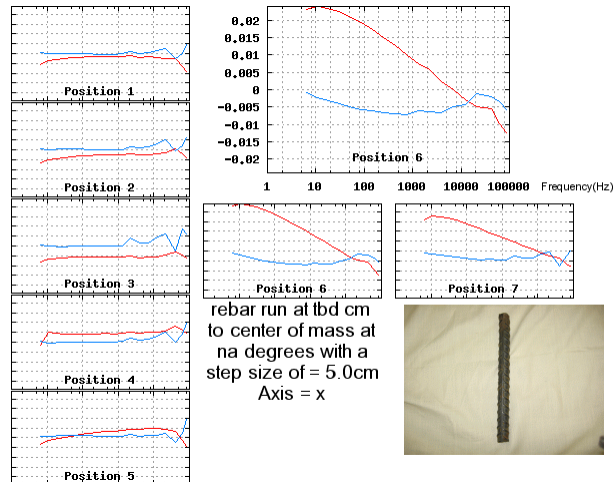


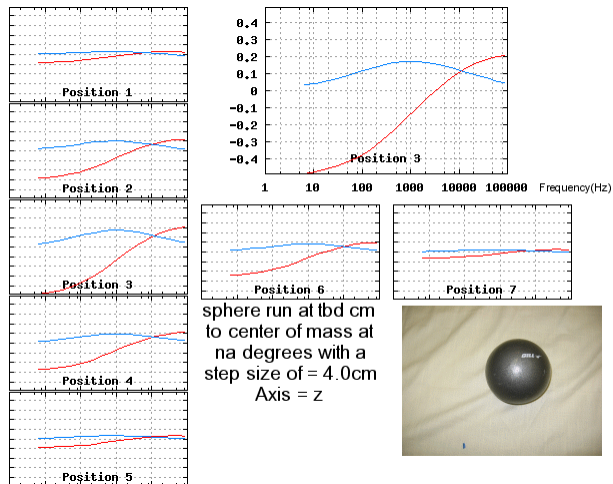
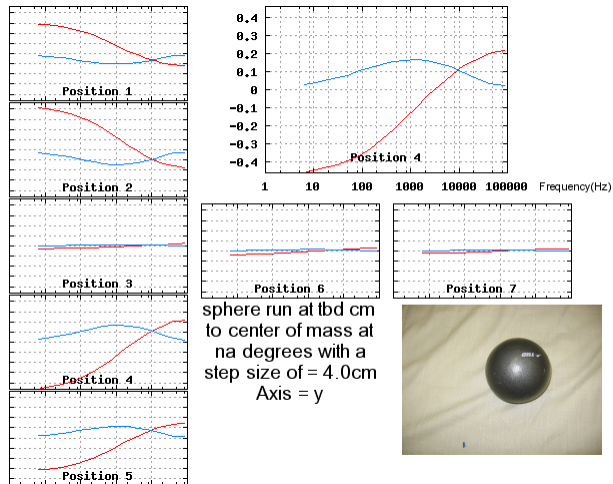
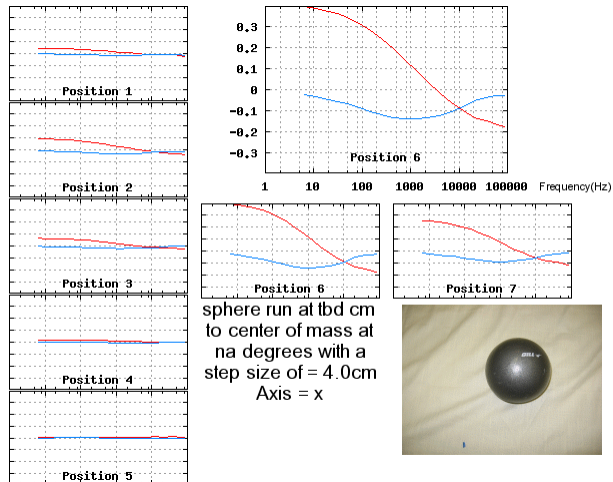






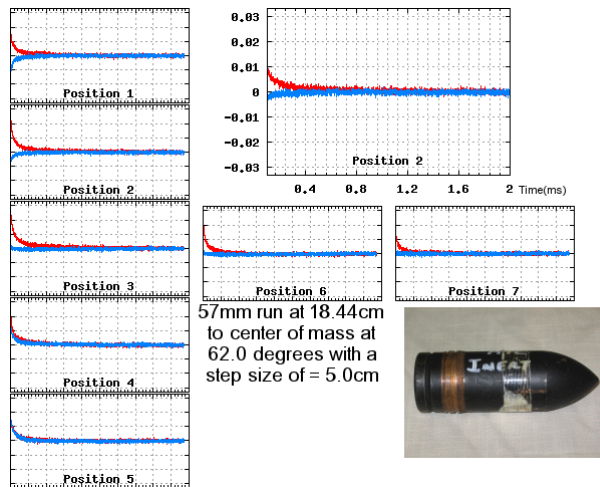
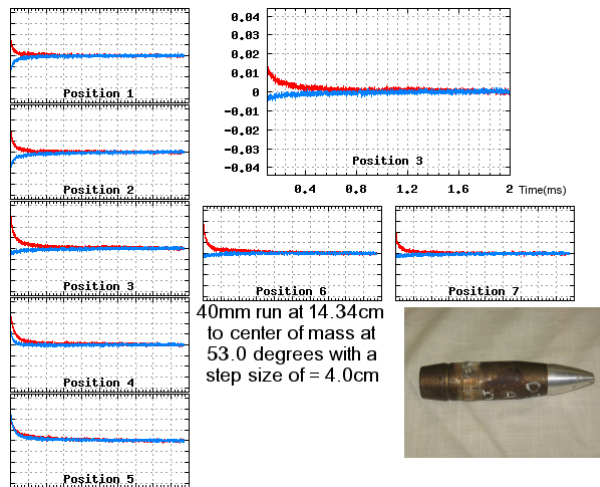
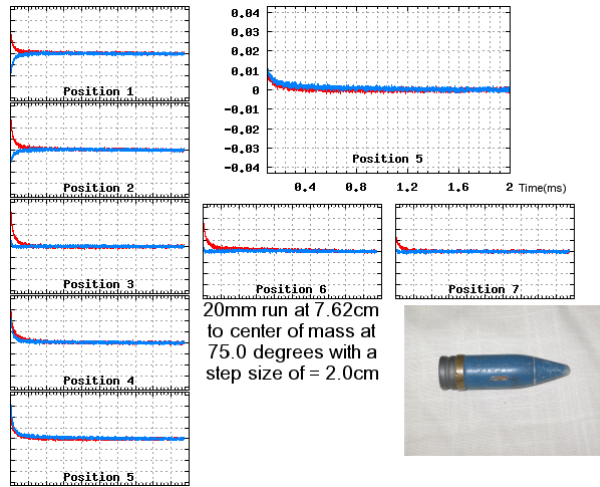


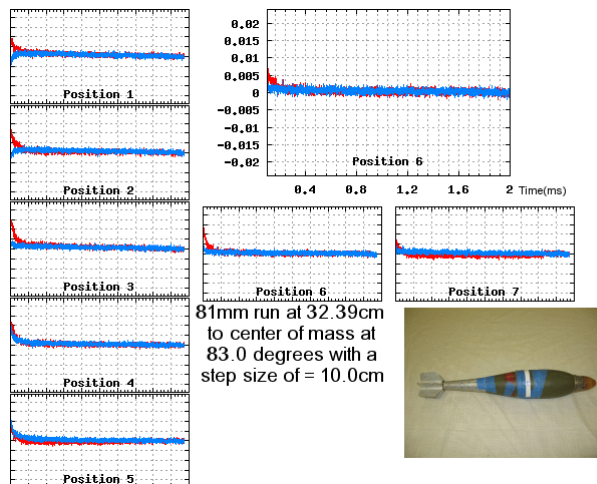
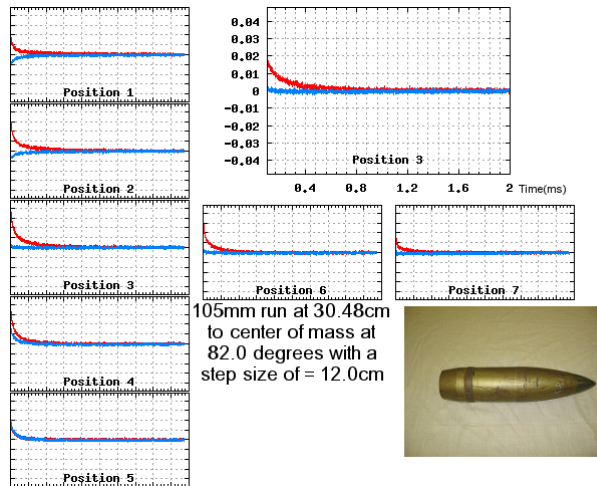
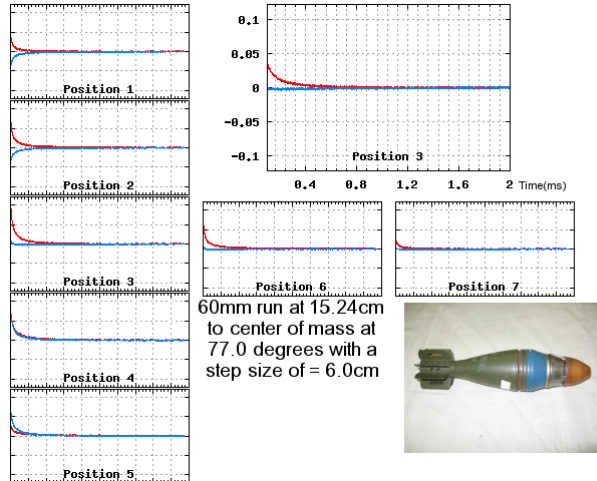


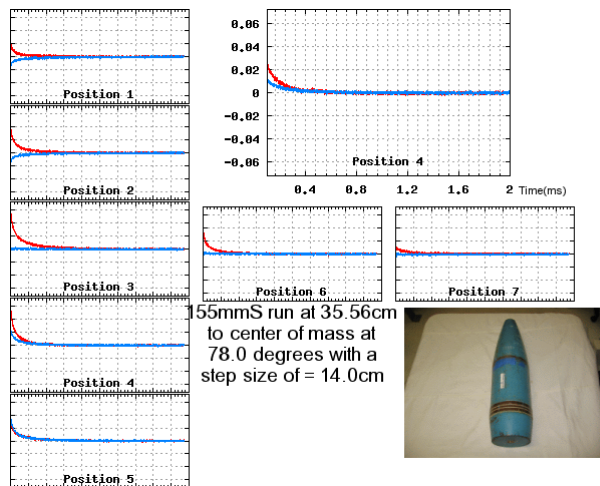
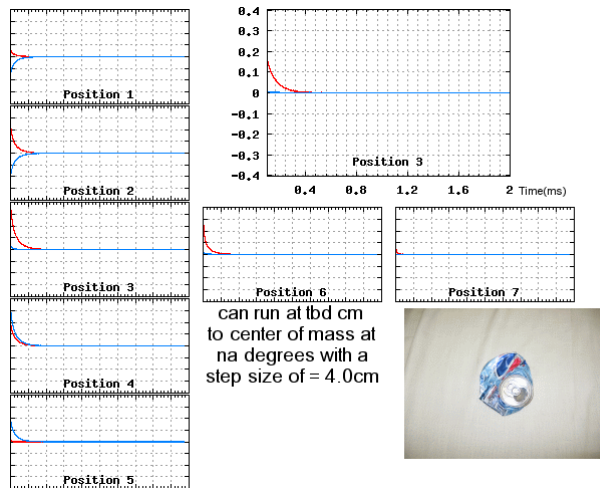
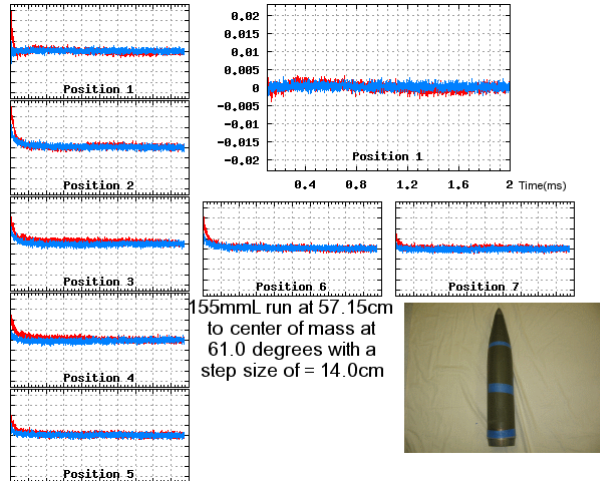


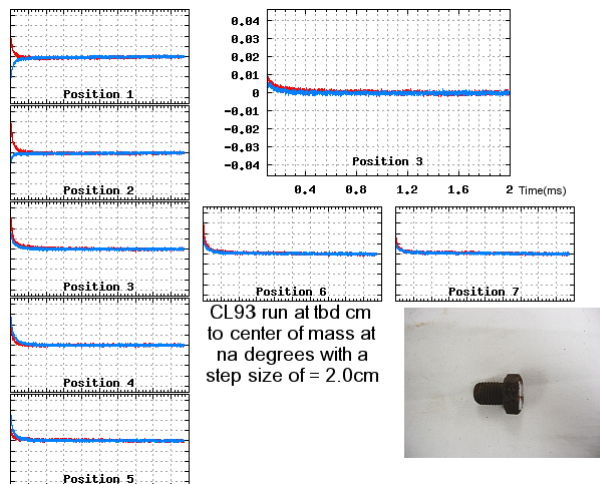
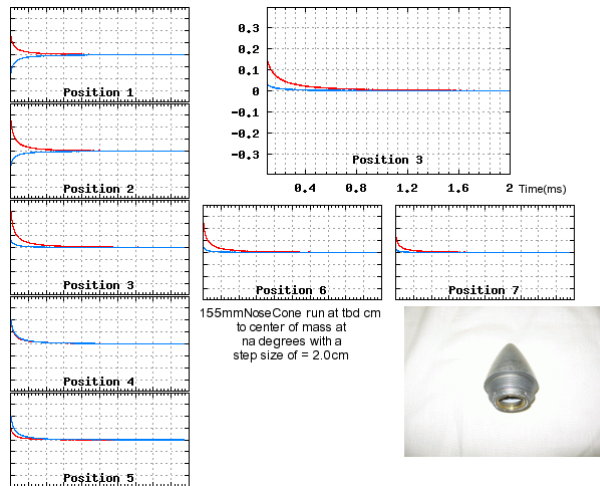
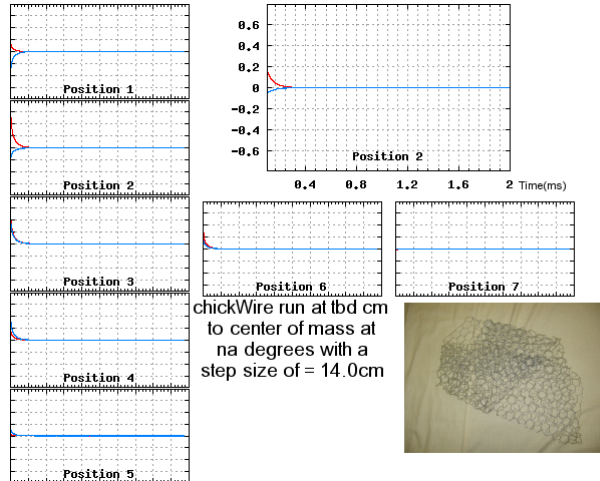
APPENDIX B: TD testing data

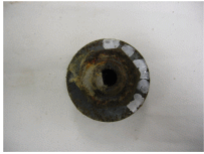
This appendix presents the complete set of raw TD data collected for all UXO and clutter items. Visual inspection of the data may persuade the reader that characteristic differences do exist, that can lead to development of an effective classification algorithm. A separate set of CD ROMs includes the data in numerical form, providing an archive for use in further algorithm development.

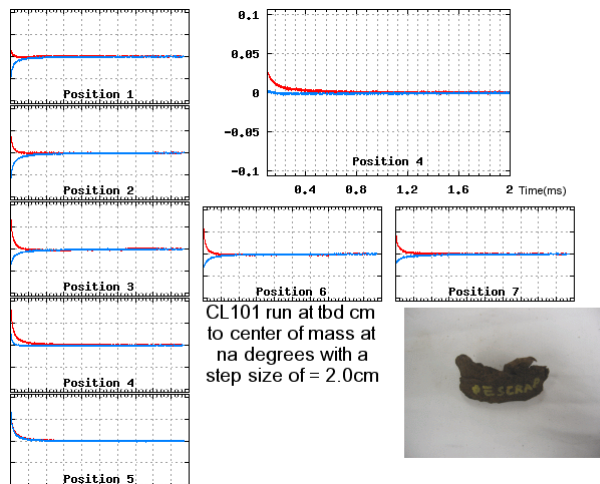
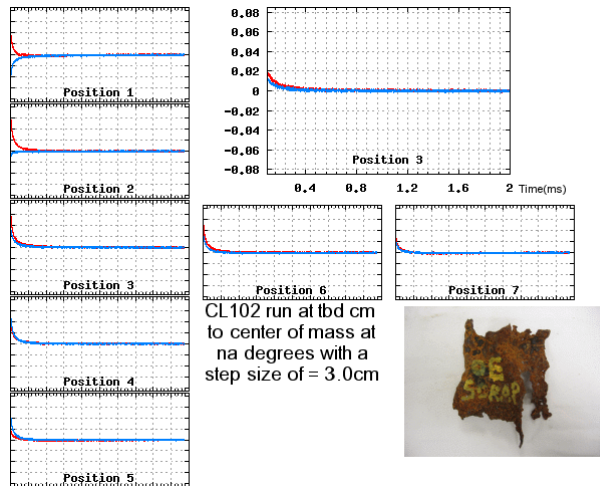
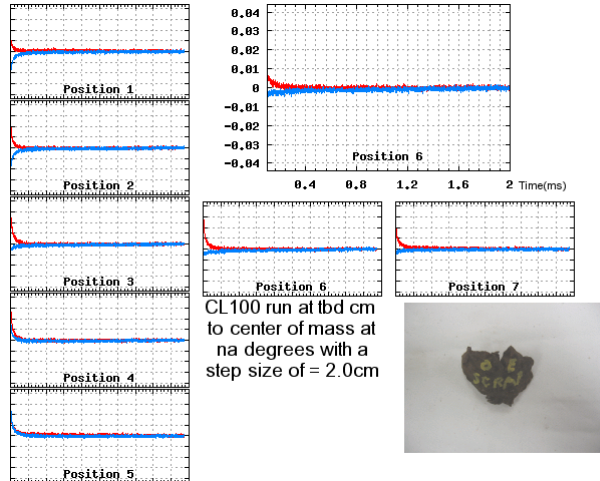


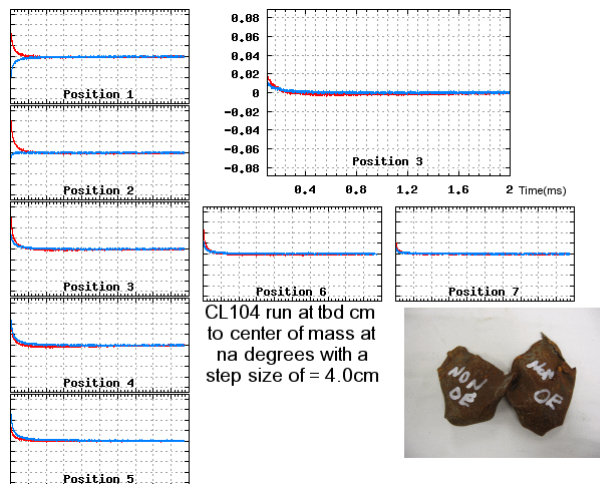
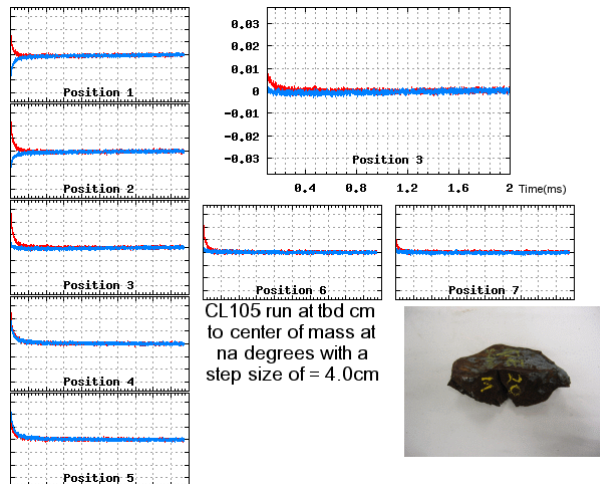
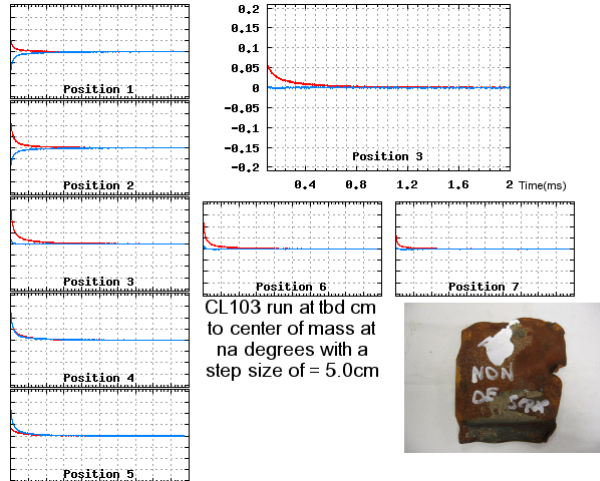


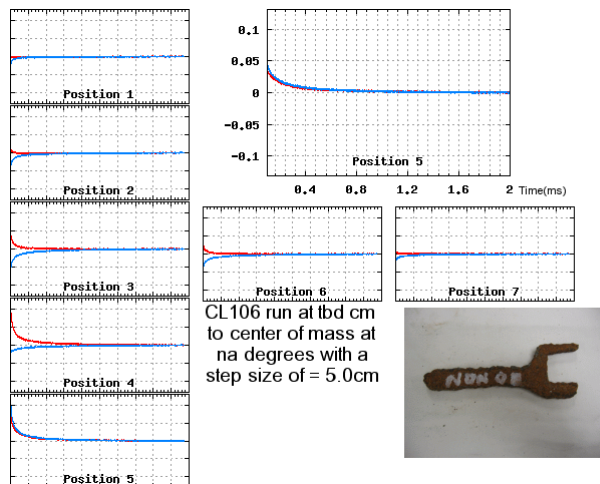
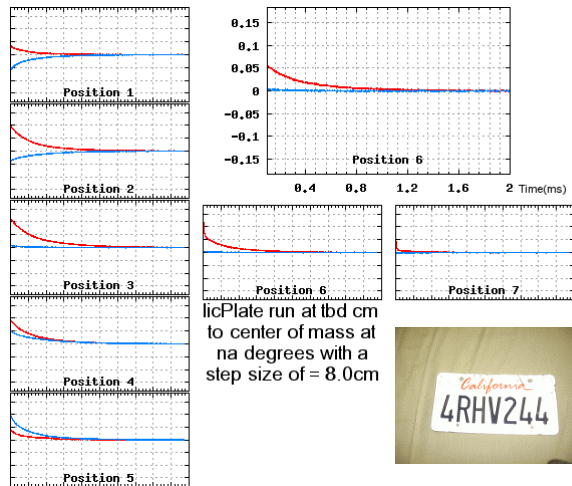
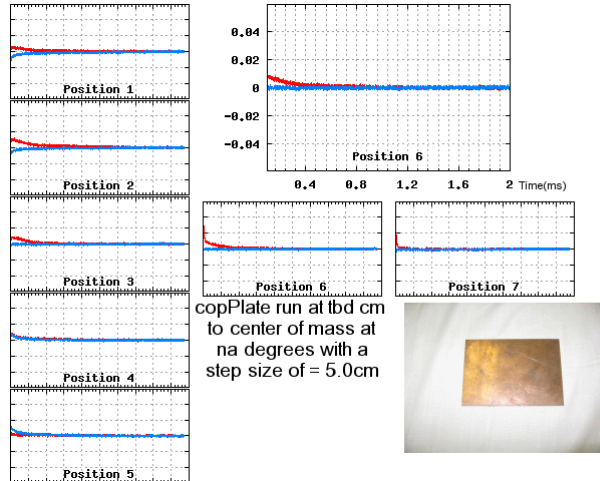


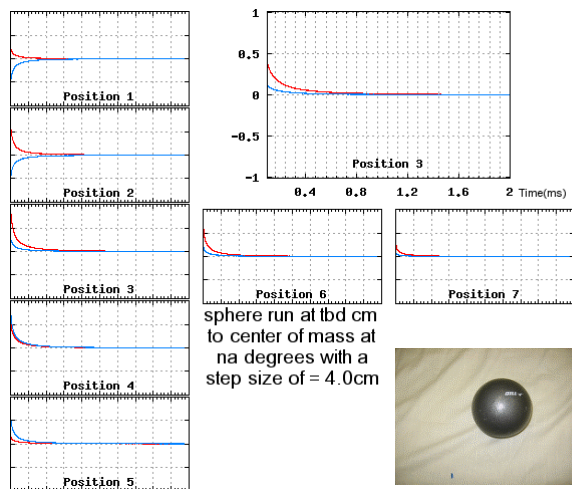
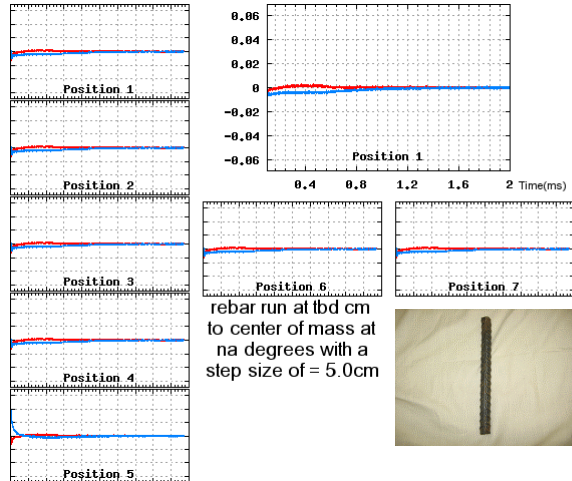












APPENDIX C: List of Technical Publications

L. Carin, H. Yu, Y. Dalichaouch, A.R. Perry, P.V. Czipott and C. Baum, On the wideband EMI response of a rotationally symmetric permeable and conducting target, *IEEE Transactions on Geoscience and Remote Sensing* **39**, 1206-1213, 2001.